THE UNIVERSITY OF CHICAGO

MECHANISMS OF PROTEIN TARGETING TO BIOMEMBRANES

A DISSERTATION SUBMITTED TO

THE FACULTY OF THE DIVISION OF THE PHYSICAL SCIENCES

IN CANDIDACY FOR THE DEGREE OF

DOCTOR OF PHILOSOPHY

DEPARTMENT OF CHEMISTRY

BY

MORRIS ELI SHARP

CHICAGO, ILLINOIS

DECEMBER 2018

For Bethany, who somehow gets me through every day

Table of Contents

List of Figures viii

List of Tables xi

Acknowledgements xii

Abstract xv

Chapter 1. Introduction 1

1.1 Lipids and Lipid Membranes 1

1.2 Emulsions and Lipid Droplets 3

1.3 Protein Targeting to Membranes 4

1.4 Enhanced Sampling and Free Energy Sampling Techniques 7

1.5 Thesis Aims and Chapters 10

Chapter 2. Mechanism and Determinants of Amphipathic Helix-Containing Protein Targeting to Lipid Droplets 12

2.1 Summary 12

2.2 Introduction 12

2.3 Results 15

2.3.1 Molecular Dynamics Simulations Reveal that LD Surfaces Exhibit Numerous, Large Phospholipid Packing Defects 15

2.3.2 Initial Binding of the CCTα Amphipathic Helix to the LD Surface in Molecular Dynamics Simulations 18

2.3.3 Insertion of Large Hydrophobic Residues into Packing Defects Mediates LD Protein Binding 20

2.3.4 Amphipathic Helix Binding to Phospholipid Surfaces *In Vitro* Depends on Large Hydrophobic Residues Recognizing Membrane Packing Defects 22

2.3.5 Large Hydrophobic Residues Are Critical for Amphipathic Helix Binding to LDs in Cells 28

2.3.6 Promiscuous binding of amphipathic helices containing large hydrophobic residues to cellular lipid droplets 32
2.4 Discussion 34
2.5 Acknowledgements 39
2.6 Method Details 40
2.6.1 Cell Lines and Cell Culture 40
2.6.2 Molecular Dynamics Simulations 40
2.6.3 Peptides Design 43
2.6.4 Plasmids Construction and Transfection 44
2.6.5 LDs induction 44
2.6.6 Microscopy 44
2.6.7 In Vitro Assays 45
2.6.8 Quantification and Statistical Analysis 46
2.7 Supplementary Information 48
Chapter 3. Distribution of Amino Acids in Bilayer and Lipid Droplet-Like Membranes ... 54
3.1 Introduction 54
3.2 Results 56
3.2.1 Lipid Packing Defect Distributions in Lipid Droplets with Various Compositions 56
3.2.2 Distribution of Small Hydrophobic Residues: Ala, Val, Leu, Ile 59
3.2.3 Distribution of Aromatic Residues: Phe, Trp 61
3.2.4 Distribution of Polar Residues: Thr 62
3.3 Discussion 63
3.4 Conclusion 66
3.5 Methods 66
3.5.1 General Simulation Parameters 66
3.5.2 Single Residue Simulation Setup 67
3.5.3 Single Residue Metadynamics 67

3.5.4 Lipid packing defects 68
3.6 Acknowledgements 69
Chapter 4. Targeting of hydrophobic hairpin motifs to the surface of lipid droplets from the ER 70
4.1 Introduction 70
4.2 Results and Discussion 72
4.2.1 GPAT4 Hairpin Contains Sequence Specific Residues Required and Sufficient for Targeting to Lipid Droplets 72
4.2.2 Molecular Dynamics Simulations Reveal GPAT4 Structural Differences in Bilayer and LD Membranes 81
4.2.3 Lipid Droplet Preference of GPAT4 is Driven by a Shift Upwards in the Membrane Driven by the Hydrophobic Residues. 89
4.3 Conclusion 94
4.4 Methods 95
4.5 Acknowledgements 100
Chapter 5. Endophilin H0 Folding on Bilayer Membranes 101
5.1 Introduction 101
5.2 Results and Discussion 102
5.3 Methods 107
5.4 Acknowledgements 108
Chapter 6. A Bottom Up Approach for Multi-Configuration Coarse Grained Molecular Dynamics 109
6.1 Abstract 109
6.2 Introduction 109
6.3 Theory and Methods 112
6.3.1 Theory 112

6.3.2 Simulation Details 115
6.4 Results and Discussion 118
6.4.1 Dodecaalanine 118
6.4.2 Endophilin H0 126
6.5 Conclusion 129
Bibliography 131

List of Figures

Figure 1-1 Structure of Glycerolipids 1

Figure 1-2 Structure of Fatty Acids, Phospholipids, and Triacylglycerols 2

Figure 1-3 Helical Wheel Plot of Endophilin H0 5

Figure 1-4 Schematic of Amphipathic Helices Targeting to Lipid Droplets 6

Figure 1-5 Schematic of Metadynamics Free Energy Sampling 10

Figure 2-1 Molecular Dynamics Simulations Reveal that LDs Have Larger and More Persistent Surface Packing Defects than Bilayer Membranes 17

Figure 2-2 Molecular Dynamics Simulations Show that Amphipathic Helices Insert Bulky Hydrophobic Residues into Large Lipid Packing Defects 19

Figure 2-3 Amphipathic Helix Sequences with Large Hydrophobic Residues Bind LDs and Packing Defect-Rich Membranes in *In Vitro* Systems 23

Figure 2-4 Large Hydrophobic Residues Are Crucial for LD Targeting of the M-domain in Cells 27

Figure 2-5 Binding of Amphipathic Helices to Cellular Lipid Droplets Correlates with the Number of Large Hydrophobic Residues 33

Figure 2-6 Proposed Thermodynamic Cycle for the Partitioning of Amphipathic Helices at the LD Surface 35

Figure 2-7 Histogram of packing defect sizes for bilayer and monolayer surfaces with varying TG thicknesses. 48

Figure 2-8 Representative Z-distances between the carbon-alpha of a specific residue and the membrane phosphate plane. 49

Figure 2-9 Amphipathic Helix binding to GUVs 50

Figure 2-10 Analysis of the LD-targeting ability of a range of AH domains from LD- (Core), lipoprotein- (ApoC-I) and bilayer membrane-targeting proteins. 51
Figure 3-1 Defect Distributions for monolayer membranes with different compositions..... 57
Figure 3-2 Snapshot and Z-density profile of bilayer and monolayer membranes 59
Figure 3-3 PMFs for Small Hydrophobic Residues in Bilayer and Monolayer..... 60
Figure 3-4 PMFs for Large Hydrophobic Residues in Bilayer and Monolayer..... 61
Figure 3-5 PMFs for Polar Residues in Bilayer and Monolayer 62
Figure 3-6 Thermodynamic Cycle for Calculating Free Energy Difference Between Bilayer and Monolayer for Phe 63
Figure 3-7 Comparisons of Extrema in Bilayer and Monolayer Membranes for Amino Acids... 65
Figure 4-1 GPAT4 Hairpin is Sufficient for LD Targeting 73
Figure 4-2 GPAT4 Hairpin Contains Sequence Specific Residues Required for LD Targeting.. 74
Figure 4-3 Charged Residues on GPAT4 Play a Role in LD Targeting..... 75
Figure 4-4 R179 is Key to LD Targeting by GPAT4 Hairpin 77
Figure 4-5 Large Hydrophobic Residues are Critical for GPAT Targeting to LDs..... 78
Figure 4-6 TRP Residues Are the Only Aromatic Residues Required for Targeting 79
Figure 4-7 Alg4 Targets to LDs in a similar manner to GPAT4..... 81
Figure 4-8 W166-A203 Distance in in Bilayer and Monolayer Simulations 82
Figure 4-9 P185 Membrane Depth in Bilayer and Monolayer Simulations 84
Figure 4-10 W166-A203 Distance in Metadynamics Simulations 85
Figure 4-11 Potential of Mean Force for Association of GPAT4 Hairpin Helices. 86
Figure 4-12 Snapshots of GPAT in Bilayer and Monolayer..... 88

Figure 4-13 Summary of Single Residue Free Energies at Membrane Depths in Bilayer and Monolayer 91
Figure 4-14 Helices of R179A Mutant in Bilayer are More Associated than WT..... 93
Figure 5-1 Folding of Endophilin H0 on a Membrane..... 103
Figure 5-2 Endophilin H0 exhibits limited folding with 2 μs of simulation 105
Figure 5-3 Extended Simulations of H0 do not Achieve Full Folding..... 106
Figure 6-1 2D potential of mean force for the AA dodecaalanine (ALA-AA) system. 119
Figure 6-2 2D potentials of mean force of dodecalalanine for the BI (ALA-BI) and hENM (ALA-HENM) CG models. 120
Figure 6-3 2D potentials of mean force of dodecalalanine for the unfolded BI (ALA-BI-U) and folded hENM (ALA-HENM-F) CG models. 121
Figure 6-4 MCCG Model of dodecaalanine 123
Figure 6-5 PMFs of dodecaalanine iterative MCCG model. 125
Figure 6-6 PMFs of AA and CG models of endophilin H0..... 127
Figure 6-7 PMFs of iterative MCCG model for endophilin H0..... 128

List of Tables

Table 2-1 Amphipathic Helices Studied in this Manuscript. 29

Table 2-2 Summary of MD Simulations..... 51

Table 2-3 Summary of simulation binding times (ns) for M-domain, P2, and ALPS peptides on monolayer and bilayer membranes. 53

Table 4-1 Table of Hairpin Sequences used in this Manuscript 98

Acknowledgements

First, I would like to thank my advisor, Greg Voth, for providing me with the opportunity to conduct my Ph.D. research. Your support, both scientific and especially financial, and mentorship allowed me to focus freely on research without hinderance, with constant nudges pushing me in the correct direction. Your ability to provide an excellent research environment for such a large research group amazes me every day. I would also like to thank Suri Vaikuntanathan and Tobin Sosnick for serving on my dissertation committee.

I would also like to thank Tobi Walther and Bob Farese, for inviting Greg and me to collaborate on the lipid droplet research. It has really been a great experience working with you. I have learned more biology and experimental techniques than I ever would have expected going into my graduate degree in computational chemistry. I would especially like to thank you for welcoming me into your lab on my trips to Boston, and treating me like a member of your research group, a member of the family.

I am extremely appreciative of Coline Prévost and María-Jesús Olarte and the rest of the Walther-Farese lab for doing all of the experimental research that went into this collaboration, our research publications, and my thesis. On its own, my simulations and analysis would not mean nearly as much without the corroborating results from your experiments. Coline and MJ, I cannot thank you enough for all of the work that you've done, the many hours you spent explaining all of the technical details and implications from your results to me over skype, and the fruitful discussions we have had trying to reconcile our results. I am constantly amazed at the work you have done, and I am most appreciative for the patience and diligence you have shown throughout our work together.

Doing research every day can often be difficult and demotivating. To the Voth group members, past and present, who have helped me along the way, thank you. There are always many different pros and cons in each research group, but the best thing about the Voth group is each of its individual members, each who have different backgrounds and expertise, and who were willing to help me with whatever problems I had. Especially Glen, Rui, and Jesper, you were always there to help me with whatever problems I needed solving.

I am especially thankful for my officemates, Zack, Jacob, and Thomas, as well as honorary member Alek. You guys provided more of hours of scientific advice and help than I could have ever imagined needing. You put up with my complaining and frustrations on a daily basis, and were just friends in the best way possible. I was not always happy coming in to the office every day, but you guys made the worst days bearable, and the best days even better. I am most assuredly going to miss sitting in an office with all of you. And to Josh and Tim, I know that we have not shared an office together for so long, but within the short time we have sat together, I know that you two will continue the tradition of a tightly knit office, which will help you get through the tough times doing research when they arise.

My friends, whether within the Voth group or not, have given me some amazing times in Chicago. I have really enjoyed playing softball with the baseliners, which has been a bright spot twice-weekly when the weather has been nice. A few special thanks are in order here. Thomas and Camille, the two of you were always there for me, whether I was having a bad day or just extremely hungry. I could only ever want to spend more time hanging out with you. Tony, thanks for dragging me out of bed all those mornings to swim at the gym and listen to all of my grumblings many times a week. I often needed a way to vent my frustration, and you were always willing to listen.

Finally, I wouldn't be here today without the support of my family. Sometimes it was just really hard for me to know what I needed, but you all always did. Mom and Dad, I cannot thank you enough for the opportunities you provided for me, and the support you have given me all of these years. Isaac and Shelli, you always understood me better than everyone else, and I just can't say enough how thankful I am for all of the time that we have spent together. You were always there for me in more ways than you can realize. And lastly, Bethany, I don't know how you got me through every day, but you somehow did. I couldn't have possibly asked for a better person to spend my life with.

Abstract

Protein targeting to membranes is important for proper function in the cell. Proteins need to identify the proper biological membranes within the cell and do so through a variety of membrane bound domains, including amphipathic helices and membrane hairpin domains. In this thesis, work is presented that addresses these membrane-targeting mechanisms. Specifically, the mechanisms of protein targeting to lipid droplets (LD) are identified. LD membranes contain larger and more frequent packing defects compared to bilayer membranes due to the intercalation of neutral lipids in the phospholipid tails. This increased space in LD membranes allows for more stable insertion of all amino acids. LD membranes are therefore more promiscuous and allow a larger variety of amphipathic helices to bind. Additionally, LD proteins targeting from the ER undergo conformational change upon relocalization to LDs due to the switch from a phospholipid bilayer to a phospholipid monolayer and neutral lipid core. LD proteins that relocalize from the ER contain a concentration of large hydrophobic residues near the bilayer midplane. These residues are shifted in LD membranes towards the carbonyl region in the phospholipid tails, a more packing defect enriched area. Finally, a new method coarse-graining method is presented that allows one to accurately model the folding process of proteins using a multistate approach. This multi-configurational coarse-graining method is demonstrated for helix folding in water and can be extended to study amphipathic helix binding and folding on biomembranes.

Chapter 1. Introduction

1.1 Lipids and Lipid Membranes

Lipids are a broad class of biomolecules that are insoluble or only slightly soluble in water. Lipids primarily perform three functions in the cell: 1) lipids form membranes to segregate the cell from the environment and compartmentalize the cellular organelles; 2) lipids are the primary long-term storage mechanism of the cell; and 3) lipids are involved in many cell signaling pathways (Voet et al., 2013).

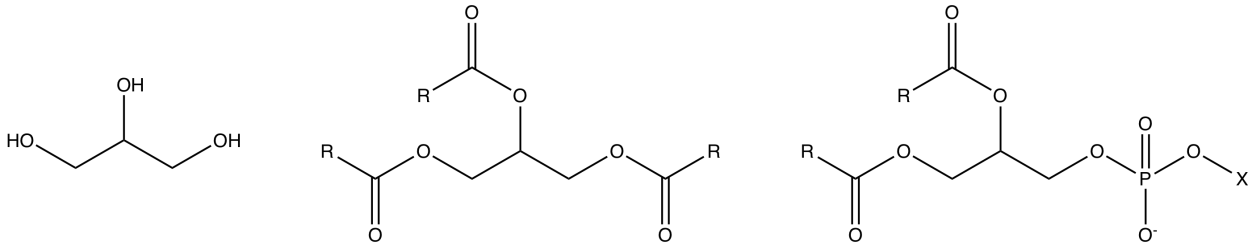

Glycerol **Triacylglycerol** **Glycerophospholipid**

Figure 1-1 Structure of Glycerolipids
Schematic diagram of glycerol, a triacylgerol, and a glycerophospholipid.

Lipids come in a number of different biological forms, including fatty acids, glycerolipids, and phospholipids (PL), sphingolipids, and sterols. Glycerol, a simple organic compound with three hydroxyl groups, forms the backbone for glycerolipids and phospholipids. It can form a diverse set of lipids depending on the fatty acids and phosphoryl groups it is bonded to at the hydroxyl groups. Fatty acids, carboxylic acids with long hydrocarbon chains, occur with various hydrocarbon lengths (though most commonly between 14 and 20 carbons in length) as well as with various degrees of unsaturation (Figure 1-2). Phosphoryl groups consist of a phosphate bonded to a polar group or hydrogen.

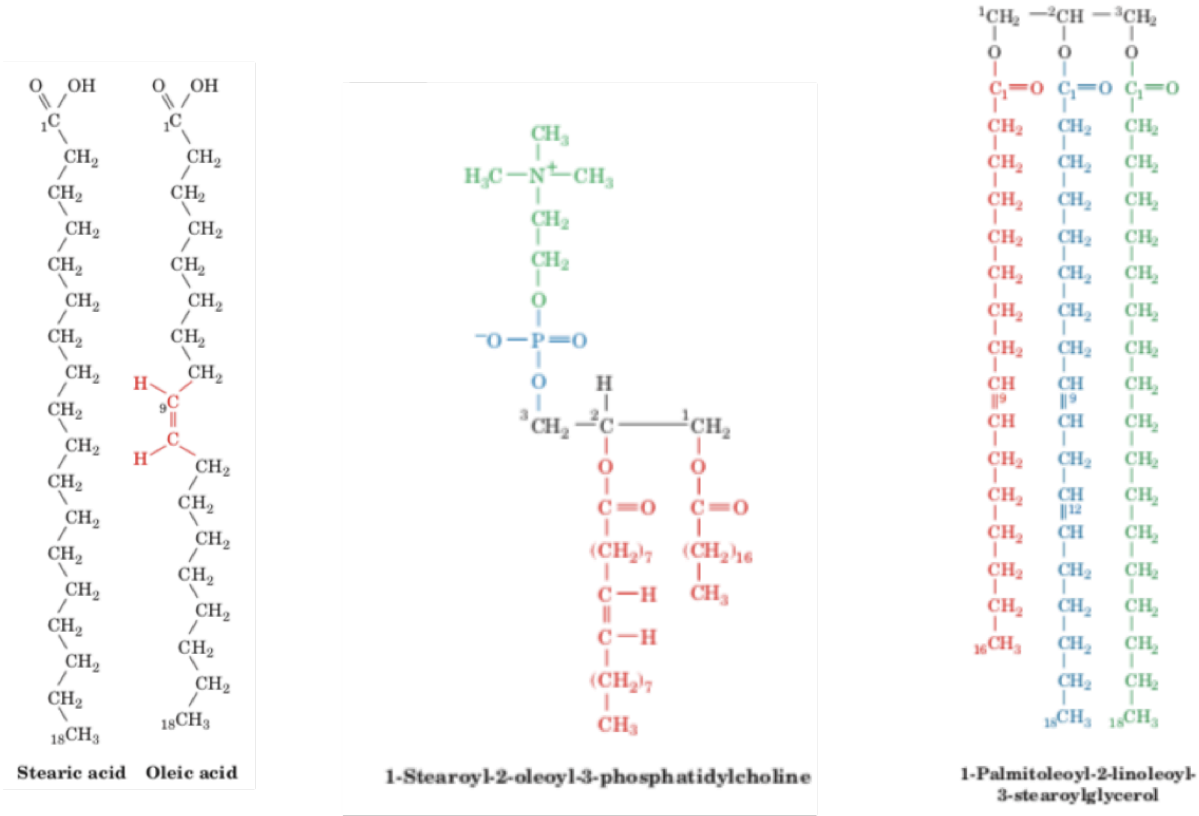

Figure 1-2 Structure of Fatty Acids, Phospholipids, and Triacylglycerols
Schematic diagram of two fatty acids (left), a phospholipid (center) and a triacylglycerol (right), adapted from (Voet et al., 2013).

Glycerols can be linked by up to three fatty acids to form monoacylglycerols, diacylglycerols, and triacylglycerols. These glycerolipids are hydrophobic and serve as a form of energy storage for the cell, as energy is released by the hydrolysis of the esterified fatty acid. Glycerophospholipids consist of a glycerol backbone, with fatty acids linked at the first and second carbon, and a phosphate group at the third carbon. Glycerophospholipids are amphiphilic and are therefore a major component of biomembranes, segregating various biological compartments from each other. Sphingolipids contain a sphingosine backbone and can be amide

linked to a fatty acid as well as linked to a phosphate group. Sterols, a subgroup of steroids, can also be esterified with fatty acids into sterol esters.

1.2 Emulsions and Lipid Droplets

Emulsions are formed when two immiscible fluids are mixed, and one of the fluids is dispersed in the form of droplets within the other. Cells turn fatty acids, which can act as detergents, into neutral lipids such as triacylglycerols and sterol esters. But these hydrophobic oils would naturally form an emulsion within the largely water cytosol (Thiam et al., 2013b). To reduce surface tension and generate more stable emulsions, surfactants are required. In the cell, a phospholipid monolayer acts as the surfactant, segregating the hydrophobic neutral lipids from the cytosol, forming lipid droplets. Lipid droplets can vary significantly in size, from hundreds of nanometers in diameter in yeast, to tens of microns in diameter in adipose tissue.

The neutral lipids with the lipid droplet core are primarily composed of triacylglycerols (TG) with a smaller portion of sterol esters (SE). The phospholipid monolayer composition is quite similar to composition of the endoplasmic reticulum. It is primarily composed of phosphatidylcholine (PC) and phosphatidylethanolamine (PE).

Lipid droplets are formed from the ER, where neutral lipids are synthesized (Walther and Farese, 2012). Current models (Wilfling et al., 2014) suggest the formation of lipid droplets occurs in three steps: 1) synthesis of neutral lipids within the ER; 2) aggregation of neutral lipids with the ER accompanied by lens formation; and 3) droplet formation and scission. The synthesis of neutral lipids within the ER is catalyzed by a number of different enzymes for each step of the Kennedy pathway for TG synthesis (Wilfling et al., 2014). Once a sufficient number of neutral lipids have aggregated within the ER, lens formation followed by droplet formation

can occur. Lipid droplets can grow in size depending on the needs of the cell, and therefore require enzymes for TG synthesis as well as for PC synthesis. Once lipid droplets have separated from the ER, they have been shown to reform connections to the ER to acquire enzymes for TG synthesis. This thesis thoroughly investigates how these proteins target to lipid droplets.

1.3 Protein Targeting to Membranes

Proper cellular function requires proteins to accurately target to specific locations and organelles within the cell. There are a number of mechanisms by which proteins target within the cell. Bin/amphiphysin/rvs (BAR) domain-containing proteins are characterized by a banana-shaped curved domain that targets to and stabilizes curved membranes (Simunovic et al., 2015). Many BAR domain-containing proteins also use amphipathic helices (AH), which insert into the membrane, stabilizing the protein on the surface of the membrane. Other proteins, such as protein kinases (Li et al., 2014; Ziemba et al., 2014), target to membranes and bind to specific lipids, often phosphoinositides (PI). Proteins binding to PI lipids often contain widely shared domains, such as pleckstrin homology (PH) domains, which specifically bind to PI lipids (Lai et al., 2013).

Amphipathic helices are another common motif found in proteins that bind to membranes. Amphipathic helices are normally disordered when in bulk water, but fold upon binding to membranes (Fernandez-Vidal et al., 2007; Hristova et al., 1999). They characteristically have a hydrophobic face as well as a polar face, which drives helix formation upon binding to phospholipid membranes (Figure 1-3). Folding of an AH allows the two faces of the AH to partition between the polar headgroups and hydrophobic tails of the PLs. The mechanism of AH binding to membranes requires a number of steps. First, a single (likely large) hydrophobic

residue on the amphipathic helix locates a lipid packing defect on the surface of the membrane that is large enough for it to insert (Vanni et al., 2013). This first step occurs quite quickly, within hundreds of nanoseconds, upon approaching the membrane. Next, the AH folds into the interfacial region of the membrane. The lipid packing defect in which the residue has inserted is enlarged as surrounding residues are folded into the membrane (Cui et al., 2011). This step occurs on timescales greater than 10 μs, making the study of this process using molecular dynamics simulations quite difficult. This step is energetically favorable (Almeida et al., 2012; Cui et al., 2011; Fernandez-Vidal et al., 2007; Ladokhin and White, 1999). Proteins containing AH are therefore only likely to be removed from the membrane on highly crowded membrane surfaces, where proteins with e.g. transmembrane domains bump off the AH-containing proteins from the membrane. Subsequently, the amphipathic helix would unfold due to the increase in entropy achieved in the disordered state, beginning the cycle anew.

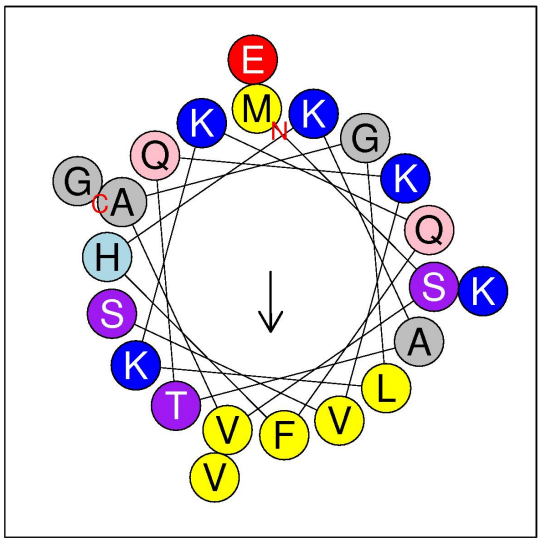

Figure 1-3 Helical Wheel Plot of Endophilin H0
A wheel plot of the endophilin amphipathic helix, generated using Heliquest(Gautier et al., 2008). The hydrophobic residues (yellow) are localized on one face of the helix, partitioning the helix between the polar headgroups and hydrophobic tails of phospholipids. The arrow depicts the hydrophobic face, which interacts with the hydrophobic tails.

Lipid droplet proteins are not translated on directly on the lipid droplets, but are instead translated either within the ER (Class I) or the cytosol (Class II) (Kory et al., 2016). Class I proteins contain membrane embedded domains and re-localize to LDs from the ER through membrane bridges. In the absence of LDs in the cell, these proteins are predominantly found in the ER. Class II proteins target to LDs via amphipathic helices. AH targeting to bilayer membranes has been extensively studied, though the different surface properties of LDs likely affect this targeting mechanism.

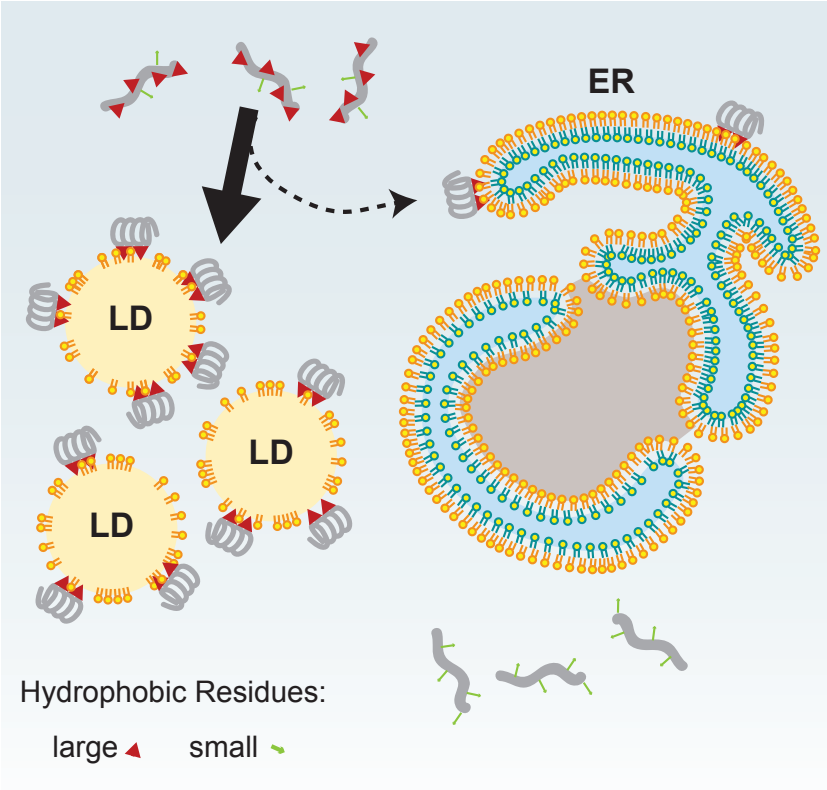

Figure 1-4 Schematic of Amphipathic Helices Targeting to Lipid Droplets
Amphipathic helices prefer to target to lipid droplets (LD) as opposed to the ER, due to the increase in packing defects on the surface (Prevost et al., 2018).

1.4 Enhanced Sampling and Free Energy Sampling Techniques

One common issue that arises when trying to simulate some of the biophysical phenomena noted above is that current computer hardware limits the simulation size and simulation length. Typical hardware currently allows one to simulate a system of up to a few million atoms for up to a few microseconds. But many of the biological phenomena of interest occur on longer timescales, presenting a challenge for how these systems can be studied. Specialized hardware, such as the Anton (Shaw et al., 2009) supercomputer, allows the simulation of systems on the order of 100k atoms for hundreds of microseconds or even up to milliseconds. A number of simulations within this thesis have extensively used the Anton supercomputer for long time simulations, though access to this machine is limited

Therefore, a number of techniques have been developed within the last few decades to enhance the sampling of certain phenomena within accessible computational power. These methods include replica exchange molecular dynamics (Sugita and Okamoto, 1999), metadynamics (Laio and Parrinello, 2002b), and umbrella sampling (Torrie and Valleau, 1977). Each method has its own advantages and disadvantages, though many rely on accurately describing the phenomena of interest using a collective variable (a.k.a. order parameter or reaction coordinate)(Bernardi et al., 2015). Poor choice of a collective variable will often lead to problems in sampling, especially when orthogonal degrees of freedom are slow to relax.

The potential of mean force (PMF) along a collective variable (CV) can be obtained using umbrella sampling(Torrie and Valleau, 1977), where independent replicas are run with harmonic restraints placed on the CV, centered at various points along the CV. The unbiased potential of mean force can then be obtained by subtracting out the bias from the biased potential of mean force for a system with a single umbrella potential applied. For a series of simulations with

different umbrella potentials added, the potential of mean force can be calculated using the weighted histogram analysis method (Grossfield; Kumar et al., 1995; Roux, 1995) (WHAM) or multistate Bennett acceptance ratio (Bennett, 1976; Shirts and Chodera, 2008) (M-BAR).

Replica exchange molecular dynamics (REMD) (Sugita and Okamoto, 1999), a common enhanced sampling technique, uses multiple independent replicas running concurrently, with exchanges attempted between replicas every certain number of steps, with the acceptance based upon the metropolis criterion $\min\left(1, e^{-\beta \Delta U}\right)$. Typically, each replica is run at a different temperature (T-REMD), such that sampling is greatly enhanced at higher temperatures. Each replica can then explore conformational space quickly at higher temperatures, and, when exchanged back down to the lowest temperature replica, the equilibrium distribution at physiological temperature can be obtained. REMD can be generalized to simulate each replica with a separate Hamiltonian (Ostermeir and Zacharias, 2013; Roe et al., 2014; Sugita et al., 2000) (H-REMD) so that coordinates other than temperature can be explored. For example, a common perturbation of the Hamiltonian is captured with Solute Tempering (Liu et al., 2005), where the exchange criterion is not dependent upon the number of water molecules in the system, which can be quite important for adequate sampling for large systems. One significant advantage of REMD is that the replicas are all run in parallel, limiting the calendar time spent acquiring results. Additionally, T-REMD does not require a choice of collective variable, which can be quite advantageous when investigating a process that is difficult to describe using only one or two CVs. But, inadequate choice of the maximum temperature or the exchange rate can lead to a more computationally expensive simulation.

Another commonly used enhanced sampling technique is metadynamics(Laio and Parrinello, 2002b). Metadynamics adds biasing potentials in the shape of gaussian hills as it traverses CV

space (i.e. it fills up free energy minima with “computational sand” (Darve and Pohorille, 2001)), allowing the system to escape local minima (Figure 1-5, as shown in (Bernardi et al., 2015). Upon filling up the entire free energy landscape, the bias that has been added to the system can be inverted, resulting in the PMF of the system. There are a number of variants to metadynamics that improve upon some of its deficiencies, to ensure convergence, relevant sampling, and efficient sampling within the PMF of interest, which are not guaranteed with standard metadynamics. Well-tempered metadynamics (Barducci et al., 2008) decreases the size of the gaussian hill as a function of the simulation time, ensuring convergence to the PMF asymptotically (Dama et al., 2014a). Transition-tempered metadynamics (Dama et al., 2014b) improves (Sun et al., 2016) upon well-tempering by waiting to temper until transitions have been observed between free energy minima, decreasing the simulation time spent filling free energy basins while still maintaining convergence. Metabasin metadynamics (Dama et al., 2015) prevents exploration into unphysical regions of conformational space which in turn inhibits irreversible changes occurring to the system. Bias exchange metadynamics (Piana and Laio, 2007) incorporates the principles of REMD, where each replica samples a different CV with exchanges occurring between replicas in order to accurately sample transitions that cannot be accurately described with one or two CVs. Depending on the complexity and specificity of the biophysical phenomena of interest, the different variants of metadynamics may provide more accurate results.

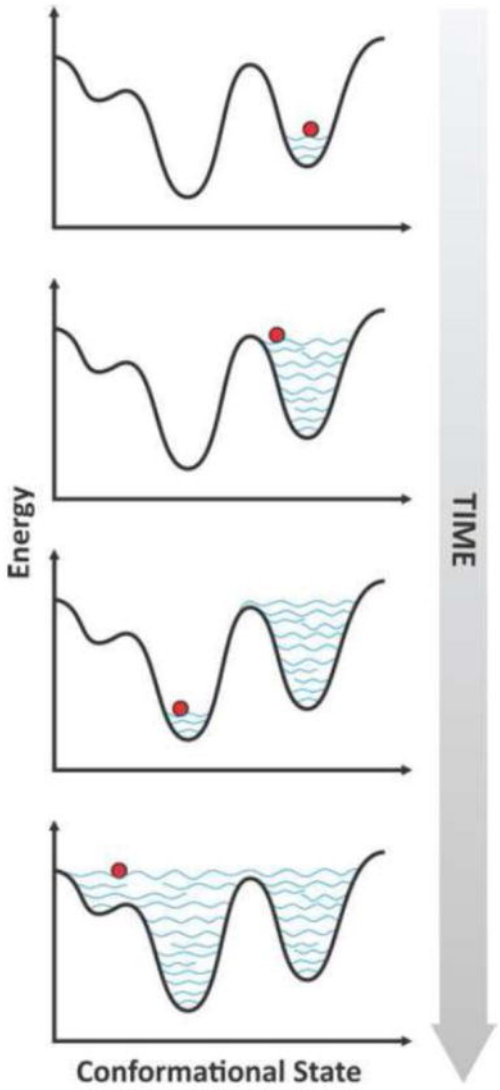

Figure 1-5 Schematic of Metadynamics Free Energy Sampling
Metadynamics first fills the free energy well it is currently in. Once it has added enough bias to its current well, it can diffuse across the free energy barrier into the adjacent well. Upon filling up the entire surface, the system will freely diffuse along the reaction coordinate.

1.5 Thesis Aims and Chapters

The aim of this thesis is to understand how and why proteins target to specific membranes within the cell. I used different molecular dynamics simulation techniques to investigate these biological mechanisms. Most of the work within this thesis was done in collaboration with the

joint research lab of Tobias C. Walther and Robert V. Farese Jr. (Harvard Medical School). The experiments were primarily conducted by Coline Prévost and María-Jesús Olarte.

In chapter 2, I show the mechanism of amphipathic helix-containing proteins targeting to lipid droplets. In chapter 3, I describe the differences in permeation free energy for amino acids in bilayer and lipid droplet membranes. Chapter 4 discusses how proteins with membrane-embedded hairpin domains relocalize from the ER to lipid droplets. Chapter 5 explains how amphipathic helix folding on bilayer membranes is a significant challenge even with long time molecular dynamics simulations. Chapter 6 presents a novel method for modeling protein folding with coarse-grained molecular dynamics.

Chapter 2. Mechanism and Determinants of Amphipathic Helix-Containing Protein Targeting to Lipid Droplets

This chapter is adapted from (Prevost et al., 2018)

2.1 Summary

Cytosolic lipid droplets (LDs) are the main storage organelles for metabolic energy in most cells. They are unusual organelles that are bounded by a phospholipid monolayer and specific surface proteins, including key enzymes of lipid and energy metabolism. Proteins targeting LDs from the cytoplasm often contain amphipathic helices, but how they bind to LDs is not well understood. Combining computer simulations with experimental studies *in vitro* and in cells, we uncover a general mechanism for targeting of cytosolic proteins to LDs: large hydrophobic residues of amphipathic helices detect and bind to large, persistent membrane packing defects that are unique to the LD surface. Surprisingly, amphipathic helices with large hydrophobic residues from many different proteins are capable of binding to LDs. This suggests that LD protein composition is additionally determined by mechanisms that selectively prevent proteins from binding LDs, such as macromolecular crowding at the LD surface.

2.2 Introduction

Lipid droplets (LDs) are cytoplasmic organelles that store neutral lipids, such as triacylglycerols (TGs) or sterol esters, which serve as reservoirs of lipids for cell proliferation or energy (Pol et al., 2014; Walther and Farese, 2012). The number and size of LDs vary greatly in cells, depending on the metabolic state, and LD accumulation in tissues, such as the adipose tissue and liver, is the hallmark of obesity. In addition to their function in energy metabolism, LDs are involved in a host of other cellular functions, such as maintaining proteostasis and as signaling

hubs (Welte, 2015). Knowledge of basic LD biology is thus a fundamental aspect of cell biology, with important implications for our understanding of the pathogenesis of metabolic diseases and for engineering storage of neutral lipid oils in LDs for industrial purposes (Gluchowski et al., 2017; Krahmer et al., 2013a)

LDs comprise a neutral lipid core bounded by a phospholipid monolayer, which sets them apart from most other organelles that instead have a bilayer membrane. The phospholipid monolayer is derived from the cytosolic face of the ER, and its composition is similar to the ER lipid composition (Bartz et al., 2007; Choudhary et al., 2015). Many proteins target to the LD monolayer where they carry out crucial functions. For example, correct targeting of proteins is key for synthesizing or hydrolyzing TGs at the organelle surface (Kory et al., 2016). LD proteins differ between organisms and cell types, but generally include structural and regulatory proteins and enzymes of lipid metabolism (Brasaemle et al., 2004; Fujimoto et al., 2004; Kory et al., 2016; Krahmer et al., 2011; Krahmer et al., 2013b; Wilfling et al., 2013). How these proteins recognize and target to the LD surface is an important unanswered question of cell biology.

Current models posit two distinct pathways by which proteins target to the surface of LDs (Kory et al., 2016). In one pathway (Class I), proteins are initially inserted into the ER membrane and subsequently re-localize as membrane-embedded proteins from the ER to the LD surface using physical continuities between the two organelles, known as membrane bridges (Jacquier et al., 2011; Thiam et al., 2013a; Wilfling et al., 2013). Consistent with their biochemical behavior as integral membrane proteins, cargoes of this pathway are characterized by stretches of highly hydrophobic amino acids with the potential to form membrane-embedded domains, possibly hairpin loops. Examples of Class I proteins include GPAT4 and DGAT2, enzymes involved in TG synthesis (Wilfling et al., 2013), and the methyltransferase ALDI (Zehmer et al., 2008).

In a second pathway (Class II), proteins are translated in the cytoplasm and subsequently directly bind the LD surface. Members of this class include the structural and regulatory perilipin proteins, as well as important metabolic enzymes (e.g., CCT enzymes 1 and 2) (Bickel et al., 2009; Kimmel and Sztalryd, 2016; Krahmer et al., 2011; Miyanari et al., 2007; Ohsaki et al., 2016; Rowe et al., 2016). These proteins typically contain sequences with a propensity to form amphipathic helices or short stretches of hydrophobic residues that are required for LD binding (Kory et al., 2016).

How these cytoplasmic proteins recognize and bind to the LD surface is largely unknown. The LD targeting pathway is likely unique as LDs do not have dedicated protein targeting/import machinery, such as the translocon or the TOM/TIM import channel for targeting of proteins to the ER or mitochondria, respectively. Nor do LDs apparently have specific lipids that serve as spatial organelle identity markers, such as phosphoinositides, that could be bound by targeting domains, such as PH domains. Given this, it remains unclear how LDs achieve their specific protein composition.

Here we combined computational and experimental approaches to unravel how LD surfaces differ from membrane bilayers surfaces and to identify mechanisms for targeting proteins to LD monolayers. Our data indicate that LDs exhibit distinctive surface properties that distinguish them from membrane bilayers and that these features of LD monolayers are recognized by cytosolic proteins with amphipathic helices containing large hydrophobic residues, thus providing a general mechanism for LD targeting of class II proteins. Surprisingly, many amphipathic helices are able to bind LDs in isolation, indicating promiscuity in binding and highlighting the need for mechanisms to prevent erroneous targeting and to maintain the LD proteome.

2.3 Results

2.3.1 Molecular Dynamics Simulations Reveal that LD Surfaces Exhibit Numerous, Large Phospholipid Packing Defects

Because targeting of class II proteins to LDs does not seem to involve specific protein machinery or lipid markers, we hypothesized that LD proteins with AH motifs might detect global surface properties that are specific to LDs. To identify such features, we performed all-atom molecular dynamic (MD) simulations of LD surfaces (a summary of all the simulations run is presented in Table S1). Because the relatively large size of LDs prohibits the study of entire LDs in MD simulations due to limitations in computing power, we modeled the behavior of LDs by inserting a layer of neutral lipids, composed of 1:1 triolein (TRIO) and cholesteryl oleate (CO), inside of a flat bilayer, composed of 65:27:8 palmitoyl-oleoyl phosphatidylcholine (POPC): dioleoylphosphatidylethanolamine (DOPE): stearoyl-arachidonoyl phosphatidylinositol (SAPI) (Figure 2-1A), a previously demonstrated technique for simulating LD surfaces (Bacle et al., 2017; Hennere et al., 2005; Hennere et al., 2009; Koivuniemi et al., 2009). To determine the smallest system that exhibits LD surface properties, we varied the thickness of the neutral lipid layer. These analyses revealed that a 4-nm thick layer of neutral lipids was sufficient to change the properties of the phospholipid monolayers on each side, and that increasing this layer further did not lead to additional changes (see also below and Figure 2-7). Specifically, modeling LDs with these conditions revealed that inclusion of neutral lipids increased the surface area per phospholipid from 67 $Å^2$ for bilayer membranes to 71 $Å^2$ for monolayers of the same phospholipid composition. This increase results from the significant mixing between the neutral lipids and the phospholipids chains, illustrated by the z-density profile of the 4-nm-thick LD in

Figure 1B. This finding is in agreement with the results of a recent report (Bacle et al., 2017). A snapshot of the simulation (Figure 2-1A) shows an example of a neutral lipid that has inserted all the way to the solvent exposed region, causing a packing defect on the surface of the membrane. Our simulations, thus, support a model in which the physical surface properties of LDs are distinct from that of bilayer membranes as LDs expose a rougher interface towards the aqueous cytosol, with a looser packing of surface phospholipids.

To further explore this possibility, we calculated the probability of observing hydrophobic lipid packing defects on the LD and on the bilayer surface based on our simulation data. We defined packing defects by mapping the phospholipid hydrocarbon tails exposed to the solvent and projecting them on the plane of the membrane (Cui et al., 2011). We refer to the area of these defects as "defect size". Using this metric, LD monolayers show significantly more large packing defects than bilayer membranes (Figure 2-1C), as reported (Bacle et al., 2017). When we analyzed the persistence of packing defects, we found that defects with a life-time of more than 5 ns, the time scale of initial protein interaction with the membrane (Vanni et al., 2013), were more frequent on the monolayer than on the bilayer surface (Figure 2-1D). This suggests that the probability of a peptide productively encountering a large packing defect is much greater in such monolayer membranes than in bilayer membranes.

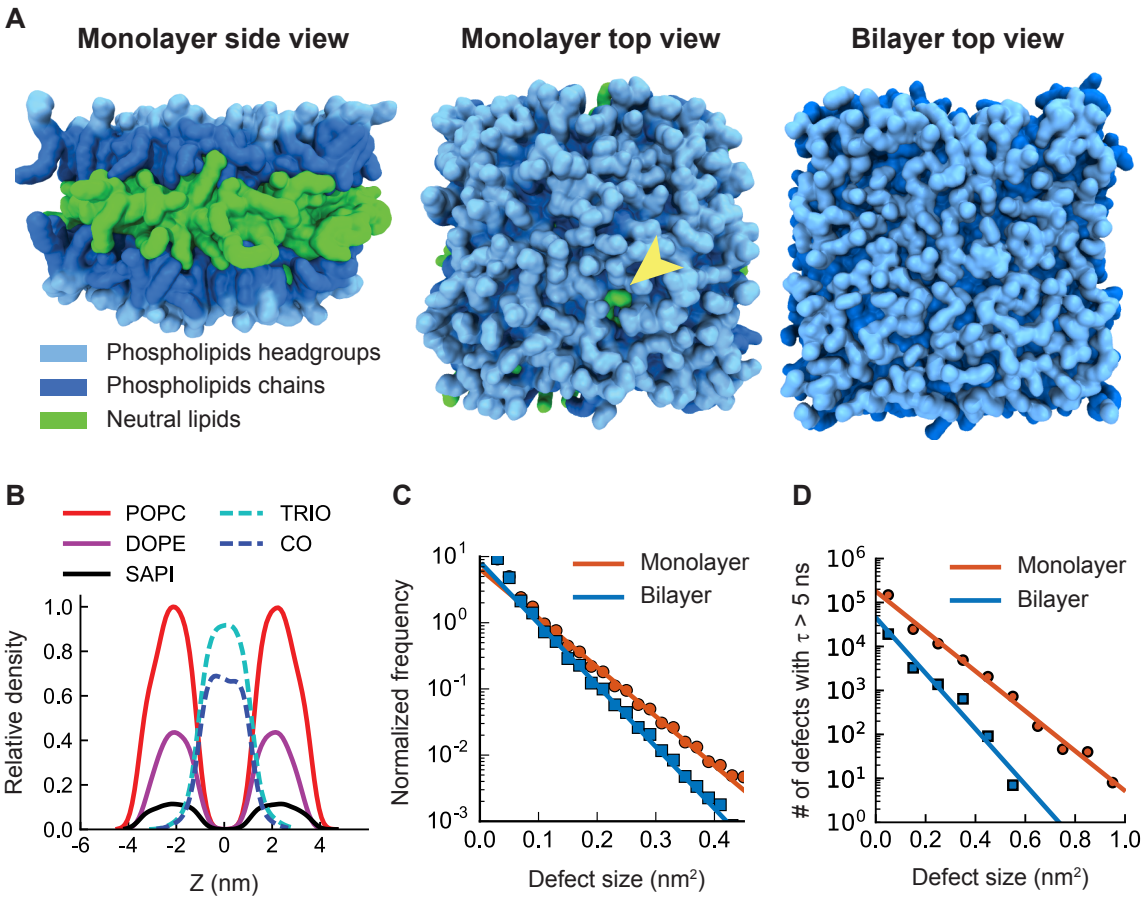

Figure 2-1 Molecular Dynamics Simulations Reveal that LDs Have Larger and More Persistent Surface Packing Defects than Bilayer Membranes.

(**A**) Simulation snapshots of the monolayer system (phospholipids: 65:27:8 POPC:DOPE:SAPI, neutral lipids: TG:SE 1:1, neutral lipid thickness: 4nm). Arrow indicates a neutral lipid that has inserted all the way to the surface.

(**B**) z-Density profile for the 4-nm LD. The relative density is normalized by the maximum number density. Note the mixing between the neutral lipids and the tails of the phospholipids. See also Table S1 for a summary of all simulations run.

(**C**) Distribution of packing defect sizes for bilayer and LD surfaces. The monolayer exhibits increases in the frequency of larger defects. Normalized frequency: number of defects for a given size range is normalized by the total number of defects over the simulation time frame. Solid lines are least-square fits to exponential decays. See also Figure S1.

(**D**) Distribution of packing defect sizes taking into account only the defects with characteristic lifetimes,τ, longer than 5 ns. Compared with the defects on the bilayer, the defects on the monolayer are roughly 10 times as likely to last longer than 5 ns for all defect sizes. Solid lines are least-square fits to exponential decays.

2.3.2 Initial Binding of the CCTα Amphipathic Helix to the LD Surface in Molecular Dynamics Simulations

We next used MD simulations to analyze the initial binding of amphipathic helices to the LD surface. For bilayer membranes, such simulations suggest a pathway that has several distinct steps (Tang et al., 2007; Ulmschneider et al., 2010; Vanni et al., 2013; Voth, 2013; White and Wimley, 1998). In the first step, the peptide, which is unfolded in solution, is often attracted to the membrane due to electrostatic forces. Next, hydrophobic residues of the targeting sequence adsorb onto hydrophobic packing defects of the phospholipid bilayer. In the last step of binding, the sequence around the inserted residue folds into an amphipathic α-helix, resulting in stable binding to the bilayer surface.

We hypothesized that targeting sequences of class II proteins have a high likelihood to similarly interact with packing defects at the surface of monolayer membranes. To test this hypothesis, we performed MD simulations of peptide-monolayer interactions, using the amphipathic helix of the LD-binding metabolic enzyme CCTα (Krahmer et al., 2011) as a model peptide. In four independent simulations, we placed this peptide (referred to as the M-domain) at least 2 nm from the membrane in a random coil conformation. We considered that binding was successful if hydrophobic residues inserted into the membrane below the plane of the phospholipids phosphates (an example is shown on the simulation snapshot Figure 2-2A) and did not dissociate from the membrane within the timeframe of our simulation (750 ns). If no insertion occurred, or if a residue inserted but subsequently dissociated, the simulation was scored as an instance where binding was unsuccessful (see an example for each case in Figure 2-8). In three of the four simulations, we observed binding of the M-domain to the LD surface within the timeframe of our simulations (Figure 2-2C). In each case where binding occurred, a

large, but not necessarily the same, hydrophobic residue (F53 twice and L34 once) was first to insert into a packing defect. Additionally, in one of the four simulations, we observed the initial stages of amphipathic helix folding within the time window of our simulations (data not shown).

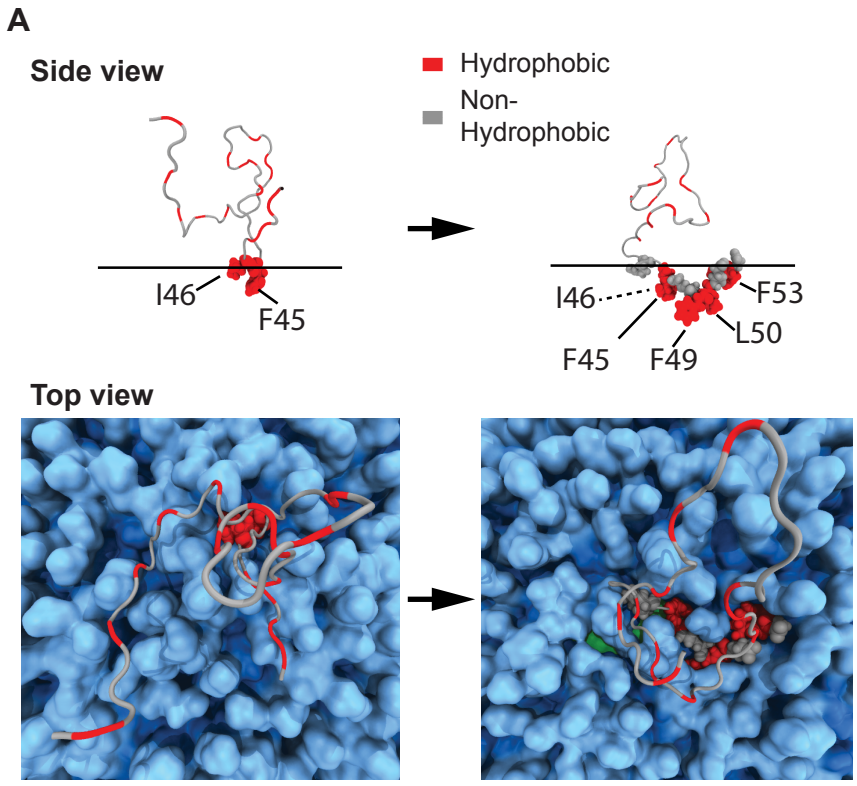

Figure 2-2 Molecular Dynamics Simulations Show that Amphipathic Helices Insert Bulky Hydrophobic Residues into Large Lipid Packing Defects
(**A**) Representative sequence of insertion of a stretch of residues from the M-domain into the LD surface. The inserting residues are depicted in a space-filling representation, and the rest of the peptide is depicted by a ribbon. The horizontal line in the side view represents the phosphate level. Residues labeled are the hydrophobic residues that have inserted below the phosphate plane. See also Movie S1.

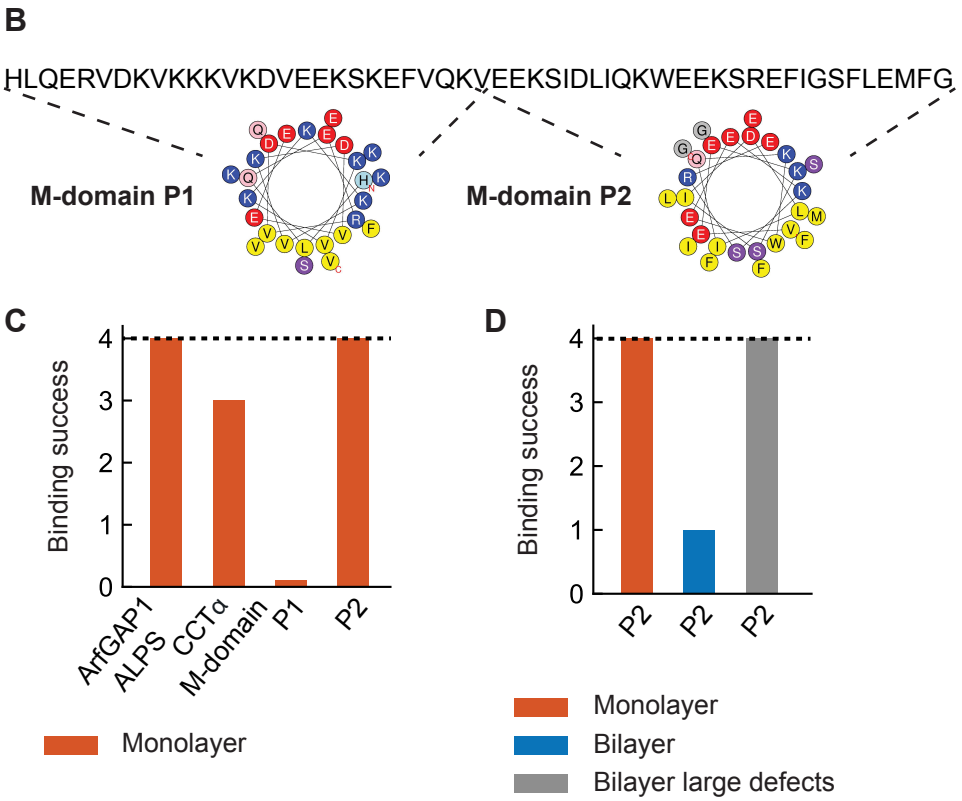

Figure 2-2 Cont.
(**B**) Amino acid sequence of the M-domain and helical plots of both halves (P1 and P2). Dashed lines indicate the ends of both peptides within the full M-domain sequence.
(**C**) Binding success of AHs with (ArfGAP1 ALPS, M-domain, P2) or without (P1) large hydrophobic residues at the LD surface in MD simulations. Binding success is defined as the number of simulations in which at least one residue inserted in the lipid monolayer and remained inserted for the duration of the simulation. See also Figure S2 and Table S2. A total of four simulations were run for each peptide.
(**D**) Binding success of P2 to different surfaces. Monolayer: phospholipids: POPC:DOPE:SAPI 65:27:8, neutral lipids: TG: SE 1:1, bilayer: POPC: DOPE: SAPI 65: 27: 8, bilayer large defects: DOPC: DOG 85: 15. See also Tables S1 and S2.

2.3.3 Insertion of Large Hydrophobic Residues into Packing Defects Mediates LD Protein Binding

Based on our initial studies, we hypothesized that large hydrophobic residues (i.e., I, F, L, M, W, Y) in the sequences forming amphipathic helices interact with packing defects and, thus, are

responsible for recognizing the LD surface. Within the M-domain, 10 such large hydrophobic residues are found in the second half of the sequence that we designated "P2" (Figure 2-2B; similar to "PEPC22" of (Dunne et al., 1996)). In the computational studies, initial binding of P2 to LDs occurred in each of four simulations (Figure 2-2C). In contrast, the N-terminal half of the M-domain, "P1" (Figure 2B; similar to "PEPNH1" of (Dunne et al., 1996)), with only two large hydrophobic residues, did not bind LDs in our simulations (Figure 2-2C). To further test our hypothesis, we analyzed the AH of another LD-targeting protein, ArfGAP1 (Gannon et al., 2014), which contains eight large hydrophobic residues. This peptide, known as the ALPS domain (Bigay et al., 2005), bound in each of four simulations (Figure 2-2C).

These findings suggest that specific targeting of amphipathic helices with large hydrophobic residues to LDs results from the higher prevalence of packing defects on monolayer than bilayer membranes. To test that, we analyzed P2 binding to lipid bilayer membranes and found that it occurred in only one of four simulations (Figure 2-2D). Consistent with previous experimental data (Dunne et al., 1996), this finding indicates that P2 can bind bilayer membranes, but does so with a lower probability than that for binding to monolayers. To confirm that differences in the amount of packing defects caused the difference in binding to monolayers and bilayers, we included 1,2-dioleoyl-sn-glycerol ((DOG), a conical lipid that increases packing defects (Vamparys et al., 2013)) in the simulation of binding to a bilayer membrane. In this case, P2 binding occurred in all instances of the simulation (Figure 2-2D).

2.3.4 Amphipathic Helix Binding to Phospholipid Surfaces *In Vitro* Depends on Large Hydrophobic Residues Recognizing Membrane Packing Defects

To test the MD findings experimentally, we assayed binding of labeled peptides to monolayer and bilayer membranes in several *in vitro* assay systems. We first generated artificial LDs, mixed them with synthesized, fluorescently labeled peptides and assayed binding to the surface by fluorescence microscopy. In these assays, and consistent with our simulations, P2, but not P1, bound to a large fraction of LDs (Figure 2-3A). When large hydrophobic residues (F, L or I) were introduced into P1 ("P1 Large Hydrophobics (LH)", see Table 2-1), this peptide also bound to LDs (Figure 2-3A). Conversely, when we mutated most of the large hydrophobic residues in P2 to V ("P2 Small Hydrophobics (SH)", see Table 2-1), binding was abolished (Figure 2-3A). In these experiments, we sometimes found large variations in the LD binding signal, most likely due to heterogeneous phospholipid coverage among different LDs in the sample. Supporting this interpretation, only the P2-binding population persisted in experiments in which the LD preparation lacked phospholipids (i.e., artificial TG droplets without a phospholipid monolayer; data not shown).

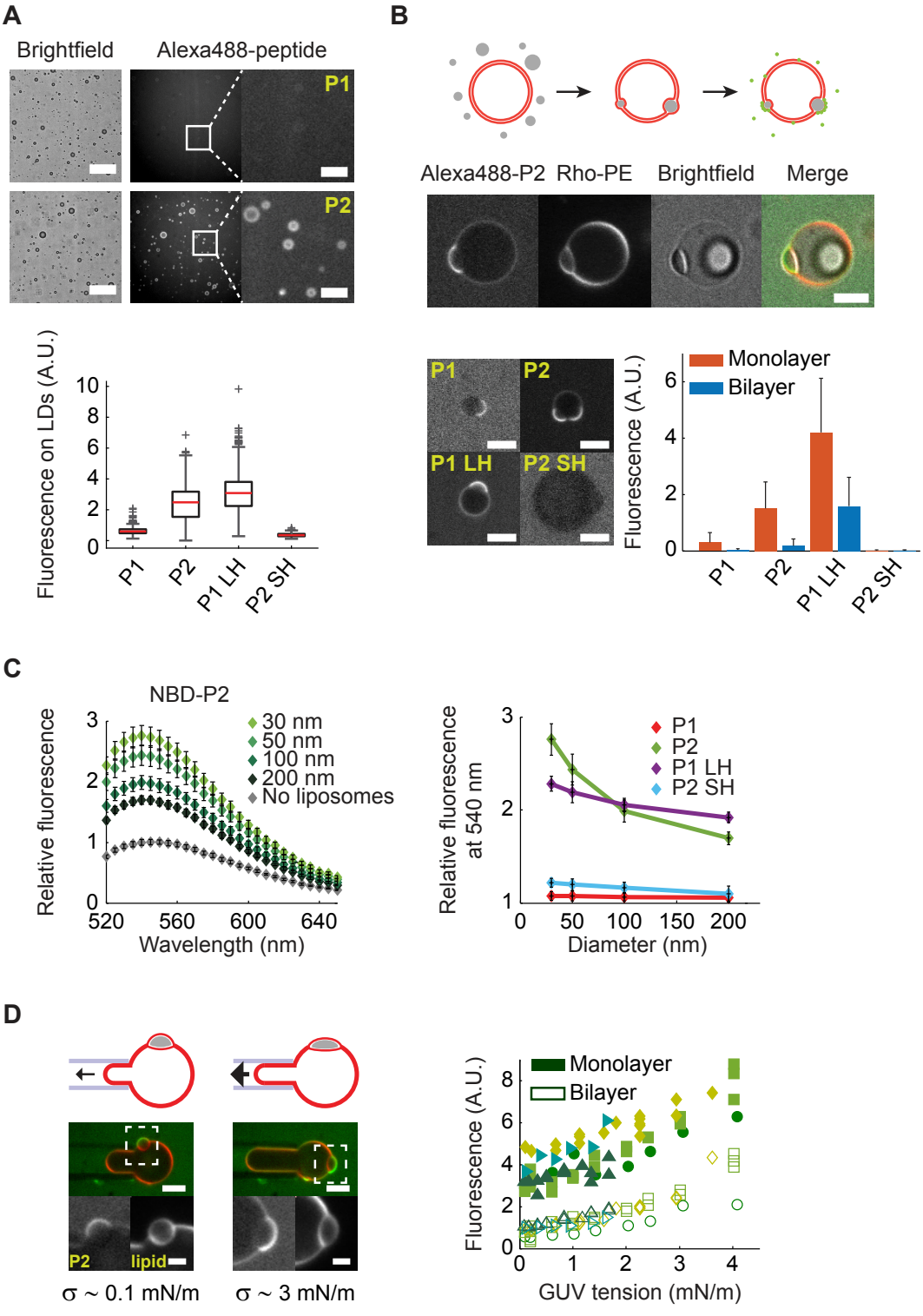

Figure 2-3 Amphipathic Helix Sequences with Large Hydrophobic Residues Bind LDs and Packing Defect-Rich Membranes in *In Vitro* Systems

Figure 2-3 **Cont.**
(**A**) Binding of AHs with (P2, P1 LH) or without (P1, P2 SH) large hydrophobic residues to artificial lipid droplets. Emulsion droplets prepared from a mixture of triolein and phospholipids (POPC: DOPE: liver phosphatidylinositol (liver PI) 65: 27: 8) were incubated with Alexa488-labeled synthetic peptides and imaged by fluorescence confocal microscopy. Upper panel: bright field and confocal images of the droplets after incubation with Alexa488-P1 and -P2. The inset highlights the ring-shaped protein signal. Lower panel: boxplot representation of the fluorescence signal on droplets. Over 200 droplets per condition were quantified in each of two independent experiments. Scale bar, 50 μm (larger field), and 10 μm (inset).
(**B**) Binding of AH peptides to a membrane-LD system. GUVs (POPC: DOPE: liver PI 65: 27: 8) were incubated with an emulsion of triolein in buffer, and the resulting TG-containing GUVs were incubated with labeled AHs and imaged with fluorescence confocal microscopy. Top: schematic of the experimental protocol. Middle: Representative image of a TG-loaded GUV after incubation with Alexa488-P2. Confocal images show the peptide and phospholipid signals. Two membrane-embedded droplets are visible in the bright field image, however only the one in focus is visible in the confocal images. Bottom left: representative images for each peptide. The protein channel is shown (see also Figure S3A for more examples); Bottom right: quantification (mean and standard deviation) of the fluorescence signal at the surface of the LD and membrane. 10–40 GUVs were imaged in each of two independent experiments. Scale bar, 5 μm.
(**C**) Binding of AH peptides to liposomes of increasing curvature. Liposomes (POPC: DOPE: liver PI 65: 27: 8) of different curvatures were incubated with NBD-labeled peptides and fluorescence emission spectra of the resulting mixtures were recorded. Left: normalized fluorescence emission spectra of NBD-P2 in the presence and absence of liposomes. Right: normalized fluorescence emission signal at 540 nm as a function of the extrusion pore diameter. Mean and standard deviation from three independent experiments with duplicate measurements are shown. Fluorescence values at each wavelength were normalized by the fluorescence at 540 nm in buffer averaged over the six measurements.
(**D**) Binding of Alexa488-P2 to TG-loaded GUVs of varying surface tensions. Same as (**B**) except GUVs were aspirated in micropipettes to change their tension. Top left: schematic of the experimental protocol. Arrows represent aspiration pressure. Bottom left: representative images of a GUV aspirated to two different tensions. Scale bar, 5 μm (merge), 2 μm (inlay). Right: quantification of the fluorescence in the protein channel on the monolayer and bilayer parts of the GUV as a function of membrane tension. Each different marker corresponds to a different GUV (N=5). Quantification of fluorescence in the lipid channel is shown in Figure S3B.

We next established an assay system in which peptides could bind either bilayer or monolayer membranes. For this, we generated giant unilamellar vesicles (GUVs) and subsequently incorporated TG droplets into the GUV bilayers (Figure 2-3B**,** (Ben M'barek et al., 2017; Thiam et al., 2013a)). We then incubated the TG-loaded GUVs with fluorescently labeled peptides. Fluorescence imaging of the system revealed that P2 bound to TG-GUVs and was

enriched on the portion of the GUV consisting of a monolayer covering an embedded TG droplet (Figure 2-3B)**.** In contrast, P1 exhibited only very weak binding to the monolayer part (and did not bind to the bilayer part). P2 SH did not bind the monolayer nor the bilayer in these *in vitro* reconstitutions, indicating that large hydrophobic residues are necessary for amphipathic helix binding. Conversely, P1 LH bound in the same way as P2, further indicating that large hydrophobic residues are sufficient to mediate LD binding in the context of an amphipathic helix (Figure 2-3B; and see more images in Figure 2-9A).

Another prediction from our simulation models is that increases in phospholipid packing defects in bilayer membranes will increase protein binding to bilayers (Figure 2-2D)**.** To test this model experimentally, we modulated packing defects in liposomes and tested binding of synthesized peptides harboring environmentally sensitive fluorophores. For these experiments, we varied the liposome diameters to generate packing defects. Previous studies showed that the curvature of small liposomes (<200 nm diameter) leads to phospholipid packing defects due to a mismatch between the curvature of the vesicle and the curvature preferred by the membrane lipids (Bigay and Antonny, 2012). When testing binding of P2 to bilayer membranes, we found low-level binding to flat membranes, such as large diameter vesicles (200 nm radius; Figure 2-3C). However, smaller liposomes, with higher number of packing defects, bound fluorescently labeled P2 peptide more efficiently (Figure 2-3C). We also found that, in addition to P2, the P1 mutant with large hydrophobic residues bound preferentially to highly curved membranes, whereas P1 and the P2 mutant in which the large hydrophobic residues were replaced with smaller residues did not bind to membranes of any curvature (Figure 2-3C).

Finally, our model predicts that increasing the density of packing defects on the monolayer surface results in increased protein binding. To test this prediction, we incubated LD-loaded

GUVs with fluorescently-labeled P2, and aspirated these GUVs in a micropipette to increase their surface tension (Evans and Rawicz, 1990) and, as a result, the surface tension of the monolayer (Figure 2-3D). This increase in tension is expected to increase the area per phospholipid of the monolayer, i.e. to increase packing defect density. In these experiments, the peptide fluorescent signal on the monolayer increased with membrane tension (Figure 2-3D). Additionally, the fluorescent signal on the GUV membrane, although always lower than the signal on the monolayer, also increases with surface tension. This is consistent with our model, as stretching the GUV membrane also increases the density of bilayer packing defects. However, while the monolayer tensions in this experiment are close to the estimated tensions of cellular LDs (Ben M'barek et al., 2017), the bilayer tensions are orders of magnitudes above physiological tensions (Gauthier et al., 2012). As a consequence, the observed binding of the P2 peptide to the membrane bilayer is likely non-physiological. As a control, we measured the fluorescent signal of a lipid tracer on the monolayer and observed slightly decreased signal with increased membrane tension (Figure 2-9B).

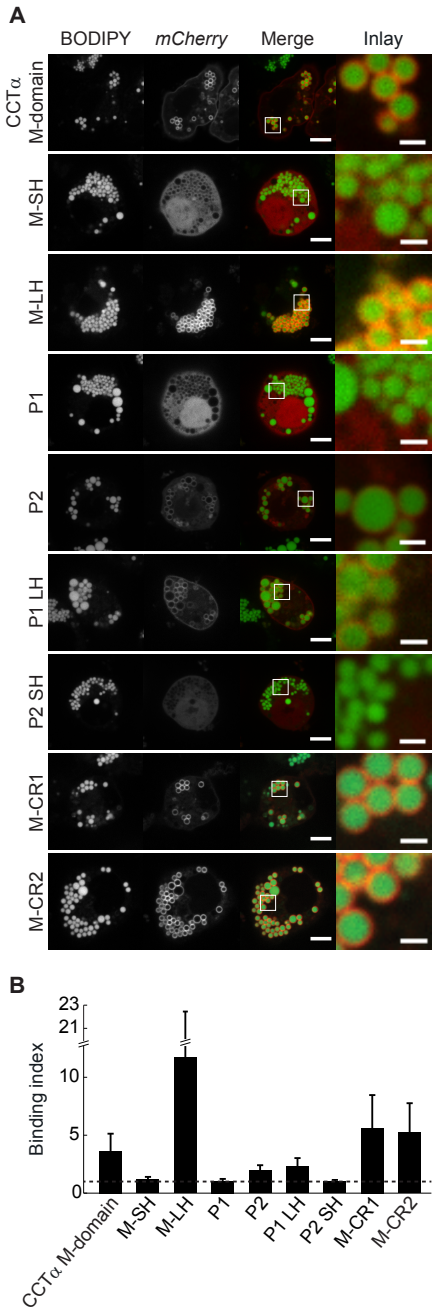

Figure 2-4 Large Hydrophobic Residues Are Crucial for LD Targeting of the M-domain in Cells

(**A**) Analysis of the LD-targeting ability of a series of M-domain mutants. *Drosophila* cells were transfected with mCherry-tagged constructs and incubated 14-18 hours with 0.5 mM oleic acid. LDs were stained with BODIPY. Representative images are shown. Scale bar, 5 μm (merge), 1 μm (inlay).

(**B**) Quantification of the protein signal on droplets. Data are represented as mean + SD. At least 10 cells were analyzed in each independent experiment.

2.3.5 Large Hydrophobic Residues Are Critical for Amphipathic Helix Binding to LDs in Cells

We next tested whether large hydrophobic residues are also crucial to detect and bind the phospholipid packing defects on the LD surface in cells. We expressed a series of variants of the human CCTα M-domain fused to mCherry in *Drosophila* S2 cells and assayed these proteins for LD binding. We first mutated eight of the large hydrophobic residues to valines in the context of the full-length M-domain ("M-SH", see Table 2-1). Consistent with our hypothesis, these mutations abolished LD binding (Figure 2-4A and Figure 2-4B). Conversely, increasing the number of large hydrophobic residues by mutating all six valines to larger hydrophobic residues (F, L or I, resulting in "M-LH", see Table 1) increased LD binding (Figure 2-4A and Figure 2-4B). Furthermore, and consistent with our simulation and *in vitro* data, the P1 fragment by itself did not bind LDs in *Drosophila* S2 cells, whereas P2 did bind LDs (Figure 2-4A and Figure 2-4B)**.** The binding of P2 depended on its large hydrophobic residues, as P2 SH did not bind LDs in cells (Figure 2-4A and Figure 2-4B)**.** In contrast, the P1 LH protein did bind LDs, indicating that large hydrophobic residues in the context of this amphipathic helix are sufficient to mediate LD binding in cells. To assess if electrostatic interactions play a role in LD binding, we also mutated charged residues of the CCTα M-domain ("M-Charge Reduction (CR) 1"**,** i.e. five positively and five negatively charged residues mutated to A and G and "M-Charge Reduction (CR) 2", i.e. 10 positively and 10 negatively charged residues mutated to A and G; see Table 2-1) and found no differences in LD binding (Figure 2-4A and Figure 2-4B).

#	Protein (Domain) *Organism*	Sequence	Binding Index		Ref.
			Mean	Std. Dev.	
1	CCTα (M-domain) *H. Sapiens*	HLQERVDKVKKKVKDVEEKSKEFVQKV... ...EEKSIDLIQKWEEKSREFIGSFLEMFG	2.6	1.5	(Krahmer et al., 2011)
2	CCTα (M-SH)	HLQERVDKVKKKVKDVEEKSKEVVQKV... ...EEKSVDLVQKVEEKSREVVGSVLEMVG	1.2	0.2	
3	CCTα (M-LH)	HLQERFDKLKKKFKDFEEKSKEFFQKI... ...EEKSIDLIQKWEEKSREFIGSFLEMFG	11.7	10.8	
4	CCTα (P1)	HLQERVDKVKKKVKDVEEKSKEFVQKV	1.0	0.1	
5	CCTα (P2)	VEEKSIDLIQKWEEKSREFIGSFLEMFG	1.9	0.5	
6	CCTα (P1 LH)	HLQERFDKLKKKFKDFEEKSKEFFQKI	2.3	0.7	
7	CCTα (P2 SH)	VEEKSVDLVQKVEEKSREVVGSVLEMVG	1.0	0.1	
8	CCTα (M-CR1)	HLQERVDAVKGAVKDVEAGSKEFVQKV... ...EAGSIDLIQKWGAKSRAFIGSFLEMFG	5.6	2.9	
9	CCTα (M-CR2)	HLQERVAGVGAAVGAVEGASGAFVQAV... ...AAGSIGLIQKWGGASREFIGSFLAMFG	5.2	2.6	
10	Lsd1 (H6-7) *D. Melanogaster*	MSKEAIHVLFYAAELIATDPKQAVQKA... ...KELWVYLS	3.7	1.4	(Arrese et al., 2008; Lin et al., 2014)

Table 2-1 Amphipathic Helices Studied in this Manuscript.

11	Lsd1 (H6-7 SH)	MSKEAVHVLVVAAELVATDPKQAVQKA... ...KELVVVLS	1.2	0.1	
12	ArfGAP1 (ALPS) *H. Sapiens*	FLNNAMSSLYSGWSSFTTGASRFAS	1.9	0.3	(Bigay et al., 2005)
13	ArfGAP1 (ALPS SH)	VLNNAMSSLVSGVSSVTTGASRVAS	1.0	0.1	
14	Core (D2) *HCV*	NLGKVIDTLTCGFADLMGYIPLVGAPL... ...GGAARALAHGVRVLEDGVNY	4.5	1.8	(Boulant et al., 2006)
15	GMAP 210 *H. Sapiens*	MSSWLGGLGSGLGQSLGQVGGSLASLT... ...GQISNFTKDML	3.2	1.0	(Drin et al., 2007)
16	Magainins (Magainin-2) *X. Laevis*	GIGKFLHSAKKFGKAFVGEIMNS	2.4	0.5	(Seelig, 2004)
17	Mastoparan X *V. Xanthoptera*	INWKGIAAMAKKLL	2.1	0.4	(Seelig, 2004)
18	Arf1 *H. Sapiens*	MGNIFANLFKGLFGKKE	1.8	0.4	(Kahn et al., 1992)
19	Sar1p *S. Cerevisiae*	MAGWDIFGWFRDVLASLGLWNKH	2.2	0.5	(Lee et al., 2005)
20	Kes1p *S. Cerevisiae*	SSSWTSFLKSIASFNGDLSSLSA	1.2	0.1	(Drin et al., 2007)
21	Nup133 *H. Sapiens*	LPQGQGMLSGIGRKVSSLFGILS	1.3	0.2	(Drin et al., 2007)
22	Epsin *H. Sapiens*	TSSLRRQMKNIVH	1.0	0.1	(Ford et al., 2002)

Table 2-1 Cont.

23	Endophilin A-I *N.Norvegicus*	MSVAGLKKQFHKATQKVSEKV	0.9	0.1	(Farsad et al., 2001)
24	Atlastin *D. Melanogaster*	FGGKLDDFATLLWEKFMRPIYHGCMEK	2.1	0.4	(Liu et al., 2012)
25	Yop1p *S. Cerevisiae*	ALPQTGGARMIYQKIVAPLTDRYILR	1.1	0.1	(Brady et al., 2015)
26	Curt1A *A. Thaliana*	SIDTNELITDLKEKWDGL	1.0	0.1	(Armbruster et al., 2013)
27	MinD *B. Subtilis*	VLEEQNKGMMAKIKSFFGVRS	1.6	0.2	(Szeto et al., 2003)
28	SpoVM *B. Subtilis*	MKFYTIKLPKFLGGIVRAMLGSFRKD	2.3	0.4	(Gill et al., 2015)
29	FtsA *E. Coli*	GSWIKRLNSWLRKEF	1.6	0.2	(Pichoff and Lutkenhaus, 2005)
30	Apolipoprotein A-I *H. Sapiens*	VLESFKVSFLSALEEYTKKLNTQ	1.4	0.1	(Mitsche and Small, 2013)
31	Apolipoprotein C-I *H. Sapiens*	ALDKLKEFGNTLEDKARELISRI	1.2	0.1	(Meyers et al., 2012)

Table 2-1 Cont.

To test whether large hydrophobic residues are a general feature of amphipathic helices that mediate LD binding, we mutated these residues in the amphipathic helices of the perilipin-like Lsd1 (Arrese et al., 2008; Lin et al., 2014) and in the ArfGAP1 ALPS motif. Similar to the findings with the CCTα M-domain, we found that the large hydrophobic residues were required for LD binding for both helices (Figure 2-5A and Figure 2-5B).

2.3.6 Promiscuous binding of amphipathic helices containing large hydrophobic residues to cellular lipid droplets

Amphipathic helices are common bilayer membrane-targeting motifs and are found in many proteins that do not normally target to LDs (Drin and Antonny, 2010). We tested whether our findings more broadly applied to such amphipathic helices by expressing a variety of amphipathic helices, derived from different proteins, in S2 cells and analyzing their binding to LDs (constructs 14 to 31 in Table 2-1). Most of these AHs (constructs 15 to 29) normally bind to bilayer membranes, HCV core (construct 14) binds to LDs (Boulant et al., 2006), and apolipoproteins A-I and C-I bind to lipoproteins (Segrest et al., 1992). Representative fluorescence images for these experiments are shown in Figure 2-5C. These constructs displayed a range of localization patterns, with some of them localizing to LDs to varying extents, whereas some (e.g., the AHs from Yop1 and endophilin) were not detectable at the LD surface (Figure 2-5C). We analyzed various features of the LD targeting sequences that were tested in cells to determine how they correlated with the amount of LD binding. These features included the amount of net charge, the hydrophobic moment (Eisenberg et al., 1982), and the number of large hydrophobic residues in a targeting domain. Among these variables, only the number of large hydrophobic residues correlated with LD binding in cells (Figure 2-5D). Specifically, amphipathic helices with more than 5 large hydrophobic residues bound LDs, with their binding index being proportional to the number of these residues, independent of the length of the targeting motif (Figure 2-5D).

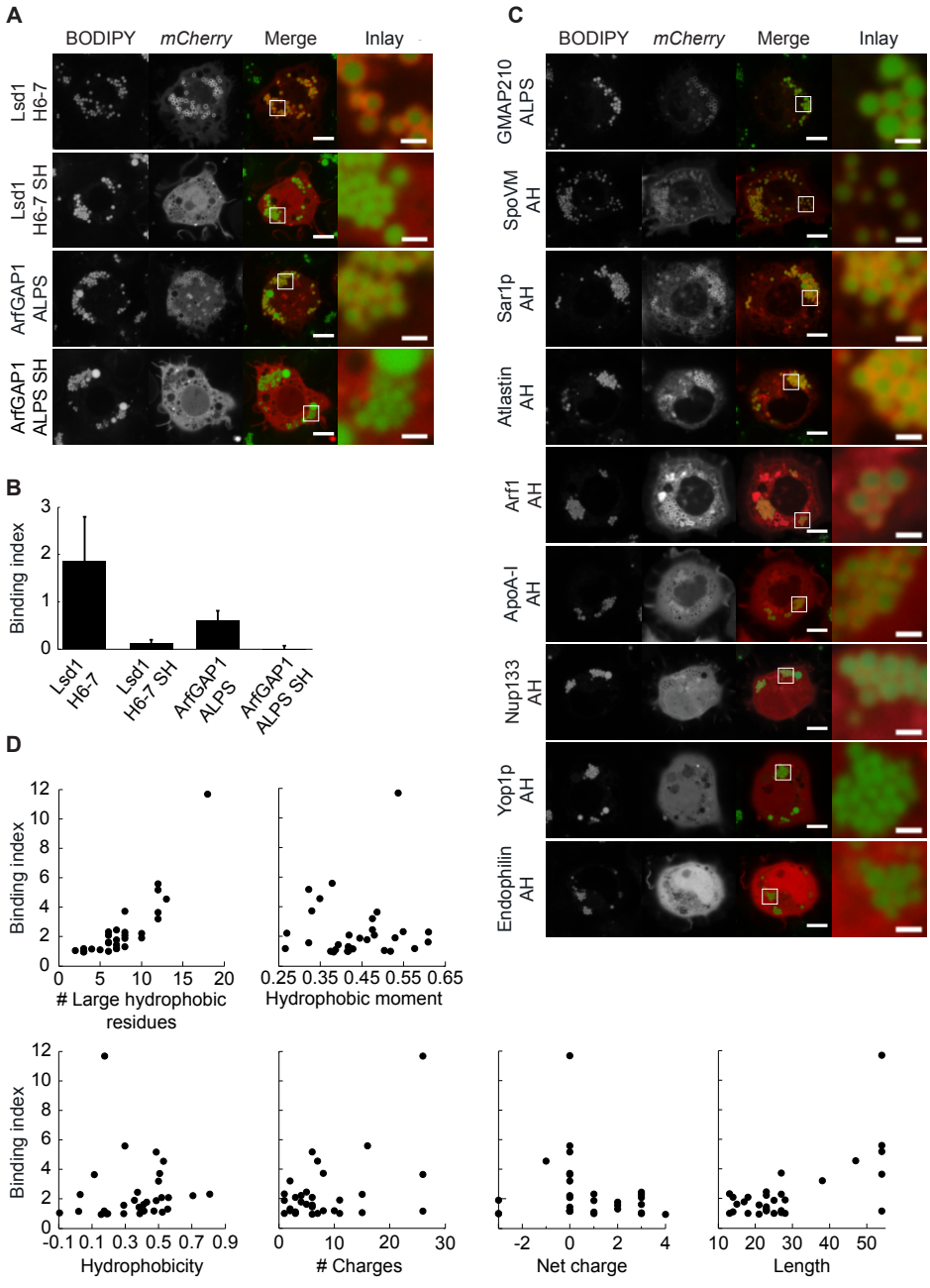

Figure 2-5 Binding of Amphipathic Helices to Cellular Lipid Droplets Correlates with the Number of Large Hydrophobic Residues.

(**A**) Analysis of the LD-targeting ability of WT and "small hydrophobic residues" (SH) mutants of ArfGAP1 ALPS and Lsd1 H6-7.

Figure 2-5 **Cont.**
(**B**) Quantification of the protein signal on droplets. Data are represented as mean + SD. Each construct was included in at least two independent experiments, and least 10 cells were analyzed in each experiment.
(**C**) Analysis of the LD-targeting ability of a range of amphipathic helices from non-LD proteins. More examples are shown in Figure 2-10. ApoA-I: Apolipoprotein A-I.
(**A**) and (**C**) *Drosophila* cells were transfected with mCherry-tagged constructs and incubated 14-18 hours with 0.5 mM oleic acid. LDs were stained with BODIPY. Representative images are shown. Scale bar, 5 μm (merge), 1 μm (inlay).
(**D**) Correlation between binding index and a range of amphipathic helix physicochemical properties. Each data point corresponds to a different construct. Data for the full set of amphipathic helices analyzed in this paper. The list of amphipathic helices and associated binding indices can be found in Table 2-1.

2.4 Discussion

We show here that the monolayer surfaces of LDs possess distinctive properties that enable the binding of cytosolic amphipathic helix-containing proteins. A combination of MD simulation and *in vitro* and cell-based experimental approaches consistently validate a model in which relatively large and frequent packing defects on the LD surface are recognized by large hydrophobic residues of AH-containing proteins to allow LD targeting and binding. Specifically, our simulations revealed that the underlying neutral lipids enable monolayer packing defects (defined as regions where the hydrocarbon groups of phospholipids or neutral lipids are accessible to the aqueous cytoplasm) to occur relatively frequently, thereby imparting distinctive surface properties to LDs. In particular, neutral lipids are seen to intercalate between the phospholipid side chains. The observation of such mixing between neutral lipids and phospholipid chains in the present and other MD simulations (Bacle et al., 2017) is consistent with prior studies by Hamilton and others that showed that neutral lipids solubilized into phospholipid liposomes are present in the membrane leaflets, aligning their acyl chains with those of the phospholipids (Hamilton and Small, 1981).

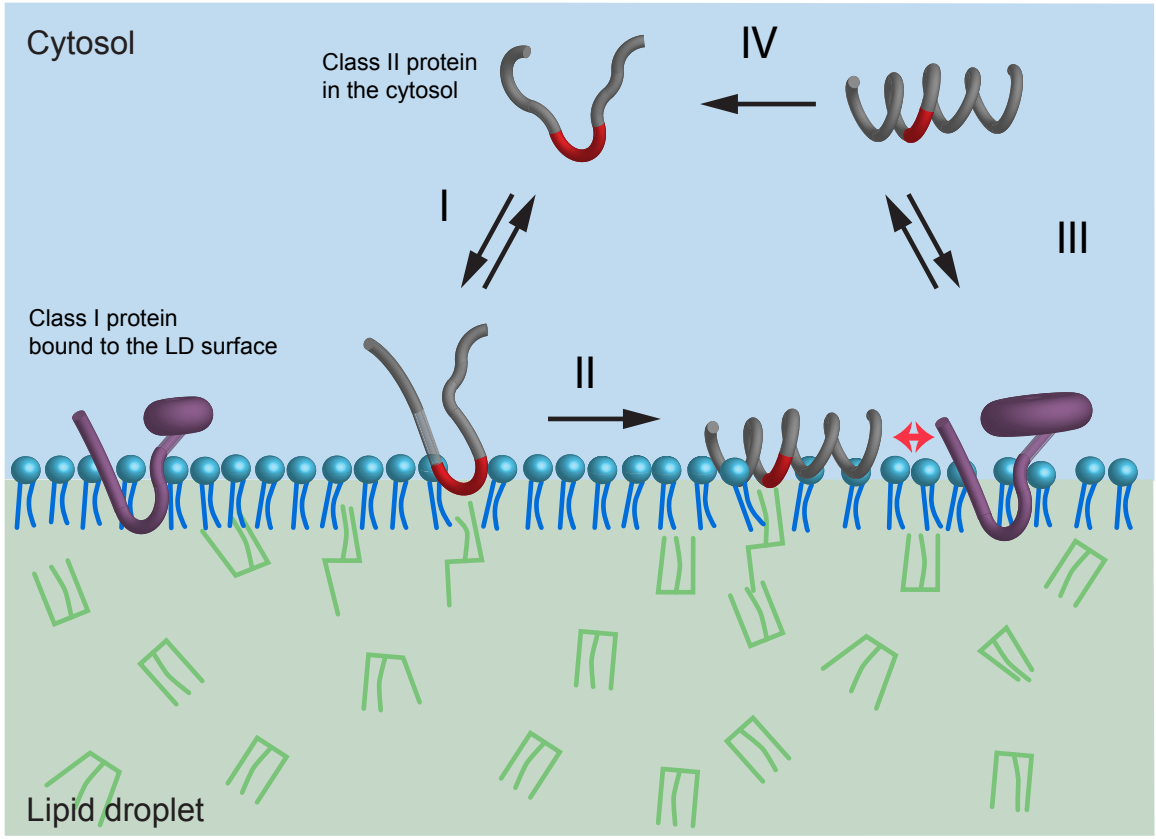

Figure 2-6 Proposed Thermodynamic Cycle for the Partitioning of Amphipathic Helices at the LD Surface
The amphipathic helix sequence is initially unfolded in the cytosol. Following insertion of a large hydrophobic residue into a packing defect at the lipid droplet surface (I), the amphipathic helix folds in the interfacial region that separates the bulk aqueous phase from the hydrocarbon core (II). High surface pressure at the crowded droplet surface promotes desorption of the folded helix (III), which subsequently unfolds in the cytosol (IV).

Our studies and prior work suggest a model for how class II (cytosolic) proteins interact with LDs (see Figure 2-6). In step **I**, an unfolded peptide sequence interacts with the LD surface and partitions to the interfacial region. For initial association, charges in the peptide are likely important, as our simulations indicate that the number of positively charged residues in a peptide somewhat correlates with the speed of association with the negatively charged membranes (Table 2-3). Consistent with this, supra-physiological concentrations of negatively charged

phospholipids (30% phosphatidic acid) promote binding of the P1 and P1 LH peptides which bear positive net charges (data not shown). However, this attraction is not enough to enable binding to LDs with physiologically relevant surface charges. Instead, the insertion of large, hydrophobic residues into large packing defects on the LD surface appears to be most critical. Consistent with this, we found that mutating the large hydrophobic residues to small ones abolished binding of the AH proteins in cells, whereas charge reductions had no significant effect. This step of protein binding to the LD surface is fast, and hence was detectable on the timescale of our MD simulations. It is also likely reversible, as we found cases in which the peptide initially adsorbed, but subsequently fell off the LD surface (Figure 2-8). Evidence suggests that large hydrophobic residues are also relevant for LD binding for class II proteins that do not possess AH sequences. For example, the binding of CGI-58 to LDs requires tryptophan residues, although not in the context of an AH (Boeszoermenyi et al., 2015). This mechanism (association of hydrophobic residues in AHs with phospholipid packing defects) is similar to the previously described mechanism of AH binding to highly-curved membranes (Cui et al., 2011; Vanni et al., 2013), as discussed below.

In step **II** of the binding reaction, the amphipathic helix folds in the interfacial region between the hydrophobic LD and the aqueous cytoplasm. The main driving force for this step is likely the need to satisfy the hydrogen bonding requirements of the peptide backbone. Folding into an α-helix lowers the free energy of peptide bond partitioning to the hydrophobic phase due to the intramolecular hydrogen bonds (Fernandez-Vidal et al., 2007; Ladokhin and White, 1999). This step is much slower than step **I**, and we did not observe complete folding in the microsecond timescale of our MD simulations. However, in one instance, we observed the beginning of the folding reaction, and this example suggests that folding starts with the inserted

residues and spreads from there to form the full AH (data not shown). This slow step provides a large amount of free energy (Almeida et al., 2012; Cui et al., 2011; Fernandez-Vidal et al., 2007; Ladokhin and White, 1999) and essentially renders the pathway for binding irreversible in biological systems. Consistent with this notion, we previously observed in FRAP experiments that AH-bound proteins, such as CCT1, have a long half-life on the LD surface (Krahmer et al., 2011). Thus, displacing proteins from the LD surface (step **III** of the interaction cycle) does not follow a simple reversal of the binding reaction, but instead is due to "bumping-off" when proteins collide in conditions where the LD surface is more crowded (Kory et al., 2015). As described in (Kory et al., 2016), proteins fall off the LD surface if the energy of the collision is greater than the binding energy of the folded AH to the LD surface (Kory et al., 2015). Therefore weaker binders are more easily displaced from the LD surface. Once the protein falls off the LD surface, the peptide unfolds, as the entropic preference for the unfolded configuration dominates. The enthalpic driving force to fold through forming 1-4 peptide backbone hydrogen bonds is significantly decreased, as water can also satisfy these backbone hydrogen-bonding sites (Adrover et al., 2012; Bianco and Franzese, 2015; Camilloni et al., 2016).

Consistent with the notion that AHs bind LDs and highly-curved membranes in a similar fashion, we found that sequences from proteins with various cellular localization, such as GMAP210 that is localized primarily to the Golgi (Doucet et al., 2015), are sufficient to mediate binding to LDs in cells. While this finding is surprising, it shows that there is no strict targeting specificity for LDs encoded in the amphipathic helix by itself. Instead, the LD surface is promiscuous for binding proteins with amphipathic helices, provided that they contain large hydrophobic residues. Such residues are commonly found in most amphipathic helices, including the ones of CCTα , GMAP210 and ArfGAP1. This raises an interesting question: how are some

amphipathic helix-containing proteins, such as GMAP210, excluded from LDs in a normal cellular context? The answer to this is currently unknown, but it likely involves combining amphipathic helices with specificity determinants, such as other membrane binding domains or protein-protein interaction motifs. Examples of this include CCTα, which has a nuclear localization domain in addition to a LD-binding amphipathic helix and which in the absence of LDs localizes to the nucleus in *Drosophila* cells, arguing both signals compete with each other in determining the localization of the protein (Krahmer et al., 2011; Lagace and Ridgway, 2005). Also consistent with this hypothesis, GMAP210 is a long coiled-coil protein, which contains several domains that can interact with membranes or proteins, and that influence its localization in cells (Drin et al., 2008; Sinka et al., 2008). Removing these additional specificity determinants in our experiments revealed the promiscuity of LD binding by AHs. In addition to these mechanisms directing proteins away from LDs, binding strength and thus resistance to molecular crowding likely play a role in determining subcellular localization (Kory et al., 2015). Many instances of genuine LD proteins, such as perilipin proteins, rely on a string of amphipathic helices. Addition of multiple amphipathic helices leads to higher avidity, stronger binding, and thus a higher resistance to molecular crowding (Kory et al., 2015). Also consistent with this, CCTα's M-domain is an unusually long amphipathic helix (54 amino acids).

Our findings on the promiscuity of amphipathic helices in binding the LD surface may have implications for physiology and disease. For example, human mutations of the ER protein *seipin*/BSCL2, involved in LD formation, apparently alters properties of the LD surface, leading to abnormal, enhanced recruitment of AH-containing proteins (Grippa et al., 2015). This suggests that seipin deficiency promotes increased packing defects on LD surfaces. Moreover, in pathological conditions where LDs over-accumulate, for instance during obesity-related hepatic

steatosis or during the development of foam cells in atherosclerotic plaques, a large amount of LD surfaces with packing defects may effectively compete for amphipathic helix containing proteins normally not binding LDs, thus possibly contributing to cellular dysfunction (e.g., via mistargeting of proteins). Therefore, a better understanding of the mechanisms for protein targeting to LD surfaces is predicted to lead to an enhanced molecular understanding of disease pathogenesis.

2.5 Acknowledgements

We thank Guan-Yue Chen, Jeremy Furtado and Maria-Jesus Olarte for help with experiments, Mijo Simunovic and Patricia Bassereau for providing micropipettes, members of the Farese & Walther and Voth laboratories for comments on the manuscript, and Gary Howard for editorial assistance. This work was supported by 2R01GM097194 (to T.C.W.) the Mathers foundation (to T.C.W). T.C.W is an investigator of the Howard Hughes Medical Institute. Anton computer time was provided by the Pittsburgh Supercomputing Center (PSC) through grant *R01GM116961* from the National Institutes of Health. The Anton machine at PSC was generously made available by D.E. Shaw Research. The MD simulation in this research were also performed in part on the Comet supercomputer at the San Diego Supercomputer Center (SDSC) with resources provided by the Extreme Science and Engineering Discovery Environment (XSEDE), which is supported by National Science Foundation grant number ACI-1548562. The MD simulations were also completed in part with resources provided by the University of Chicago Research Computing Center.

2.6 Method Details

2.6.1 Cell Lines and Cell Culture

The *Drosophila* cells used in this study are from the S2R+ cell line (sex: male) and were provided by Prof. Norbert Perrimon (Harvard Medical School). Cells were cultured at 26°C in Schneider's Drosophila Medium (LifeTechnologies) containing 10% fetal bovine serum, 50 units/ml penicillin and 50 mg/ml streptomycin.

2.6.2 Molecular Dynamics Simulations

General simulation parameters

All molecular dynamics (MD) simulations were performed using the CHARMM36 force field (Best et al., 2012; Klauda et al., 2010; MacKerell et al., 1998). Simulations were performed using the GROMACS (Abraham et al., 2015) MD simulation engine unless otherwise noted. Simulations were integrated with a 2 fs timestep. Van der Waals (VDW) interactions were switched to zero between 1.0 and 1.2 nm, and the Particle Mesh Ewald (Essmann et al., 1995) was used to evaluate electrostatic interactions. All bonds to hydrogen were constrained using the LINCS algorithm (Hess, 2008). The Nose-Hoover thermostat (Hoover, 1985) was used to maintain temperature at 310 K with a coupling time constant of 1.0 ps. For simulations with constant pressure, the Parrinello-Rahman barostat (Parrinello and Rahman, 1981) was used to maintain a pressure of 1.0 bar with a compressibility of 4.5×10^{-5} and a coupling time constant of 5.0 ps. The pressure was maintained semi-isotropically in all membrane simulations, while isotropic pressure coupling was used in protein only simulations. A list of simulations performed is provided in Table S1. The cumulative length of all the simulations was 41.1 μs.

Building of bilayer and lipid droplet membranes

Bilayer systems were built using the CHARMM-GUI membrane builder (Jo et al., 2008; Wu et al., 2014) with the CHARMM36 lipid force field (Klauda et al., 2010). Bilayers of composition 65:27:8 POPC:DOPE:SAPI and 85:15 DOPC:DOG were built of size 11x11 nm^2 and solvated with a 2.2-nm layer of TIP3P water on both sides of the membrane as well as a salt concentration of 150 mM NaCl. The system was relaxed and equilibrated using the equilibration procedure (Wu et al., 2014), designed by the CHARMM-GUI using the GROMACS simulation engine. Briefly, harmonic positional restraints were placed on select lipid atoms, and harmonic dihedral restraints were placed to maintain the *cis* orientation of double bonds in the lipid tails. These restraints were slowly relaxed through multiple steps of equilibration. For lipid droplet simulations, the neutral lipid core was constructed from a box 1:1 cholesteryl oleate:triolein. The neutral lipid box was built using Packmol (Martinez et al., 2009) to match the x-y dimensions of the POPC:DOPE:SAPI bilayer, with different z values (4, 6, and 8 nm). The neutral lipids were equilibrated using the same equilibration procedure described above. The neutral lipid box was then inserted between the two leaflets of the bilayer, after which another round of equilibration was performed.

Determining peptide structure

Each peptide structure (ALPS, P1, P2, M-domain) was first generated as an idealized alpha-helix using Molefacture in VMD (Humphrey et al., 1996). Each peptide was solvated using GROMACS in a water box with at least 1 nm of padding on each side of the peptide. The GROMACS *genion* tool was used to add ions to the system such that the system was neutralized and had a concentration of 150 mM NaCl. The system was then minimized using steepest-descent until the maximum force was less than 1000.0 kJ/mol/nm. A total of 100 ps of

equilibration was then performed in the constant NVT ensemble. The system was then heated up to 500 K, after which 10 ns of simulation was performed to unfold the protein. The system was then simulated at 310 K in the constant NPT ensemble for 5 ns.

Building peptide-membrane simulations

Using VMD, the TIP3P molecules and salt ions were removed from the membrane simulation box. To build each of the peptide-membrane systems, a random structure from the final peptide equilibration run was chosen. A different random structure was chosen for each of the four replicas of each peptide-membrane simulation. The randomly chosen peptide conformation was then placed at least 2 nm away from the membrane. The system was then solvated in VMD with TIP3P water and 150 mM NaCl. The system was then equilibrated using the CHARMM-GUI procedure described above. The systems were then simulated for 750–1000 ns for production runs.

Production Simulations in ANTON

Simulations were also run on the ANTON (Shaw et al., 2009) supercomputer, which is highly specialized for long time MD simulations. Simulations were integrated with a 2-fs timestep using RESPA (Tuckerman et al., 1992), where long range electrostatic interactions were evaluated every three timesteps. VDW interactions were switched to zero between 1.0 and 1.2 nm, and Particle Mesh Ewald (Essmann et al., 1995) was used to evaluate electrostatic interactions. All bonds to hydrogen were constrained using the SHAKE algorithm (Ryckaert et al., 1977). The Nose-Hoover thermostat (Hoover, 1985) was used to maintain temperature at 310 K with a coupling time constant of 1.0 ps. The MTK barostat (Martyna et al., 1994) maintained a pressure of 1.0 atm semi-isotropically in all membrane simulations.

Lipid packing defects

Packing defects were calculated using a described procedure (Cui et al., 2011). In brief, the solvent accessible surface area of the hydrophobic tails was calculated using VMD (Humphrey et al., 1996) using a probe radius of 0.3 nm. The points composing this surface are projected onto the membrane plane. The surface is divided into bins of size 0.16 nm^2, and each of these points are placed into the bins. The binned points are considered to be part of the same defect cluster if they are within 0.25 nm of each other. Defect lifetimes were calculated as follows. A defect was considered to have lived from one frame to the next if any of the bins composing the defect were the same in frame *i* and frame *i+1*. If a defect split into two or more defects, each smaller defect was followed in time, and the longest lifetime of the split defects was considered to be contributing to the lifetime of the original large defect. A histogram of defect sizes was tabulated for defects with lifetimes longer than 5 ns. This histogram was then fit to an exponential decay $p(x) = ce^{-ax}$ where *x* is the defect size, *p(x)* is the probability of finding a defect of size *x* with a lifetime greater than 5 ns, *c* is a constant, and *a* is the decay rate in units of nm^{-2}.

2.6.3 Peptides Design

Peptides were synthesized by Bio-Synthesis Inc. An N-terminal GG linker was included in the sequence of all peptides and peptides were conjugated with fluorescent dyes at their N-terminus. Conjugation with NBD-Chloride was performed by Bio-Synthesis. Peptides conjugated with Alexa Fluor 488 C5 Maleimide (Alexa488) had an extra C at their N-terminus. The reaction was performed according to the manufacturer's instructions. Unreacted peptide and dye were removed by reverse phase chromatography.

2.6.4 Plasmids Construction and Transfection

Synthetic gene fragments were purchased from Integrated DNA technologies and cloned into either the pENTR™/SD/D-TOPO or pENTR™/D-TOPO vector. The entry clone was subcloned into the pACherryW (all constructs except for the Flag sequence) or pAWCherry (Flag sequence) vector (Guo et al., 2008).

Transfections were performed with Effectene Transfection Reagent (Qiagen) according to the manufacturer's instructions. Transfections were done 24–36 hr before the experiment. Only the AH fragment was expressed except in the case of ArfGAP1, where the construct comprised amino acids 137-237 of human ArfGAP1 (isoform 1). Constructs 18 to 31 (see Table 1) had N-terminal G-S linkers to bring them to the same size (27 amino acids).

2.6.5 LDs induction

Cells were incubated 14-18 hr with 0.5 mM oleic acid (complexed to bovine serum albumin at a 3:1 molar ratio).

2.6.6 Microscopy

Live cell imaging was performed as described using high numerical aperture 60x or 100x objectives (Wang et al., 2016). For *in vitro* experiments, imaging was performed with a spinning disk confocal (Yokogawa CSU22) set up on a Nikon Eclipse Ti inverted microscope. Illumination was performed with 488 and 561 nm laser lines, and detection with an imagEM EM-CCD camera (Hamamatsu). **TG-loaded GUVs:** imaging was performed with a 60X ApoTIRF 1.49 NA objective (Nikon). **Artificial LDs:** LDs float at the top of the observation chamber and were imaged using a lower magnification/ longer working distance objective (Plan Apo VC 20X, 0.75 NA, Nikon).

2.6.7 In Vitro Assays

For all *in vitro* experiments we used a phospholipid composition mimicking the composition of the mammalian LD monolayer (1-palmitoyl-2-oleoyl-sn-glycero-3-phosphocholine (POPC): 1,2-dioleoyl-sn-glycero-3-phosphoethanolamine (DOPE): L-α-phosphatidylinositol from liver, bovine (liver PI) 65: 27: 8 (Bartz et al., 2007)). In experiments with GUVs, 0.05-0.1 mol % 1,2-dioleoyl-sn-glycero-3-phosphoethanolamine-N-(lissamine rhodamine B sulfonyl) (Rhodamine PE) was included in the lipid composition. All experiments were performed at room temperature.

Artificial LDs

Phospholipids in chloroform were added to triolein at a 0.5% molar ratio. The solvent was evaporated under a stream of nitrogen and further by placing the vial in a desiccator for 3–4 h. This phospholipids and oil mixture was added to buffer (20 mM Tris pH 7.5, 100 mM NaCl) at a 0.2% ratio (vol/vol), and the solution was vortexed for a few seconds and sonicated for about a minute in a bath sonicator. This emulsion was incubated with 1 μM Alexa488-labeled peptide for 5 min. before imaging by confocal microscopy.

Liposomes

Phospholipids in chloroform were dried under a stream of nitrogen and the vial was placed in a desiccator for about half an hour to remove traces of solvent. The lipid film was rehydrated in buffer (20 mM Tris pH 7.5, 100 mM NaCl) for 1 h (final lipid concentration: 2.5 mM), and the sample was processed through five cycles of freezing and thawing and subsequently extruded 11 times through polycarbonate filters with pore diameters of either 30, 50, 100 or 200 nm (Avanti Polar Lipids). The resulting liposome solutions were incubated with 1 μM NBD-labeled peptide for 5 min, and fluorescence emission spectra were recorded on an Infinite M200 microplate

reader (TECAN), with the following settings: excitation wavelength: 490 nm and bandwidth: 10 nm, emission range: 520–650 nm, bandwidth: 20 nm and step size: 5 nm.

TG-loaded GUVs

Phospholipids in chloroform were spread on indium tin oxide–coated glass slides. GUVs were grown by electroformation (Angelova et al., 1992) in 600 mM sucrose using a Vesicle Prep Pro (Nanion) with the following settings: frequency 10 Hz, amplitude 1.4V, temperature 23°C, for 1 h. GUVs were incubated with an oil-in-water emulsion (5% (vol/vol) triolein in buffer (20 mM Tris pH 7.5, 100 mM NaCl, 400 mM glucose), prepared as described above) for 10 min. The mixture was allowed to settle for about 2 h to separate most of the oil droplets from the GUVs. The TG-loaded GUVs were collected at the bottom of the tube and incubated with 1 μM Alexa488-labeled peptide for 5 min. before imaging by confocal microscopy.

Micropipette experiments

TG-loaded GUVs were prepared as described above and incubated with 1 μM Alexa488-labeled P2 for 5 min. Micropipette aspiration was performed following the protocol described in (Prévost et al., 2017). The GUV tension σ was calculated using the following expression (Kwok and Evans, 1981): $\sigma = \Delta P\, R_{\mathrm{pip}}/2\left(1 - R_{\mathrm{pip}}/R_{\mathrm{GUV}}\right)$, where ΔP is the aspiration pressure, R_{pip} is the radius of the pipette opening and R_{GUV} is the radius of the GUV.

2.6.8 Quantification and Statistical Analysis

The statistical details of the experiments can be found in the figure legends.

Artificial LDs

Images were quantified using CellProfiler software (Carpenter et al., 2006). For each droplet, the integrated intensity (background-subtracted) over the droplet-occupied region in the Alexa488 channel was normalized by the surface area of the droplet.

TG-loaded GUVs

Images were quantified using custom Matlab (MathWorks) software. The mean intensity (background-subtracted) in the protein and lipid channels along a portion of the contour of the monolayer and bilayer part of the GUVs were quantified.

Cell experiments

Images were quantified using FIJI software (Schindelin et al., 2012). An automatic threshold was applied to the BODIPY channel to identify the LD-occupied region. The mean intensity of the mCherry signal in that region was measured. This value was divided by the mean intensity of the signal in a distinct region of the cytoplasm to account for differences in expression levels. Finally, for each construct the average of this ratio was divided by the equivalent average for Flag-mCherry, considered a baseline value. The final quantity is referred to as "binding index" in Figures 4 and 5.

2.7 Supplementary Information

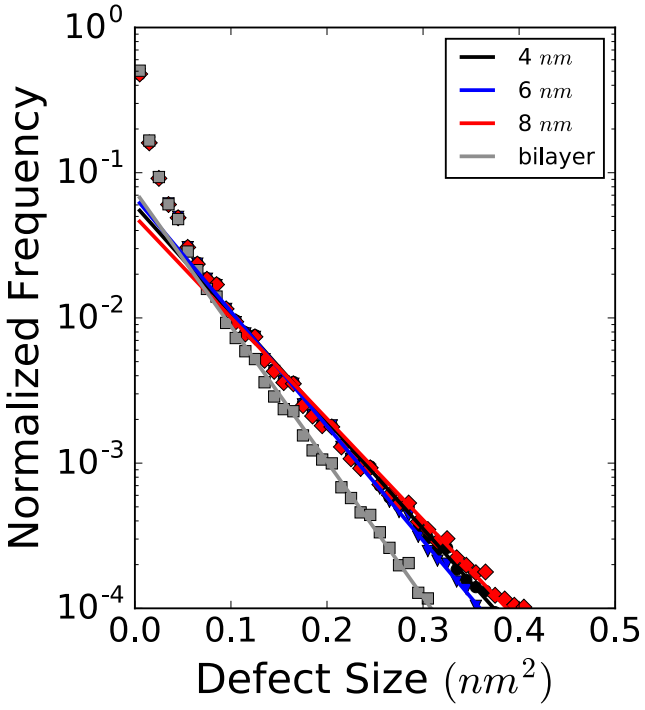

Figure 2-7 Histogram of packing defect sizes for bilayer and monolayer surfaces with varying TG thicknesses.
The monolayer with TG thickness of 4 nm exhibits an increase in the frequency of larger defects compared with the bilayer. Further increase in TG thickness shows no further increase in frequency of large defects. Normalized frequency: number of defects for a given size range is normalized by the total number of defects over the simulation time frame. Solid lines are least-square fits to exponential decays**.**

A

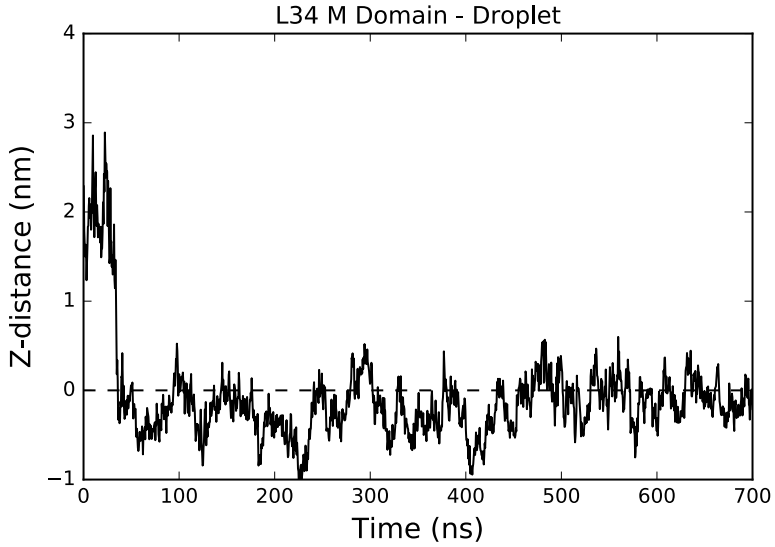

B

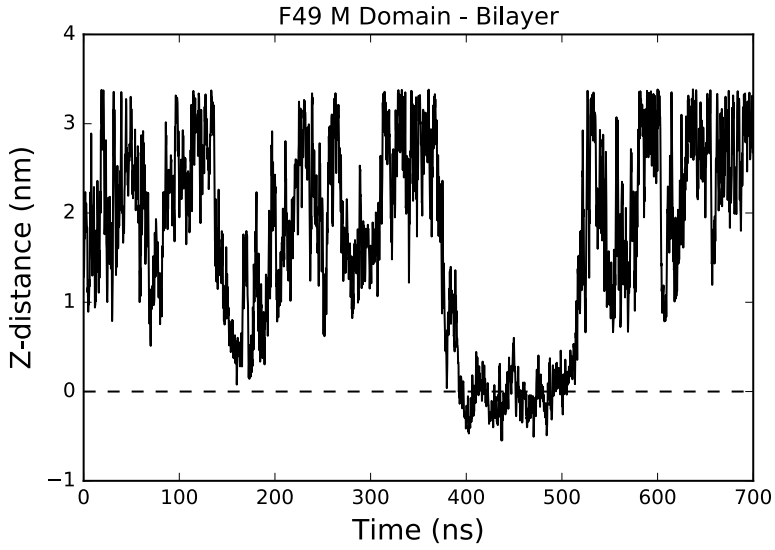

Figure 2-8 Representative Z-distances between the carbon-alpha of a specific residue and the membrane phosphate plane.

A) Residue L34 of the M-domain inserts below the monolayer phosphate plane within the first 50 ns, and remains bound to the membrane throughout the length of the simulation. **B)** Residue F49 of the M-domain inserts below the bilayer phosphate plane 400 ns into the simulation, and dissociates from the membrane 100 ns after binding. F49 was not counted as having stably inserted into the membrane in this simulation.

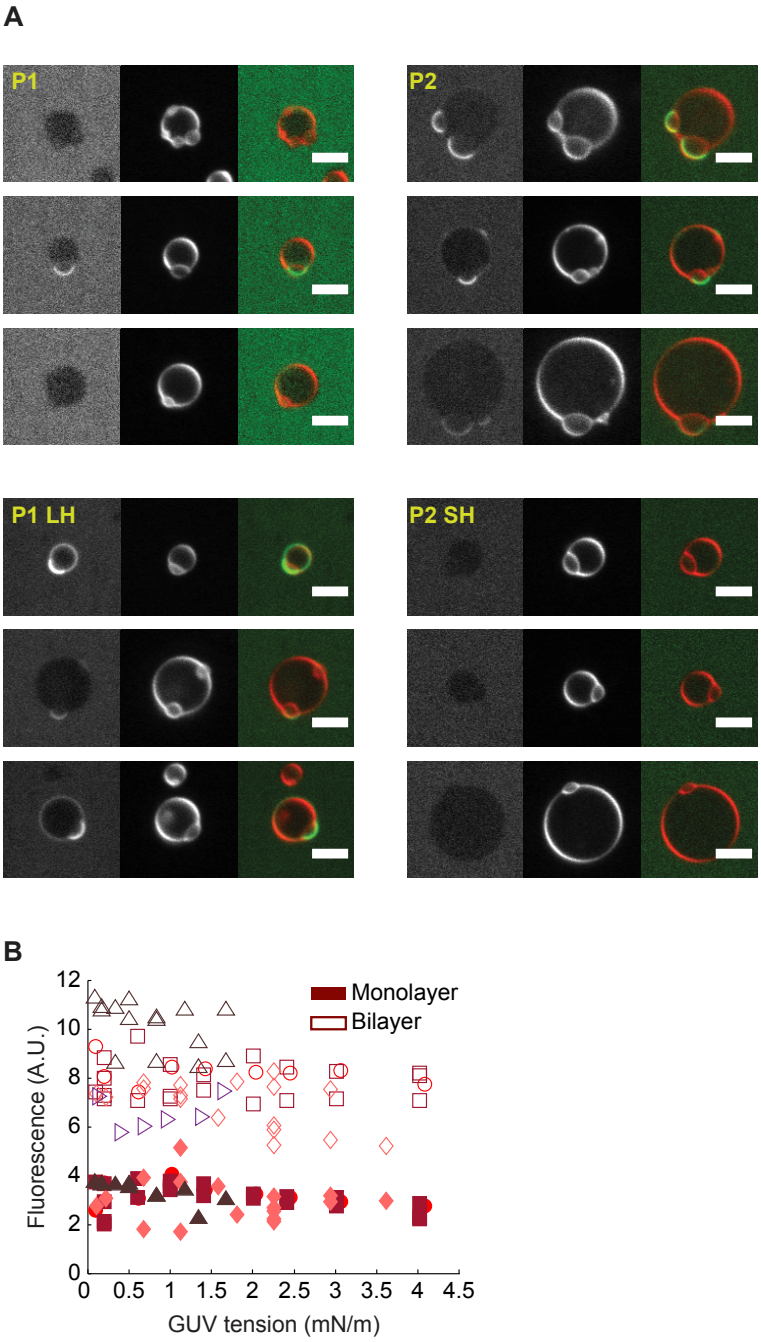

Figure 2-9 Amphipathic Helix binding to GUVs
(**A**) Gallery of TG-GUVs incubated with fluorescent peptides as in Figure 3B. Scale bar, 5 µm. (**B**) Fluorescence in the lipid channel on the monolayer and bilayer parts of the same GUVs as in Figure 3D, as a function of membrane tension. Each different marker corresponds to a different GUV (N=5).

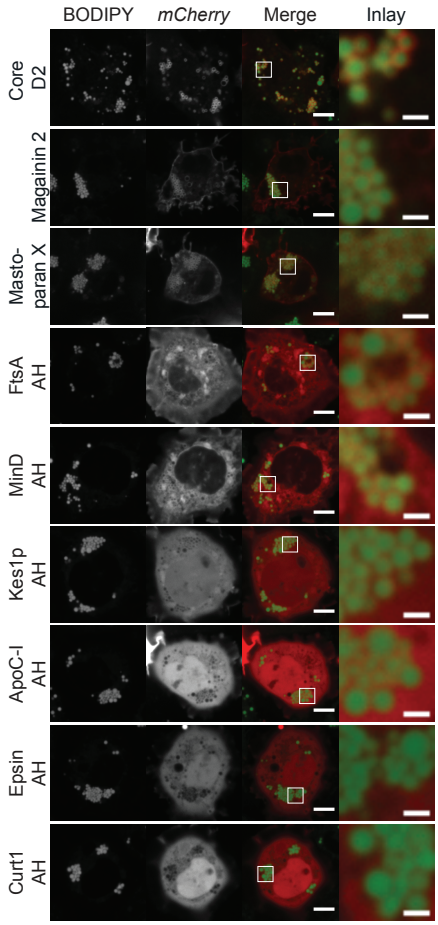

Figure 2-10 Analysis of the LD-targeting ability of a range of AH domains from LD- (Core), lipoprotein- (ApoC-I) and bilayer membrane-targeting proteins.
ApoC-I: Apolipoprotein C-I.Drosophila cells were transfected with mCherry-tagged constructs and incubated 14-18 hours with 0.5 mM oleic acid. LDs were stained with BODIPY. Representative images are shown. Scale bar, 5 μm (merge), 1 μm (inlay).

Membrane Composition	Membrane Type	Protein	#	MD Engine	Simulation Time (ns)
DOPC:DOG	Bilayer	NA		GROMACS	100
POPC:DOPE:SAPI	Bilayer	NA		ANTON	1000
POPC:DOPE:SAPI	Lipid Droplet (4 nm)	NA		ANTON	500
POPC:DOPE:SAPI	Lipid Droplet (6 nm)	NA		GROMACS	500
POPC:DOPE:SAPI	Lipid Droplet (8 nm)	NA		GROMACS	500

Table 2-2 Summary of MD Simulations

Membrane Composition	Membrane Type	Protein	#	MD Engine	Simulation Time (ns)
POPC:DOPE:SAPI	Lipid Droplet (4 nm)	ALPS	1	GROMACS	750
POPC:DOPE:SAPI	Lipid Droplet (4 nm)	ALPS	2	GROMACS	750
POPC:DOPE:SAPI	Lipid Droplet (4 nm)	ALPS	3	GROMACS	750
POPC:DOPE:SAPI	Lipid Droplet (4 nm)	ALPS	4	GROMACS	750
POPC:DOPE:SAPI	Bilayer	ALPS	1	GROMACS	1000
POPC:DOPE:SAPI	Bilayer	ALPS	2	GROMACS	1000
POPC:DOPE:SAPI	Bilayer	ALPS	3	GROMACS	750
POPC:DOPE:SAPI	Bilayer	ALPS	4	GROMACS	750
POPC:DOPE:SAPI	Lipid Droplet (4 nm)	P1	1	GROMACS	750
POPC:DOPE:SAPI	Lipid Droplet (4 nm)	P1	2	GROMACS	750
POPC:DOPE:SAPI	Lipid Droplet (4 nm)	P1	3	GROMACS	750
POPC:DOPE:SAPI	Lipid Droplet (4 nm)	P1	4	GROMACS	750
POPC:DOPE:SAPI	Bilayer	P1	1	GROMACS	750
POPC:DOPE:SAPI	Bilayer	P1	2	GROMACS	750
POPC:DOPE:SAPI	Bilayer	P1	3	GROMACS	750
POPC:DOPE:SAPI	Bilayer	P1	4	GROMACS	750
POPC:DOPE:SAPI	Lipid Droplet (4 nm)	P2	1	ANTON	750
POPC:DOPE:SAPI	Lipid Droplet (4 nm)	P2	2	ANTON	750
POPC:DOPE:SAPI	Lipid Droplet (4 nm)	P2	3	GROMACS	750
POPC:DOPE:SAPI	Lipid Droplet (4 nm)	P2	4	GROMACS	750
POPC:DOPE:SAPI	Bilayer	P2	1	ANTON	2000
POPC:DOPE:SAPI	Bilayer	P2	2	ANTON	2000
POPC:DOPE:SAPI	Bilayer	P2	3	GROMACS	750
POPC:DOPE:SAPI	Bilayer	P2	4	GROMACS	750
DOPC:DOG	Bilayer	P2	1	GROMACS	1000
DOPC:DOG	Bilayer	P2	2	GROMACS	1000
DOPC:DOG	Bilayer	P2	3	GROMACS	1000
DOPC:DOG	Bilayer	P2	4	GROMACS	1000
POPC:DOPE:SAPI	Lipid Droplet (4 nm)	M	1	ANTON	1000
POPC:DOPE:SAPI	Lipid Droplet (4 nm)	M	2	ANTON	1000
POPC:DOPE:SAPI	Lipid Droplet (4 nm)	M	3	GROMACS	750
POPC:DOPE:SAPI	Lipid Droplet (4 nm)	M	4	GROMACS	750
POPC:DOPE:SAPI	Bilayer	M	1	ANTON	750
POPC:DOPE:SAPI	Bilayer	M	2	ANTON	750
POPC:DOPE:SAPI	Bilayer	M	3	GROMACS	750
POPC:DOPE:SAPI	Bilayer	M	4	GROMACS	750

Table 2-2 Cont.

Binding time (ns)

		Bilayer				Monolayer				Avg. on
	Charge	1	2	3	4	1	2	3	4	Monolayer
M	0		25			700	25		50	260
P2	-3				250	500	500	600	250	460
ALPS	1	100	25	100	100	100	25	25	25	45

Table 2-3 Summary of simulation binding times (ns) for M-domain, P2, and ALPS peptides on monolayer and bilayer membranes.

ALPS, which is positively charged, binds significantly faster to the negatively charged monolayer in comparison with P2, which is negatively charged.

Chapter 3. Distribution of Amino Acids in Bilayer and Lipid Droplet-Like Membranes

3.1 Introduction

Proper protein targeting to lipid droplet (LD) membranes is important for proper function of a number of cellular processes and has consequences for a number of diseases, including type II diabetes/obesity, lipodystrophy, and atherosclerosis (Krahmer et al., 2013a; Rohl et al., 2004; Welte, 2015). Understanding how proteins differentiate lipid droplets from the ER and other bilayer-containing organelles is key to understanding the targeting mechanism of proteins to lipid droplets.

Studies suggest that proteins target to lipid droplets from two areas of the cell. Class I proteins, which contain membrane-embedded hairpin motifs, relocalize from the ER to LDs during LD budding or through ER-LD bridges. Class II proteins, which contain amphipathic helices, are translated in the cytosol and contain amphipathic helices, which bind to lipid droplets. Recent studies (Čopič et al., 2018; Prevost et al., 2018) have shown that large hydrophobic residues as well as overall hydrophobicity of amphipathic helices play a key role in binding to LDs.

Previous studies have examined the free energies of insertion for amino acid side chains in a number of bilayer (MacCallum et al., 2008) and bilayer-like (Pogorelov et al., 2014) systems using all-atom, united-atom and coarse-grained force fields. However, lipid droplet membranes have been shown to exhibit a number of different properties compared to bilayer membranes, including area per lipid, phospholipid length, and lipid packing defects (Bacle et al., 2017; Prevost et al., 2018). Additionally, experiments and simulations have shown that amphipathic helices with many hydrophobic residues more easily insert into LD membranes compared to

bilayer membranes. Specifically, AHs containing large hydrophobic residues were observed to preferentially bind to LDs. Proteins with membrane-embedded domains have also been shown to target to LDs from the ER through ER-LD bridges. Understanding the free energy differences between amino acids in bilayer and LD membranes is essential to understanding these LD-targeting proteins.

Using transition-tempered metadynamics (Dama et al., 2014b), we calculate the partitioning free energies of single residue amino acids into bilayer and LD-like monolayer membranes with the same phospholipid composition. Transition-tempered metadynamics has been shown to converge quickly and accurately to the correct potential of mean force (PMF), especially for small molecule permeation through membranes. Unlike other studies, which have either calculated PMFs for small-molecule side-chain analogues of the amino acids or the 5-residue Whimley-White peptides, we calculated single residue PMFs with methylated and amidated N- and C-terminal caps. Since LD proteins can have varying numbers of amino acids within the membrane and are not limited to a 4 nm in length membrane embedded domain, it is important to include the backbone with the amino acid side chain to accurately determine the mechanism of protein targeting to lipid droplets

Our PMFs show small but significant differences between residues in bilayer and monolayer membranes. First, the free energy through the phospholipid regions is lower in monolayer membranes, compared to bilayer membranes. This is observed at the free energy minimums around the PL carbonyls, where it is about .25 kcal/mol lower in monolayer membranes compared to bilayer membranes. Also, the free energy maximums, around the end of the PLs, are also lower by about 1 kcal/mol in the monolayer membranes. Second, in monolayer membranes, once residues have passed the PL tails into the NL core, the free energy is significantly lowered

compared to the end of the PL tails. Finally, these effects are observed for all types of non-charged residues fairly equally, including hydrophobic and polar residues. These results suggest why lipid droplet membranes are more promiscuous for amphipathic helix targeting – the free energy is simply lower for all residues in monolayer membranes.

3.2 Results

3.2.1 Lipid Packing Defect Distributions in Lipid Droplets with Various Compositions

To calculate single residue permeation PMFs, we decreased the membrane area compared to previous work(Prevost et al., 2018), with a membrane are of 4nm x 4nm, to increase the computational efficiency. We also decreased the number of types of neutral lipids – instead of a 1:1 molar ratio of triolein to cholesteryl oleate, we only simulated with triolein within the neutral lipid layer – to reduce the system complexity. We then simulated a monolayer system with a 4 nm thick slack of triolein between the two phospholipid leaflets to determine if the lipid packing defects are significantly different for monolayer with both triolein and cholesteryl oleate compared to a monolayer with only triolein. Packing defects, defined as whether a lipid tail is accessible to the solvent, were increased in lipid droplet-like monolayer systems with only triolein (Figure 3-1). Actual lipid droplets, which vary in SE composition from 0%-25% (Figure this out and cite), will have packing defect distributions somewhere between these two, which both exhibit significantly more frequent large packing defects compared to a bilayer with the same phospholipid composition. A monolayer system with only triolein should then represent the maximum difference between a monolayer and bilayer.

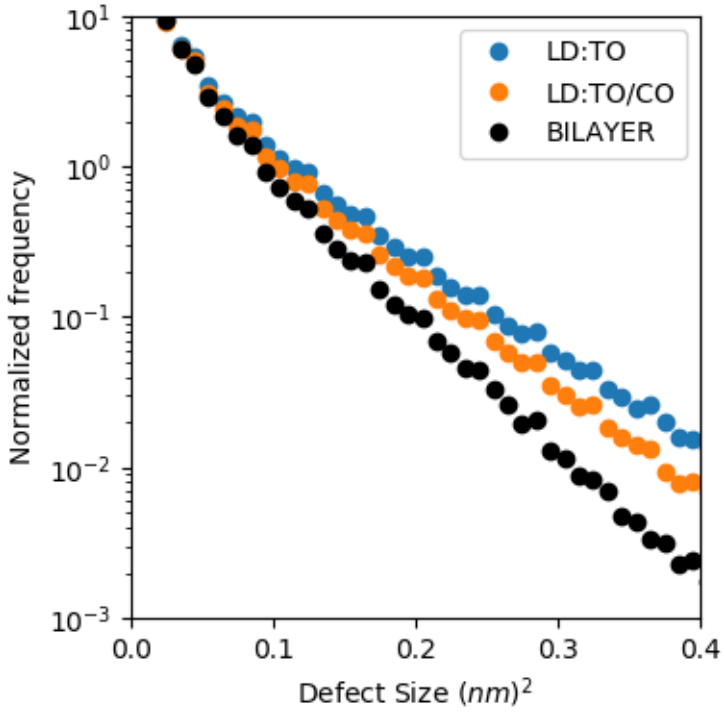

Figure 3-1 Defect Distributions for monolayer membranes with different compositions
Lipid packing defect frequencies are shown for three different membranes: Lipid droplet-like membrane with 100% triolein (LD:TO, blue) for the neutral lipid layer, lipid droplet-like membrane with 50% triolein and 50% cholesteryl oleate (LD:TO/CO, orange), and a bilayer membrane (BILAYER, black). LD membranes with only triolein have larger packing defects compared to LD membranes with cholesteryl oleate, due to the greater interdigitation of the triolein with the PL tails, compared with cholesteryl oleate.

Figure 3-2 depicts a snapshot of the bilayer and monolayer membrane systems (Panel A) and the Z-density profiles for each system (Panel B). Similar to previous manuscripts (MacCallum et al., 2008), we describe the bilayer by dividing it into four regions, though we have added an additional two regions to the monolayer system to describe the neutral lipid (NL) phases (for a total of six regions in the monolayer). Region 1 (R1) contains mostly bulk TIP3P water, with a small amount of PL headgroups. Region 2 (R2) is primarily comprised of the PL headgroups,

though it is solvated with water, and contains a small portion of PL tails. Region 3 (R3) describes the transition from a polar environment at the charged headgroups to the hydrophobic PL tails. R3 begins at the crossover in density between PL head and PL tails and ends at the maximum density of PL tails. Region 4 (R4) contains only hydrophobic tails, though in the case of the monolayer it is also occupied by TAG tails. For the monolayer, region 5 (R5) begins at the crossover in densities between the PL tails and the NL tails. Region 6 (R6) is the bulk TAG phase. Going from R5 to R6, there is a decrease in TAG tails, accompanied by an increase in TAG glycerols. Often, there is significant interdigitation between the TAG tails and the PL tails, but the TAG glycerols remain in the bulk TAG phase.

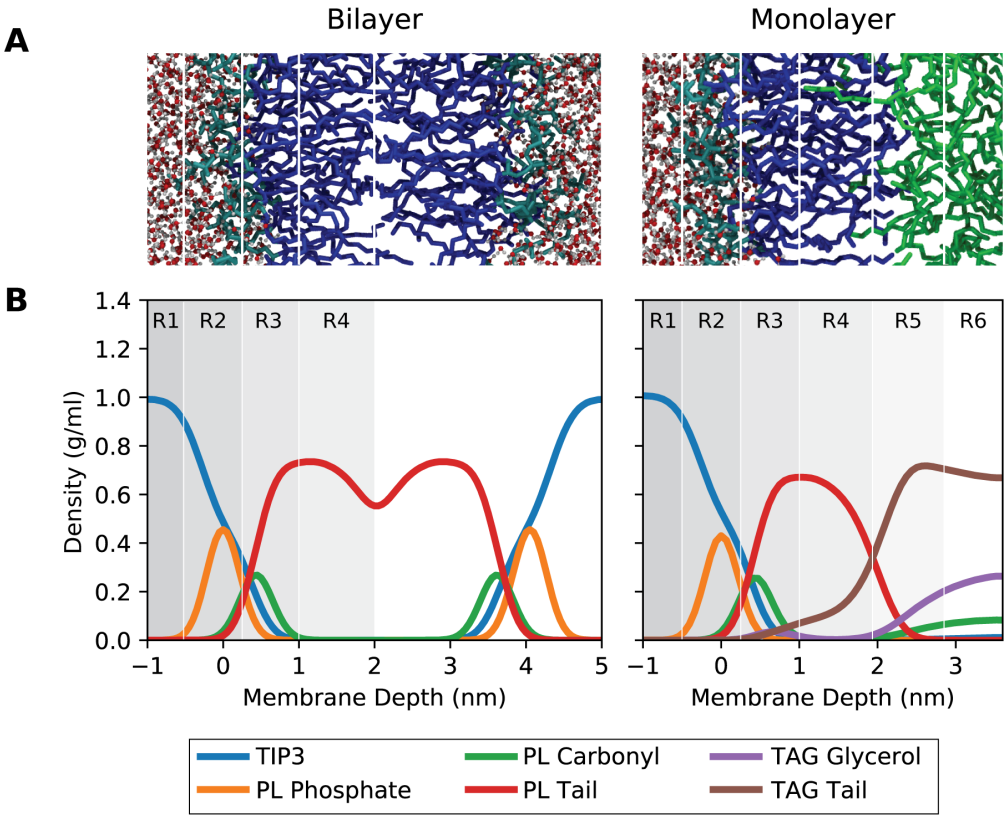

Figure 3-2 Snapshot and Z-density profile of bilayer and monolayer membranes
(A) Snapshot of the bilayer and monolayer systems. TIP3 water is represented with ball and stick (red and white), the PL heads including the glycerol as cyan cylinders, Pl tails as blue cylinders, and NLs as green cylinders. The NLs partially mix with the PL tails, increasing the area per phospholipid.
(B) Density of the monolayer and bilayer systems along the z-axis (the membrane normal). The different shades of grey represent the different regions in the membrane (R1 through R6) as described in the text. The Z-densities of the different regions of the PLs are largely similar in both the bilayer and monolayer, except for the PL tail region.

3.2.2 Distribution of Small Hydrophobic Residues: Ala, Val, Leu, Ile

The PMFs for the small hydrophobic residues (Ala, Val, Leu, Ile) are depicted in Figure 3-3.

These residues all exhibit similar behavior in both membrane types in regions 2-4: a small barrier

in R2 upon moving through the charged headgroups, a minimum just below the PL carbonyls in R3, and a large barrier in R4. In the monolayer, the barrier in R4 is significantly lowered for the larger hydrophobic residues, Ile and Leu. Additionally, the free energy minimum within the TAG core is accentuated. While in the bilayer, the free energies of all four residues are consistently within 2 kcal/mol of each other, the R4 barriers in the monolayer range from 3 kcal/mol (Ala) to -1 kcal/mol (Ile). Furthermore, the R6 minimum is 1 kcal/mol for Ala, and for Ile, it is even the global free energy minimum, at -3 kcal/mol.

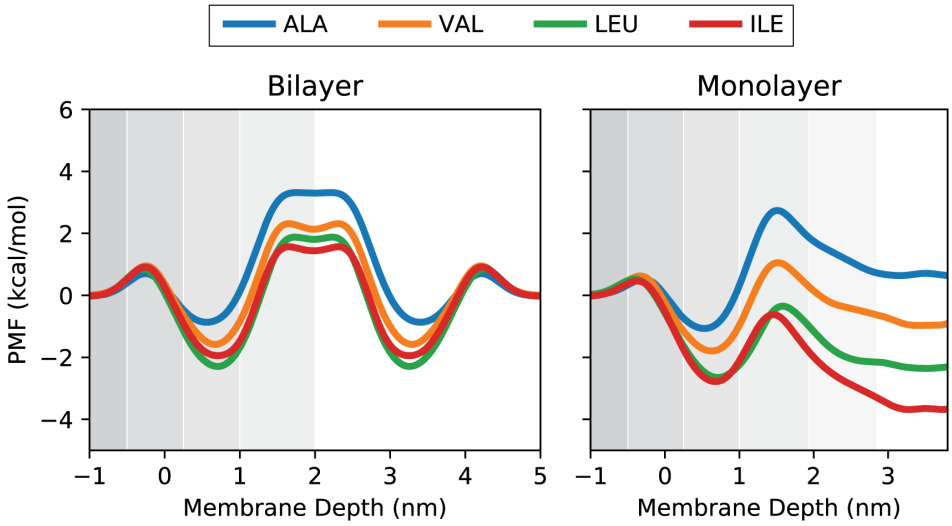

Figure 3-3 PMFs for Small Hydrophobic Residues in Bilayer and Monolayer
All PMFs are set to zero in bulk water. The different regions of the membranes are colored in different shades of grey, corresponding to the labels in Figure 3-2. While all PMFs are quite similar in the bilayer, the PMFs in the monolayer are significantly different in R4-R6, all affected by the TAGs.

3.2.3 Distribution of Aromatic Residues: Phe, Trp

The PMFs for the large hydrophobic residues are shown in Figure 3-4. Trp, unlike the other hydrophobic residues, does not have a barrier within R2 upon inserting into the membrane. Both of these residues have large minima within R3, as well as significant barriers in the bilayer within R4. This barrier is lowered by over 3 kcal/mol for Trp in the monolayer, compared to the bilayer. These residues are notable in that they contain the largest gain in free energy upon moving from the bulk to R3 in either membrane. Inserting from the bulk to the monolayer is favorable for these residues throughout all 5 regions within the monolayer, unlike R4 in the bilayer.

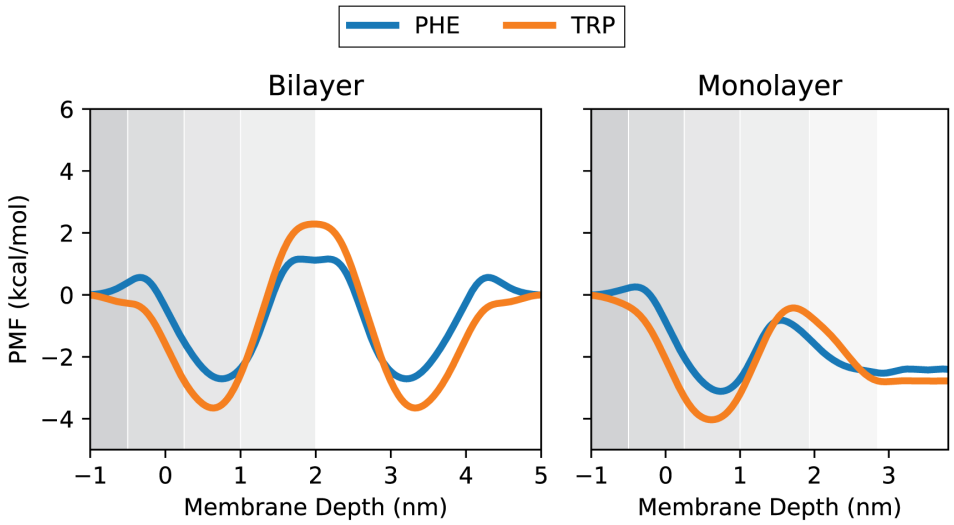

Figure 3-4 PMFs for Large Hydrophobic Residues in Bilayer and Monolayer
All PMFs are set to zero in bulk water. The different regions of the membranes are colored in different shades of grey, corresponding to the labels in Figure 3-2. The aromatic residues have the largest preference for inserting into either membrane.

3.2.4 Distribution of Polar Residues: Thr

The PMFs for polar residues are shown in Figure 3-5. Thr exhibits only a small free energy minimum in R2-R3 of less than 1 kcal/mol and a large barrier of over 5 kcal/mol in R4 in the bilayer. The barrier in the monolayer is quite large as well, and is largely discouraged from accessing the TAG core due to the high free energy within the hydrophobic tails. While these residues are unlikely to insert into the hydrophobic region of the membrane, there is a slight decrease in the free energy minimum in R3 as well as the free energy maximum in R2.

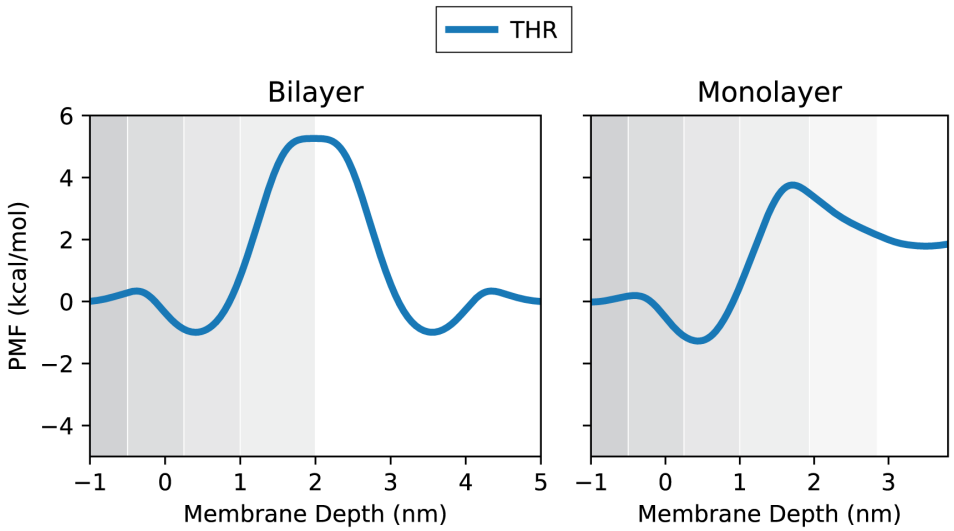

Figure 3-5 PMFs for Polar Residues in Bilayer and Monolayer
All PMFs are set to zero in bulk water. The different regions of the membranes are colored in different shades of grey, corresponding to the labels in Figure 3-2.

3.3 Discussion

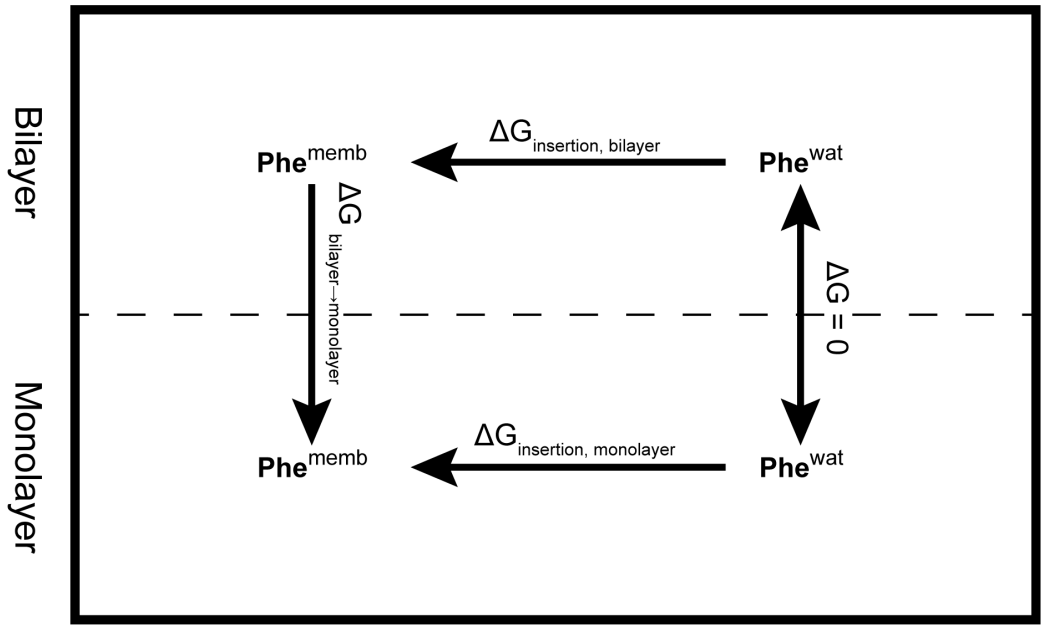

Figure 3-6 Thermodynamic Cycle for Calculating Free Energy Difference Between Bilayer and Monolayer for Phe
The free energy of an amino acid in bulk above a bilayer membrane and above a monolayer membrane is equivalent. Thus, by calculating the insertion free energy ($\Delta G_{insertion}$) of residues into both bilayer and monolayer membranes with metadynamics, we can obtain the free energy difference for a residue relocalizing from a bilayer to monolayer.

Our permeation results show how amino acids prefer to distribute within bilayer and lipid droplet-like membranes. Across all of the amino acids, the free energy of insertion was less in the monolayer compared to the bilayer. Since the free energy is equivalent for a single amino acid in bulk water whether it is near a bilayer or monolayer membrane, we can make direct comparisons between the two PMFs, as well as calculate the FE for an amino acid relocalizing from a bilayer to a lipid droplet-like membrane (Figure 3-6). Using these PMFs, one can make

an estimate for whether a protein comprised of these amino acids has a preference for bilayer or lipid droplet membranes.

The PMFs for amino acids in both the bilayer and monolayer membranes exhibit the same general form: a small barrier in R2, a free energy minimum in R3, and a barrier in R4. But, the relative free energies between the free energy minima and maxima in the PL regions are quite different (Figure 3-7). The free energy minima in the monolayer was on average 0.25 kcal/mol less than in the bilayer. The free energy maxima in the PL region was on average 1.5 kcal/mol less in the monolayer than in the bilayer. Since this trend is observed across the range of amino acids, it is likely a result of differences in entropic effects, rather than enthalpic effects. As we (Prevost et al., 2018) and others (Bacle et al., 2017) have shown, lipid droplet-like membranes have an increase in lipid packing defects due to the increase in interdigitation into the PL tails. This simply increases the space into which amino acids can insert, increasing the entropy and therefore lowering the free energy.

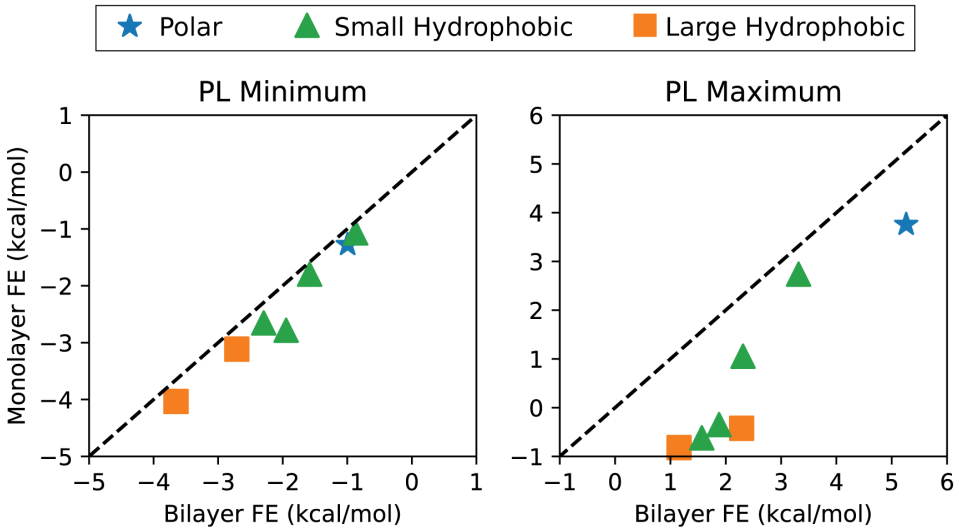

Figure 3-7 Comparisons of Extrema in Bilayer and Monolayer Membranes for Amino Acids
The free energy minimums (left) and maximums (right) within the PL regions are compared for bilayer and monolayer membranes. The dotted line shows equality. All free energy minima are to the right of the equality line, showing an average of ~0.25 kcal/mol decrease in free energy in the monolayer. The effect of the NLs is more pronounced at the PL maximum (at the edge of the PL tails), where the monolayer free energies are on average 1 kcal/mol lower in free energy.

The single residue PMFs also provide a mechanism for why certain amphipathic helices are more easily able to bind to lipid droplets as opposed to the ER (Čopič et al., 2018; Prevost et al., 2018). Regions 2 and 3 have a slightly lower free energy in the monolayer compared to the bilayer, which should allow all amphipathic helices to more easily bind to lipid droplet membranes. Additionally, increasing the length of the amphipathic helix while maintaining the same hydrophobic moment should also increase targeting, as a simple sum of the free energies should lead to increased targeting.

3.4 Conclusion

We demonstrate here the differences in the free energy amino acid insertion into bilayer and lipid droplet membranes using transition-tempered metadynamics. An increase in lipid packing defects allows amino acids of all types to more easily and more stably insert into monolayer membranes. Larger stabilization is observed in the phospholipid tail regions in the monolayer, which directly interact with the neutral lipids. These free energy differences explain why proteins with amphipathic helices are observed to more easily bind to lipid droplet membranes.

3.5 Methods

3.5.1 General Simulation Parameters

Simulations were performed using the GROMACS(Abraham et al., 2015) (version 2016) simulation engine with the CHARMM36 lipid(Klauda et al., 2010) and protein(Best et al., 2012; MacKerell et al., 1998) force fields. Biased simulations were also conducted in GROMACS, with the addition of the PLUMED2(Tribello et al., 2014) plugin (version 2.3). Simulations were integrated with a 2 fs timestep. Non-bonded VDW interactions were cut-off at 1.2 nm and were switched to zero between 1.0 and 1.2 nm. Electrostatic interactions were evaluated using the Particle Mesh Ewald(Essmann et al., 1995) algorithm. Bonds to hydrogen were constrained using the LINCS(Hess, 2008) algorithm. Temperature was maintained at 310 K using the stochastic velocity rescaling thermostat(Bussi et al., 2007) with a coupling time constant of 0.1 ps for simulations that were run in the isothermal-isobaric (NPT) ensemble as well as the canonical ensemble (NVT). In constant pressure simulations, the pressure was maintained semiisotropically using the Parrinello-Rahman(Parrinello and Rahman, 1981) barostat at a

pressure of 1.0 bar, a compressibility of $4.5x10^{-5}$, and a coupling time constant of 5.0 ps. Coordinates were saved every 10 ps.

3.5.2 Single Residue Simulation Setup

Membrane patches for the bilayer and monolayer were initialized according to procedure described previously. Briefly, a membrane patch was generated with CHARMM-GUI(Jo et al., 2007; Jo et al., 2008; Jo et al., 2009; Lee et al., 2016; Wu et al., 2014) with 34 1-palmitoyl-2-oleoyl-sn-glycero-3-phosphocholine (POPC), 14 1,2-dioleoyl-*sn*-glycero-3-phosphoethanolamine (DOPE), and 4 1-stearoyl-2-arachidonoyl-sn-glycero-3-phosphoinositol (SAPI) lipid molecules. Positional restraints were initially placed on the lipids and were slowly relaxed according to the CHARMM-GUI equilibration procedure. For the monolayer system, a 4 nm box of neutral lipids was inserted between the equilibrated bilayer leaflets. Restraints were placed on the neutral and phospholipids and slowly relaxed using the same equilibration procedure. Each system was then further equilibrated for 1 μs in the isothermal-isobaric ensemble.

3.5.3 Single Residue Metadynamics

Each peptide system was generated as follows. First, each peptide was generated with the **psfgen** plugin in VMD(Humphrey et al., 1996) with an amidated N-terminus and methylated C-terminus, and solvated in a 4x4x4 nm^3 TIP3P water box. Each peptide was then simulated for 100 ns in the isothermal-isobaric ensemble. Next, each peptide was placed 1 nm from the phosphate plane of the pre-equilibrated membrane patches. Each membrane-peptide system was then re-solvated and re-ionized with TIP3P water and 150 mM NaCl. Restraints were then placed on the peptide and the lipids and slowly relaxed, in the same manner as described above.

Transition-Tempered Metadynamics (Dama et al., 2014b; Sun et al., 2016) was then carried out for 2 μs and 3 μs for each bilayer and monolayer replica, respectively. Four independent replicas were calculated for each peptide-membrane system. The collective variable was defined as the z-distance between the center of mass of the residue side chain and the midplane of the membrane, as determined by the center of mass of all phosphate atoms in the membrane. Hills were deposited every 2 ps with a height of .001 kJ/mol/nm, a width of .2 nm, a bias factor of 10, a threshold of 10 kJ/mol/nm, an exponential decay factor (α) of 0.5, and transition wells at the carbonyl level of the phospholipids. At least five transitions through the membrane were observed for each replica.

3.5.4 Lipid packing defects

Packing defects were calculated using a described procedure in Cui et al. (Cui et al., 2011) and similar to that described in Vamparys et al. (Vamparys et al., 2013). In brief, the solvent accessible surface area of the hydrophobic tails (defined as up to the glycerol atoms) was calculated using VMD (Humphrey et al., 1996) using a probe radius of 0.3 nm. The points along this solvent accessible surface area are then projected onto the plane of the membrane. To simplify the calculation, the surface is then divided into bins with size 0.16 nm^2. Each of these points is then placed into a bin such that it is either occupied or not occupied. Occupied bins are considered part of the same defect cluster if they are within 0.25 nm A histogram of defect sizes was then tabulated for each system. The histogram was then fit to an exponential decay $p(x) = ce^{-ax}$ where x is the defect size, $p(x)$ is the probability of finding a defect of size x, c is a constant, and a is the decay rate in units of nm^{-2}.

3.6 Acknowledgements

We thank Rui Sun for his help with the simulations and Thomas Dannenhoffer-Lafage for comments on this manuscript. The simulations in this work used the Extreme Science and Engineering Discovery Environment (XSEDE), which is supported by the National Science Foundation grant number ACI-1548562. Specifically, it used the Bridges system at the Pittsburgh Supercomputing Center (PSC) through allocation number TG-MCA94P017. This work was also completed in part with resources provided by the University of Chicago Research Computing Center (RCC).

Chapter 4. Targeting of hydrophobic hairpin motifs to the surface of lipid droplets from the ER

Work in this chapter was conducted in collaboration with María-Jesús Olarte, Tobias C. Walther, and Robert V. Farese Jr. at the Harvard Medical School. Experiments were conducted by María-Jesús Olarte.

4.1 Introduction

Lipid droplets (LD) are cellular organelles that store excess metabolic energy in the form of neutral lipids. Improper function of lipid droplets is associated with a number of diseases, including lipodystrophy, obesity/type 2 diabetes, and atherosclerosis (Krahmer et al., 2013a; Pol et al., 2014; Welte, 2015).

Lipid droplets are unlike other organelles because they contain a core of neutral lipids (NL), composed of triacylglycerols (TG) and sterol esters (SE), and are surrounded by phospholipid (PL) monolayer membranes, not bilayers membranes (Fujimoto and Parton, 2011; Thiam et al., 2013b; Walther and Farese, 2012; Welte, 2015). The LD monolayer is covered with proteins, which include enzymes and regulatory proteins involved in lipid synthesis (Kory et al., 2016).

Current understanding suggests two pathways for protein targeting to LDs (Kory et al., 2016). Class I proteins are inserted into ER and have membrane embedded domains. Proteins of this type typically contain long stretches of hydrophobic amino acids. Class I LD proteins in the ER can only have a non-membrane domain on the cytosolic leaflet, as there is no lumen leaflet in the LD, and therefore require a membrane domain likely with hairpin loops. These proteins relocalize to LDs through physical connections, called ER-LD bridges (Jacquier et al., 2011; Thiam et al., 2013a; Wilfling et al., 2013).

Class II proteins are translated in the cytosol and directly bind LD membranes. This class of proteins contains perilipins as well as metabolic proteins (Bickel et al., 2009; Kimmel and Sztalryd, 2016; Krahmer et al., 2011; Miyanari et al., 2007; Ohsaki et al., 2016; Rowe et al., 2016). Class II proteins typically contain amphipathic helices (Bouvet et al., 2013; Bulankina et al., 2009; Krahmer et al., 2011), which they use to sense out and bind to LD membranes(Kory et al., 2016). Previous research by us (Prevost et al., 2018) and others (Čopič et al., 2018) have shown that having a strong hydrophobic face on the amphipathic helix is key to binding LDs, and that binding LDs is easier than binding to bilayer membranes. This is due to the increase in packing defects on the surface of LDs, which is caused by the interdigitation of the neutral lipids with the PL tails (Bacle et al., 2017; Prevost et al., 2018), even though the PL composition is similar to the ER (Bartz et al., 2007; Choudhary et al., 2015). Additionally, as the free energy due to the hydrophobic-hydrophilic partitioning of the amphipathic helices into the membrane is likely additive by residue, increasing the length of amphipathic helices while maintaining the hydrophobicity leads to an increase in binding (Čopič et al., 2018).

In this manuscript, we set out to determine what drives these proteins to target to LDs. Do Class I proteins target in a similar process to Class II proteins - preferentially, but not specifically, large hydrophobic residues drive targeting due to the larger and more frequent packing defects on LD surfaces. Or, is it driven by some other mechanism, such as protein conformational change.

Here we combine molecular dynamics simulations with experimental approaches to show how the membrane embedded domain of GPAT4 (glycerol-3-phosphate O-acyltransferase) targets to LDs. We show that GPAT4 has sequence specific features that allow it to stabilize in both bilayer and LD membranes. These features drive a conformational change as GPAT4 moves

from the ER to LDs. Positively charged and large hydrophobic residues at specific locations in the sequence drive the conformational change and relocalization to LDs. Furthermore, the increase in packing defects in the LD membranes aids in the preference of large hydrophobic residues targeting to LDs. We suggest that other Class II proteins have similar properties in order to target to LD membranes.

4.2 Results and Discussion

4.2.1 GPAT4 Hairpin Contains Sequence Specific Residues Required and Sufficient for Targeting to Lipid Droplets

We first set out to determine the minimum sequence required for targeting to LDs. We expressed only the hairpin domain of GPAT4 fused to mCherry in *Drosophila* S2 cells and compared this domain with the full length GPAT4 (FL-GPAT4) for LD targeting. As seen in Figure 4-1, both FL-GPAT4 and the hairpin target to LDs from the ER. Since only the hairpin is required for targeting, it is likely that the cytosolic domain of the protein is not involved in driving LD targeting.

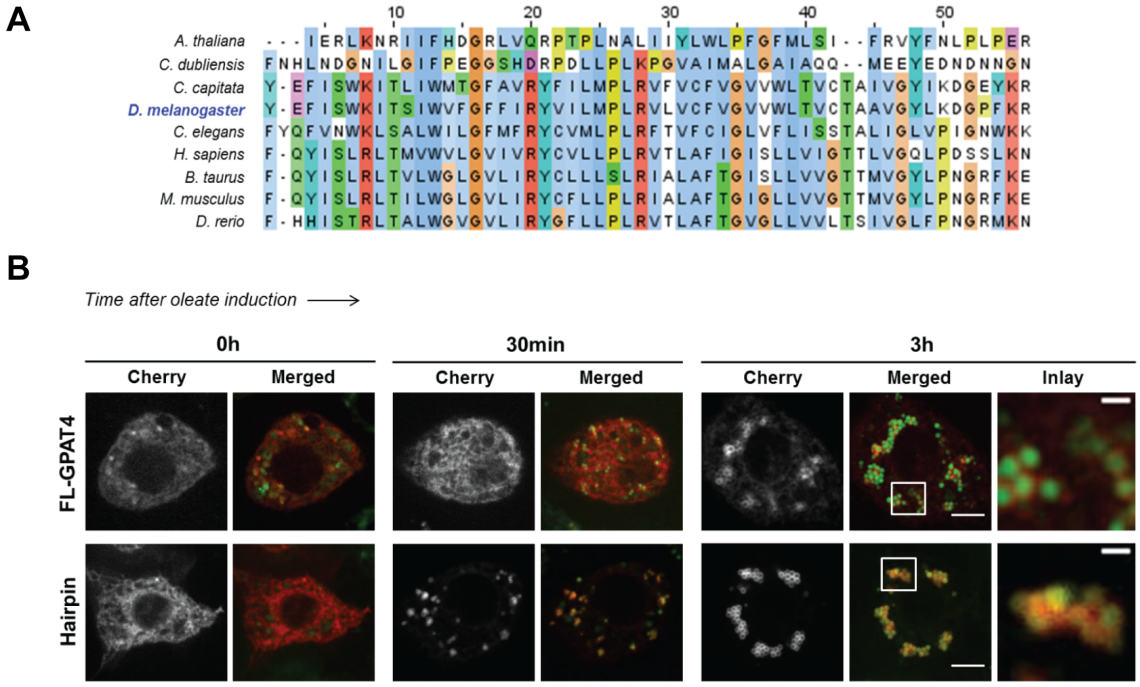

Figure 4-1 GPAT4 Hairpin is Sufficient for LD Targeting
(**A**) GPAT4 hairpin sequence in *D. melanogaster* compared with other species. Many residues are conserved, including hydrophobic residues (blue), charged residues (red), and polar residues (green).
(**B**) Analysis of LD targeting ability of full length GPAT4 (FL-GPAT4) compared with the hairpin domain of GPAT4. *Drosophila* cells were transfected with mCherry-tagged constructs and incubated with 0.5 mM oleic acid. LDs were stained with BODIPY. Representative images are shown. Scale bar, 5 μm (merge), 1 μm (inlay). The 44-residue long hairpin domain is sufficient for LD targeting from the ER.

We then attempted to determine the specificity of the sequence of the GPAT4 hairpin. Leaving in place the residues at the end of the hairpin, as well as the residues around the hinge of the protein (P185, L186, R186), two different mutants were constructed: a scrambled helix, where the rest of the residues within the hairpin were randomly scrambled; and an artificial helix, where these residues were replaced randomly to maintain similar hydrophobicity of the hairpin (see sequences in Table 4-1). These two constructs did not re-localize to LDs from the ER

(Figure 4-2), suggesting that the sequence of GPAT4 contains specific residues at specific locations that are required for targeting.

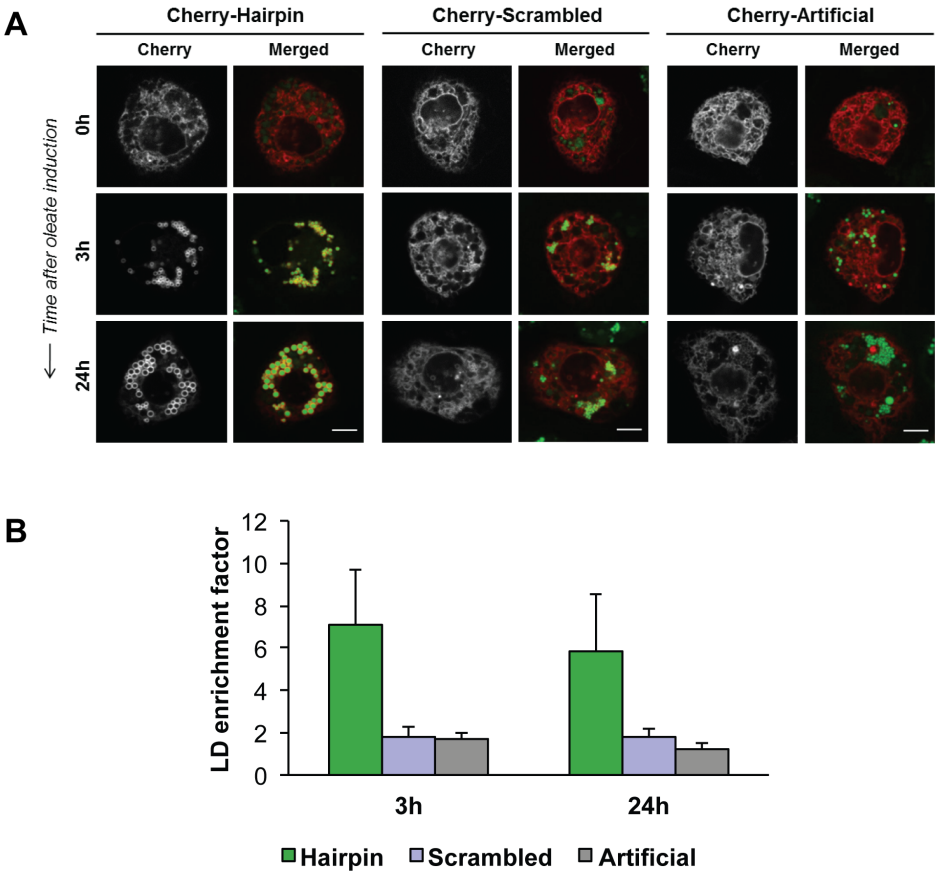

Figure 4-2 GPAT4 Hairpin Contains Sequence Specific Residues Required for LD Targeting

(**A**) Analysis of LD targeting ability of GPAT4 hairpin compared with two hairpin-like constructs. Randomizing the residues in the GPAT4 hairpin sequence (Scrambled) abolishes targeting, as does replacing the replacing the residues with those of similar hydrophobicity (Artificial).

(**B**) Quantification of the protein signal on LDs, as compared to the ER. Data is represented as mean + standard deviation.

To determine which specific residues are required for LD targeting, we conducted a sequence alignment with the GPAT4 hairpin and evolutionarily related proteins to determine which residues are strongly conserved. Three of the residues which are highly conserved are charged: K167, R179, and R187. To determine the importance of these three charged residues in LD targeting, each of these three residues was mutated to alanine and assayed for LD binding (KRR_AAA mutant). The KRR_AAA mutant exhibited a decrease in LD enrichment compared to the WT hairpin (Figure 4-3), though some targeting was still observed. This suggests that the charged residues are not the sole determinant of targeting.

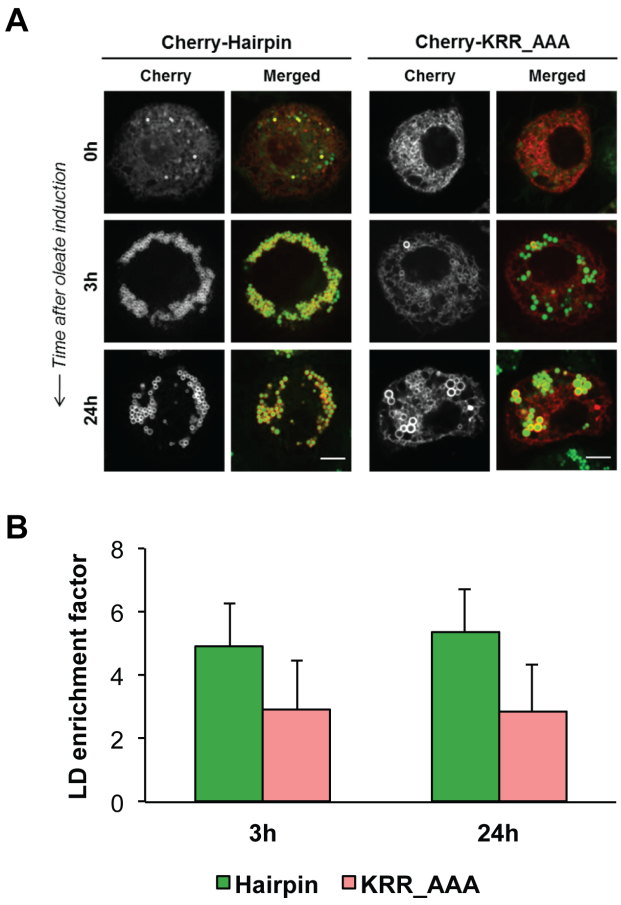

Figure 4-3 Charged Residues on GPAT4 Play a Role in LD Targeting

Figure 4-3 **Cont.**
(**A**) Analysis of LD targeting ability of GPAT4 hairpin compared with a mutant with K167, R179, and R187 mutated to alanine (KRR_AAA). Targeting is diminished significantly for the charged mutant.
(**B**) Quantification of the protein signal on LDs, as compared to the ER. Data is represented as mean + standard deviation.

To assess the importance of each of these charged residues, single point mutants of each of these residues were expressed. Of these single point mutations, all showed at least a small decrease in targeting of 15%, while R179A showed a decrease in targeting of 40% (Figure 4-4). Since the ER and LD membranes contain similar concentrations of PLs(Bartz et al., 2007; Choudhary et al., 2015), it is likely that these charged residues play a structural role in GPAT4 and therefore affect LD targeting.

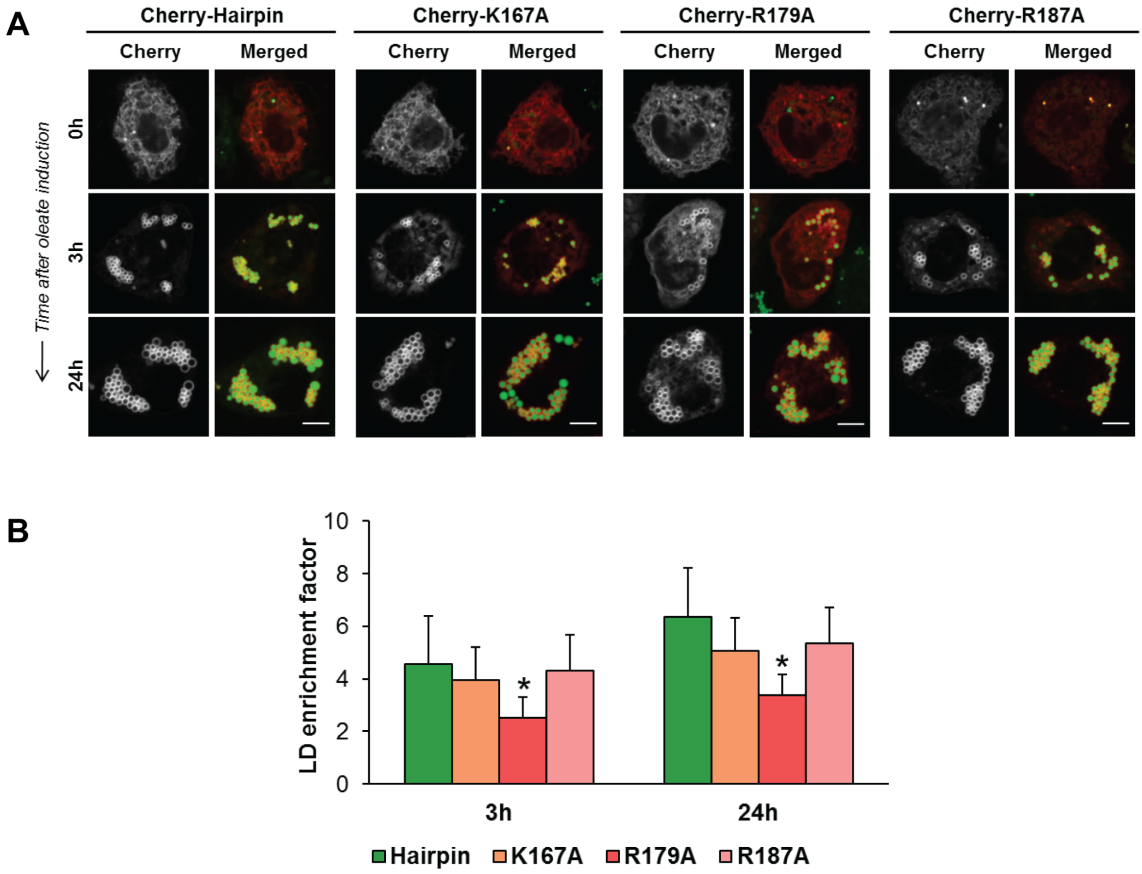

Figure 4-4 R179 is Key to LD Targeting by GPAT4 Hairpin
(**A**) Analysis of LD targeting ability of GPAT4 hairpin compared with single point mutations of the charged residues.
(**B**) Quantification of the protein signal on LDs. Each of the charged mutants shows a decrease in targeting, and R179A shows the largest decrease in targeting.

Our previous research on amphipathic helix targeting to LD membranes demonstrated that large hydrophobic residues are key to LD targeting (Prevost et al., 2018). Additionally, structural alignment of the GPAT4 hairpin showed that these large hydrophobic residues (W, F, Y) are highly conserved. We therefore tested whether mutating the large hydrophobic residues (LHR mutant) in the GPAT4 hairpin to valine (sequence in Table 4-1). Targeting was abolished for the

LHR mutant (Figure 4-5). In the case of amphipathic helix targeting to LDs, the types of large hydrophobic residues present were not nearly as important as the presence of many large hydrophobic residues (Prevost et al., 2018).

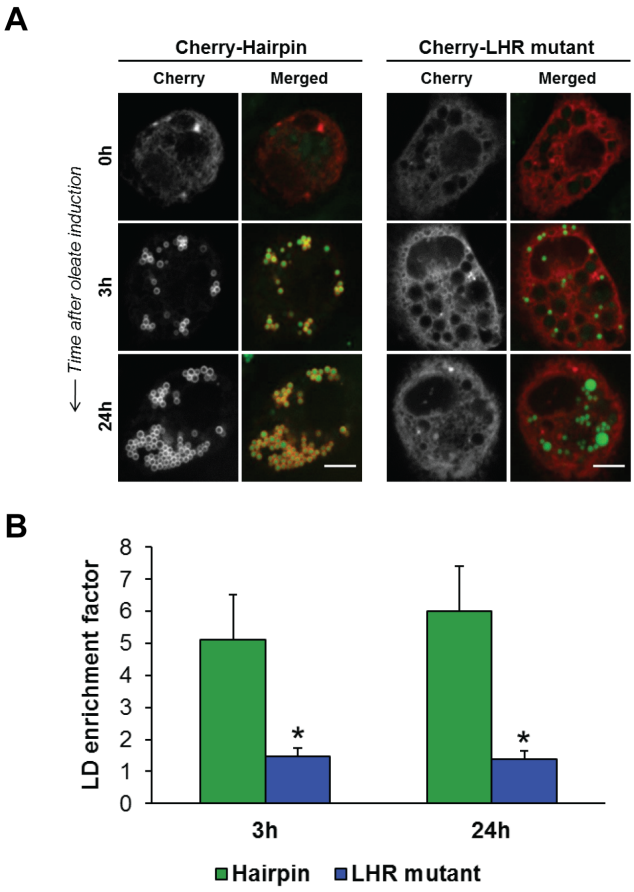

Figure 4-5 Large Hydrophobic Residues are Critical for GPAT Targeting to LDs
(**A**) Analysis of LD targeting ability of GPAT4 hairpin compared with a mutant where the aromatic residues where mutated to Val (LHR mutant). The LHR mutant is observed to be localized primarily in the ER and not on LDs
(**B**) Quantification of the protein signal on LDs. The LHR mutant shows a substantial decrease in LD enrichment.

To explore whether this trend is maintained for membrane-embedded hairpin domains, each type of large hydrophobic residue was mutated to valine (PHE_VAL, TRP_VAL, and

TYR_VAL). In this case, only the Trp mutant showed a decrease in targeting (Figure 4-6). The Phe mutant only had a slight decrease in targeting compared to the WT, and the Tyr mutant displayed an increase in targeting. These mutants suggest that the targeting of proteins with membrane-embedded hairpin motifs does not proceed due to the same features as amphipathic helix-containing proteins. Instead of an increase in hydrophobicity driving targeting, the location of the residues within the structure likely plays an important role.

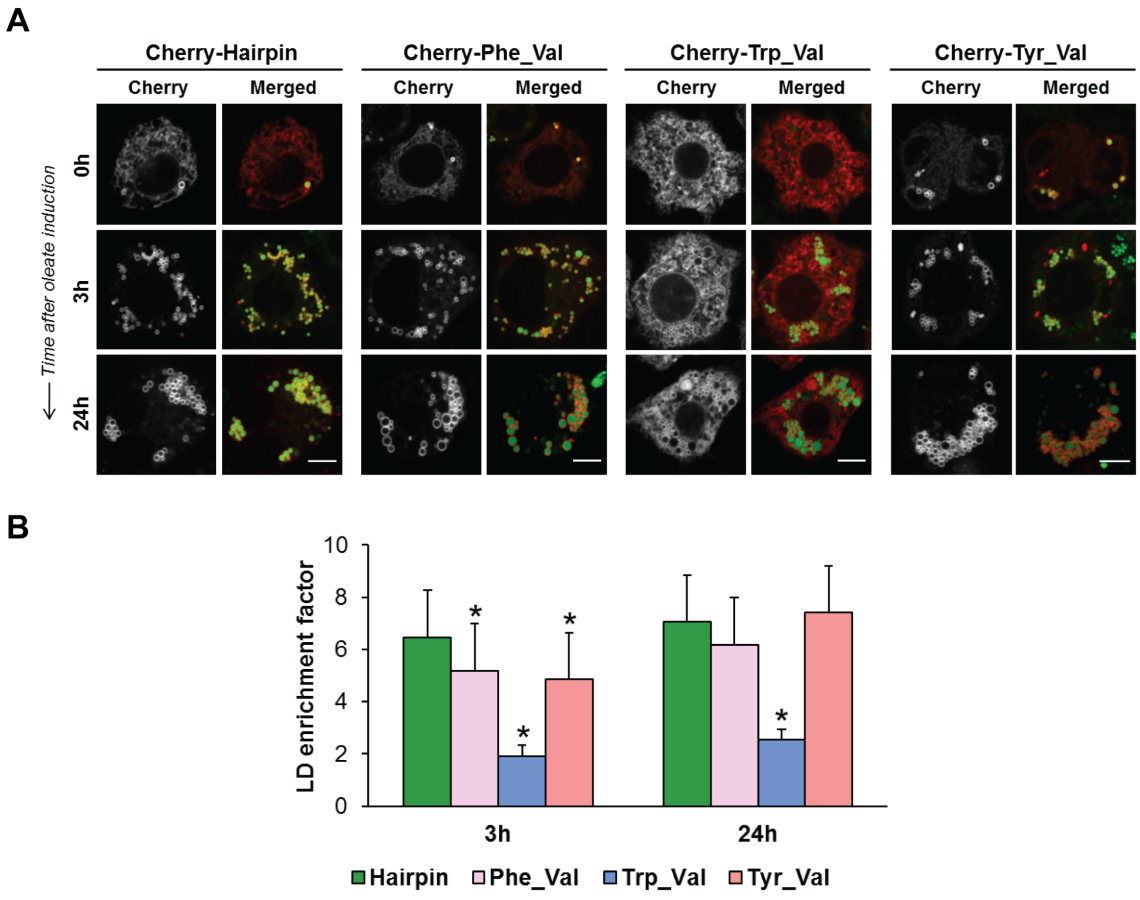

Figure 4-6 TRP Residues Are the Only Aromatic Residues Required for Targeting

Figure 4-6 Cont.
(**A**) Analysis of LD targeting ability of GPAT4 hairpin compared with three mutants, where all of the aromatic residues of a specific type were mutated to Val (Phe_Val, Trp_Val, Tyr_Val). Only the Trp_Val mutant shows a significant change in targeting ability, and is mostly localized to the ER.
(**B**) Quantification of the protein signal on LDs. The Phe and Tyr mutants do not show much change in targeting ability compared to the WT hairpin, but Trp mutant does not relocalize to the LDs.

We further tested the generality of GPAT4 targeting to examine whether other proteins with hairpin domains target to LDs from the ER. Of these proteins, only Alg4 targets to LDs (Figure 4-7). The Alg4 hairpin contains a number of the same sequence features as the GPAT4 hairpin: large hydrophobic residues are distributed along the hairpin domain, and contains a number of charged residues adjacent a proline residue near the center. However, when the Trp and Phe residues were mutated to Val, the Phe mutant showed the largest decrease in targeting in this case (data not shown). From this, we can hypothesize that both the identity and the location of the specific hydrophobic residues are key to targeting.

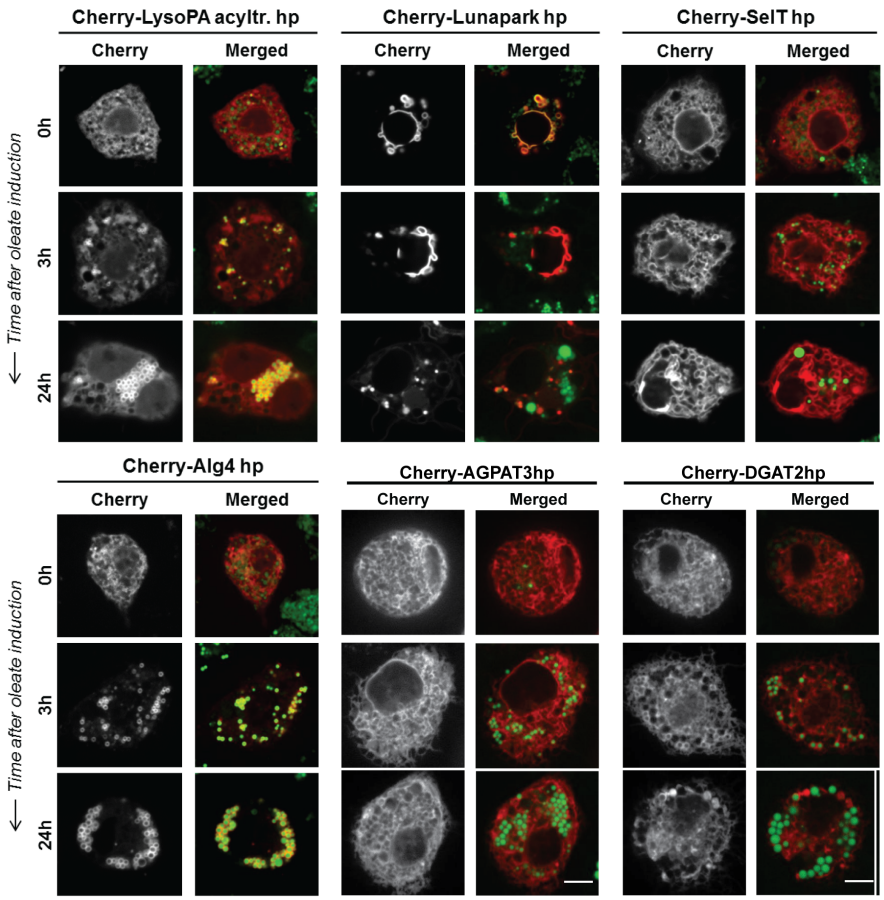

Figure 4-7 Alg4 Targets to LDs in a similar manner to GPAT4
Analysis of LD targeting ability for a series of protein membrane-domains predicted to have hairpins. Of these, only the Alg4 hairpin relocalizes from the ER to LDs. The sequence of Alg4 contains a number of similarities compared to the GPAT4 hairpin.

4.2.2 Molecular Dynamics Simulations Reveal GPAT4 Structural Differences in Bilayer and LD Membranes

Since the structure for the GPAT4 membrane-bound domain has not been resolved experimentally, we predicted the structure using the Rosetta software package. The best 10 scoring structures were all quite similar, showing two helices closely associated with a hinge at

P185. We then relaxed and inserted GPAT4 into bilayer and lipid droplet membranes from Prevost et al. (Prevost et al., 2018), with phospholipid (PL) concentration composed of 65:27:8 palmitoyl-oleoyl phosphatidylcholine (POPC): dioleoylphosphatidylethanolamine (DOPE): stearoyl-arachidonoyl phosphatidylinositol (SAPI) and for the lipid droplet membranes, a neutral lipid (NL) concentration of 1:1 triolein and cholesteryl oleate inside of a flat bilayer. We simulated 3 independent simulations for each membrane type, each for 1 μs.

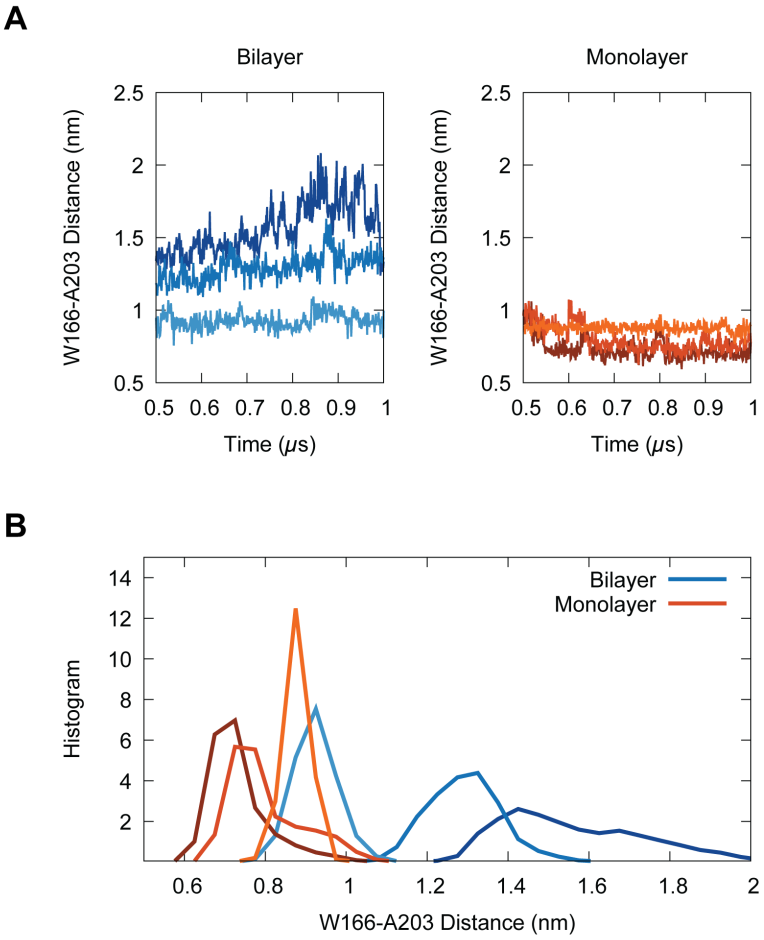

Figure 4-8 W166-A203 Distance in in Bilayer and Monolayer Simulations
(**A**) W166-A203 distance in bilayer (left, blue) and monolayer (right, orange). These residues are located on the two helices at the phosphate plane, and approximate the association of the two helices. The three replicas are shown in different shades of blue (bilayer) and orange (monolayer). In the bilayer simulations, these residues are not interacting, while in the monolayer they are closer and interacting.

Figure 4-8 **Cont.**
(**B**) Histograms of W166-A203 distance in the bilayer and monolayer. While the three replicas in the different membranes did not converge to similar results, in all replicas, the mean of the W166-A203 distance is longer in the bilayer simulations.

In 2 out of 3 simulations of GPAT4 in bilayer membranes, we observe a change in conformation of GPAT4. First, the two helices begin separating, both at the lumen and the cytosolic membrane-water interfaces. Both the distances between W166-A203 and between F177-F193 increase during length of the simulations (Figure 4-8). Additionally, P185 is significantly closer to the cytosolic membrane-water interface in the monolayer compared to the bilayer membranes (Figure 4-9).

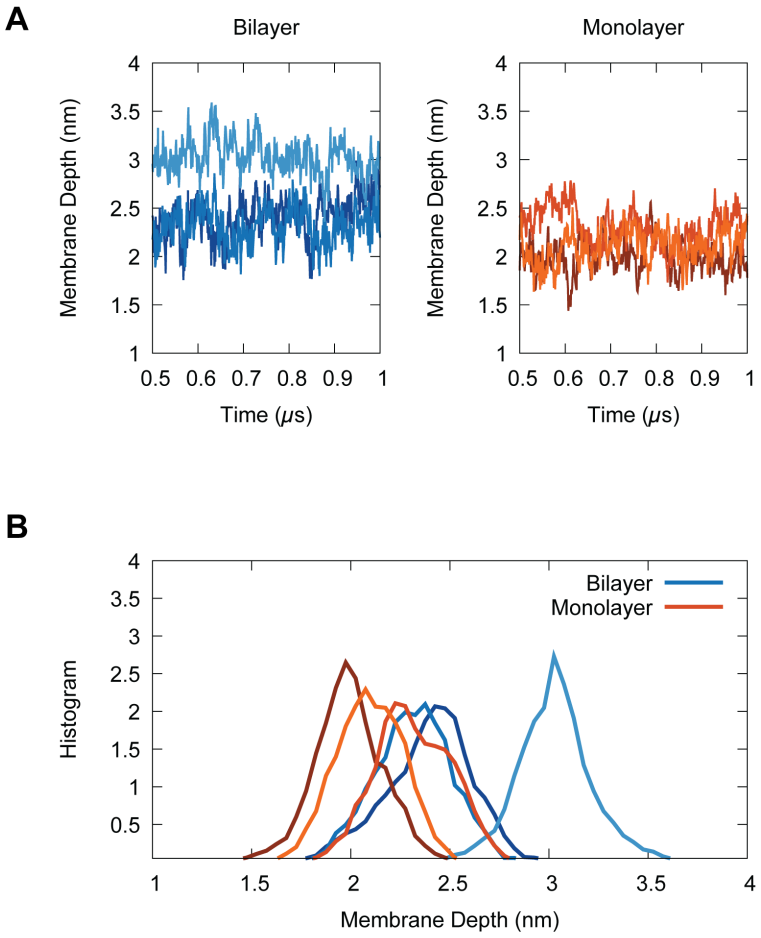

Figure 4-9 P185 Membrane Depth in Bilayer and Monolayer Simulations
(**A**) P185 membrane depth in bilayer (left, blue) and monolayer (right, orange). The membrane depth is calculated in relation to the cytosolic phosphate plane. The three replicas are shown in different shades of blue (bilayer) and orange (monolayer). In the bilayer simulations, P185 is deeper in the membrane, almost interacting with the lumen phosphate plane. In the monolayer, P185 is closer to the cytosolic phosphate plane.
(**B**) Histograms of P185 membrane depth in the bilayer and monolayer. The mean P185 membrane depth is deeper in all of the bilayer simulations than in all of the monolayer simulations.

While the average structure of GPAT4 was observed to be different in bilayer membranes compared to monolayer membranes, it is unclear from these simulations what is the equilibrium structure of GPAT4. The structures in the bilayer are highly varying, and the structures in

monolayer membranes vary as well. The slow relaxation of the lipids prohibits GPAT4 from relaxing to the equilibrium structure. We therefore performed Metadynamics on the distance between W166-A203 to more efficiently sample the separation of the helices, and calculate the potential of mean force (PMF) of separating these helices in both membrane types. After simulating two independent replicas for each membrane type for two μs, we observed structures with distances ranging from 0.5 to 5 nm (Figure 4-10).

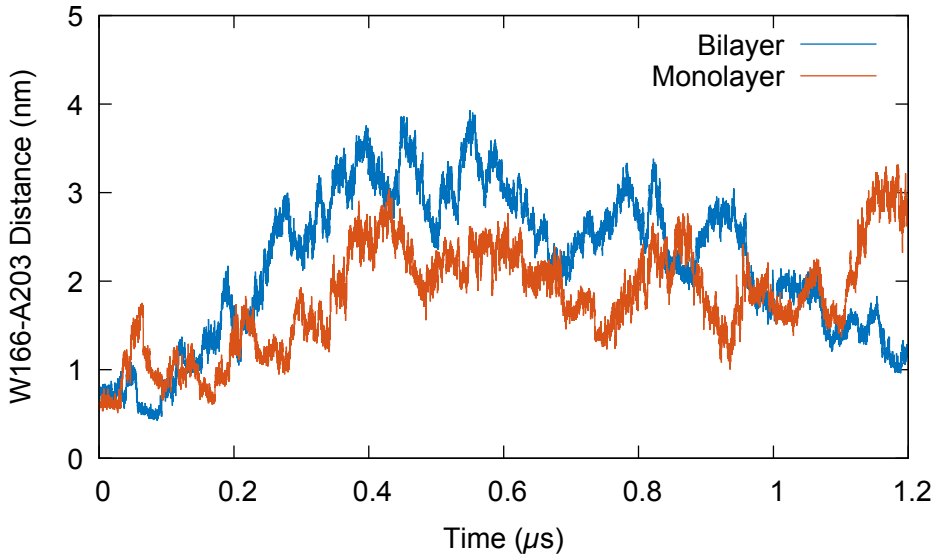

Figure 4-10 W166-A203 Distance in Metadynamics Simulations
The distance between W166 and A203 in bilayer (blue) and monolayer (orange) over time during the metadynamics simulation. While distances between 0.5 and 4 nm were sampled, a full traversal of collective variable space took longer than 1 μs. Converging this free energy surface using metadynamics along this slow collective variable have required significant amount of simulation and clock time.

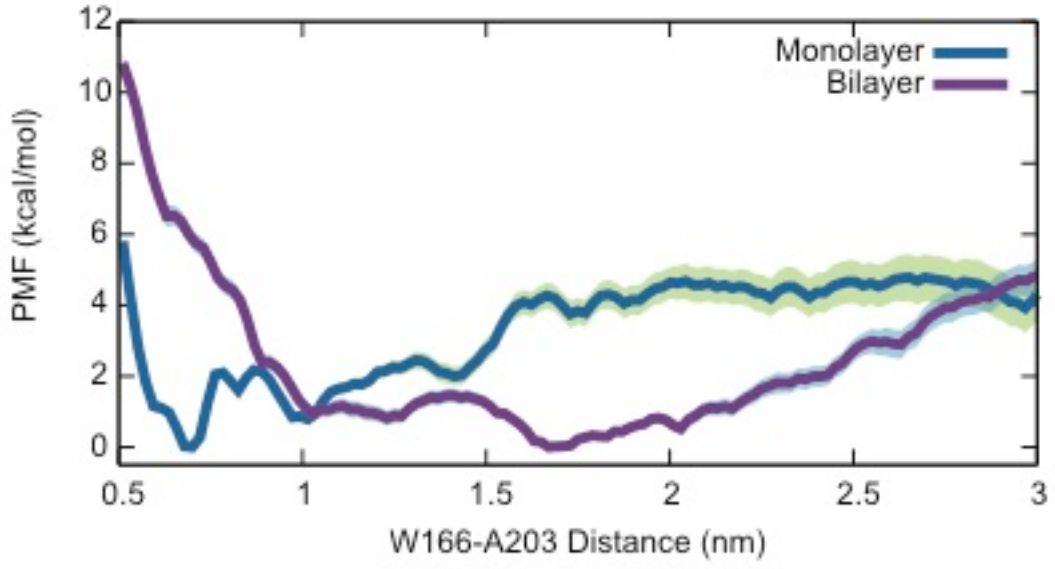

Figure 4-11 Potential of Mean Force for Association of GPAT4 Hairpin Helices.
The PMF for the hairpin association of GPAT4 was calculated along the W166-A203 distance. GPAT4 helices are observed to be close together in the monolayer membrane, with a minimum in the PMF at 0.7 nm. The helices of GPAT4 are further separated in the bilayer, and cannot achieve the close distances observed in the monolayer.

Using the structures generated from the Metadynamics simulations, we performed Umbrella Sampling on the W166-A203 distance in both bilayer and monolayer membraness. The PMF calculating using Umbrella Sampling shows that GPAT4 in a bilayer prefers to be at a helix separation of 1.7 nm, but prefers a much closer separation of 0.7 nm in the monolayer (Figure 4-11).

Inspecting the minimum free energy structures in the bilayer and monolayer, we can verify the structural differences between the two membrane types. In addition to the difference in the association of the helices, we also observe that P185 is closer to the cytosolic membrane-water interface in the bilayer membranes. Additionally, in the bilayer, R179 and R187 are interacting with the charged region of the PLs on the lumen membrane-water interface (Figure 4-12). In the monolayer, R179 is flipped and interacting with the cytosolic membrane interface, while R187 is

solvated by the glycerol oxygens of triolein (Figure 4-12). The 5-residue segment between R179 and the hinge at P185 (seq: YVILM) contains some flexibility required for the two orientations of R179. In the monolayer, this segment is stretched towards the cytosolic interface so that R179 can reach the polar PL region, while the segment is condensed in the bilayer membrane (Figure 4-12).

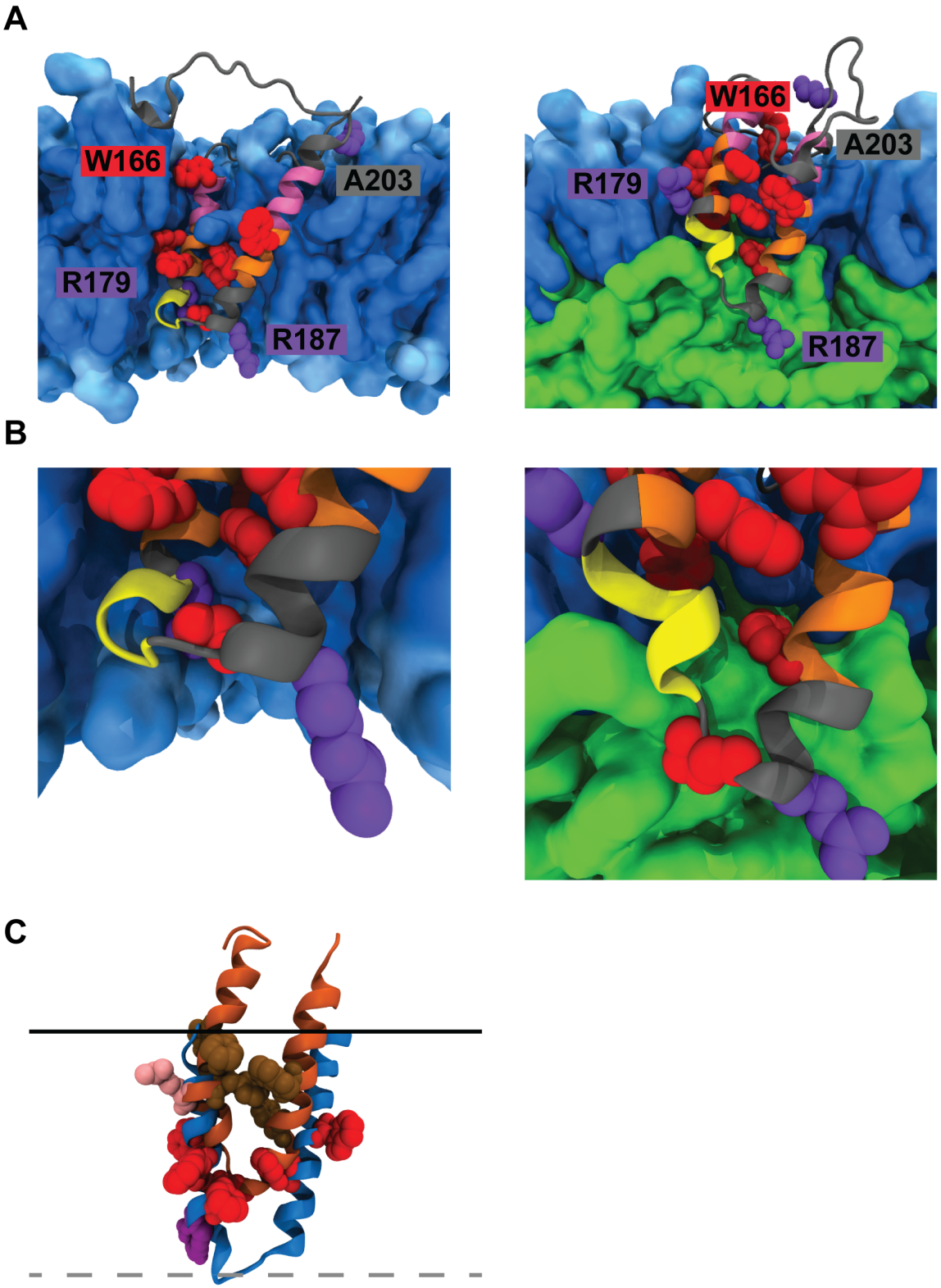

Figure 4-12 Snapshots of GPAT in Bilayer and Monolayer.

Figure 4-12 **Cont.**
(**A**) The helices of GPAT4 are associated in the monolayer (right), while in the bilayer (left) they remain separated. In the bilayer, the two ARG residues (R179, R187) are associated with the lumen leaflet, while in the monolayer R179 interacts with the cytosolic leaflet.
(**B**) The hinge region zoomed in. In the bilayer, the residues between R179 and P185 are stretched parallel to the phosphate plane, while in the monolayer they are stretched perpendicular to the phosphate plane.
(**C**) An overlay of the bilayer (blue ribbon) and monolayer (orange ribbon) GPAT4 structures. The hairpin is shifted significantly towards the cytosolic phosphate plane (solid black line). Instead of R179 (dark purple) interacting with the luminal leaflet (dashed black line) in the bilayer, R179 in the monolayer (pink) interacts with the cytosolic leaflet.

In the bilayer, the mismatch in hydrophobic and hydrophilic regions between the two helices causes them to separate. There are only 11 residues between K167 and R179, while there are 18 residues between R187 and G206. The N-terminal helix is oriented parallel to the bilayer normal, while the C-terminal helix is tilted in order to fit all of the hydrophobic residues within the bilayer. In the monolayer membrane, the hydrophobic regions of the GPAT4 hairpin are more similar in length because R179 interacts with the cytosolic PL leaflet and the 5-residue flexible segment is stretched upwards.

We also inspected whether specific intra-protein or protein-lipid interactions played a role in the targeting. In the simulations, we did not observe the hairpin interacting with a specific type of lipid. Additionally, in the monolayer, we did not observe specific, stable inter-helix residue contacts forming. Instead, hydrophobic residue side chains would interact dynamically with all residues nearby.

4.2.3 Lipid Droplet Preference of GPAT4 is Driven by a Shift Upwards in the Membrane Driven by the Hydrophobic Residues.

From MD simulations, we observe that the charged residues determine the distances between helices and the angle between the helices and the membrane, as they prefer to interact with the

charged phospholipid head regions. But, to re-localize to LD membranes, GPAT4 needs to move R187 from the lumen facing leaflet to the NL region and move R179 from the lumen leaflet to the cytosolic leaflet. These changes are kinetically and thermodynamically unfavorable and therefore require a large gain in free energy elsewhere in order to target to LD membranes. In the bilayer simulations, we observed that the aromatic hydrophobic residues are clustered around the bilayer midplane, while in the monolayer they are localized just below the glycerols of the PLs (Figure 4-12). In the monolayer membrane, these regions of hydrophobic residues (highlighted in orange) replace regions of the helices that are filled will polar and smaller hydrophobic residues (highlighted in pink) in the glycerol region.

To determine the free energy preference occurring due to this switch in residues sitting just below the glycerol level, we can inspect the free energies of residues inserting within bilayer and monolayer membranes (see Chapter 3.), as calculated from Transition-Tempered Metadynamics (Dama et al., 2014b; Sun et al., 2016). In these PMFs, the barrier at the edge of the PL tails is lowered in monolayers as compared to bilayers. Furthermore, the PMF minimum, around the PL carbonyls, is stabilized even further in the monolayer PMFs. The overall lower free energy for residues within monolayer membranes should drive proteins to relocalize to lipid droplet membranes. But, an even larger free energy gain is observed due to the shift in residue positions within the membrane. The hydrophobic residues located near the midplane of the bilayer (Phe, Trp, Val) are shifted to the carbonyl level of the PLs in the monolayer, giving a large gain in free energy (Figure 4-12). Additionally, the less hydrophobic residues (Thr, Ala) are shifted upwards towards the polar regions, leading to a further reduction in free energy (Figure 4-12). This combination of large hydrophobic residues shifting to more preferable regions of the membrane while more polar regions are shifted to more polar regions of the membrane drives the

relocalization to LD membranes from monolayers. From these PMFs, we can estimate the free energy stabilization due to all of these residues shifting upwards in the monolayer membrane to be ~40 kcal/mol (Figure 4-13), though this is likely decreased by the insertions of the charged residues, which are in unfavorably positions within the membrane.

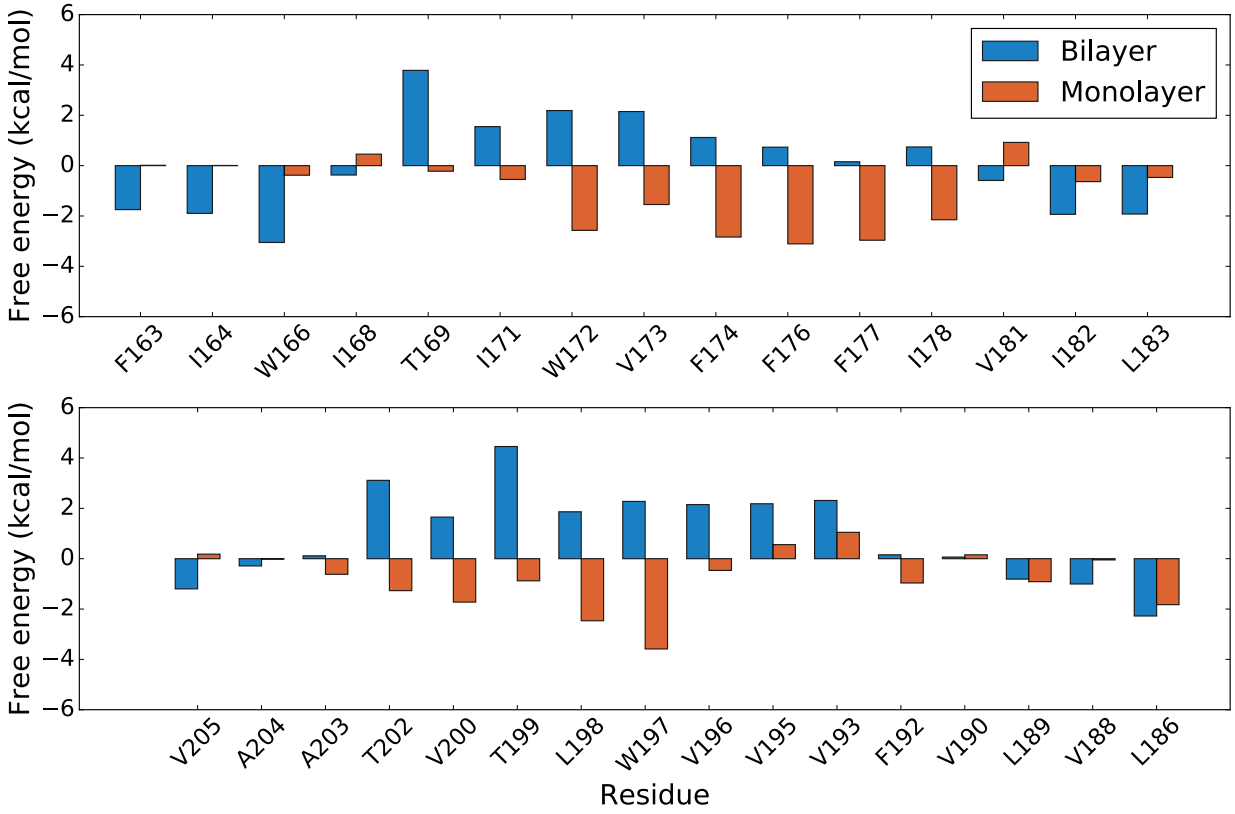

Figure 4-13 Summary of Single Residue Free Energies at Membrane Depths in Bilayer and Monolayer

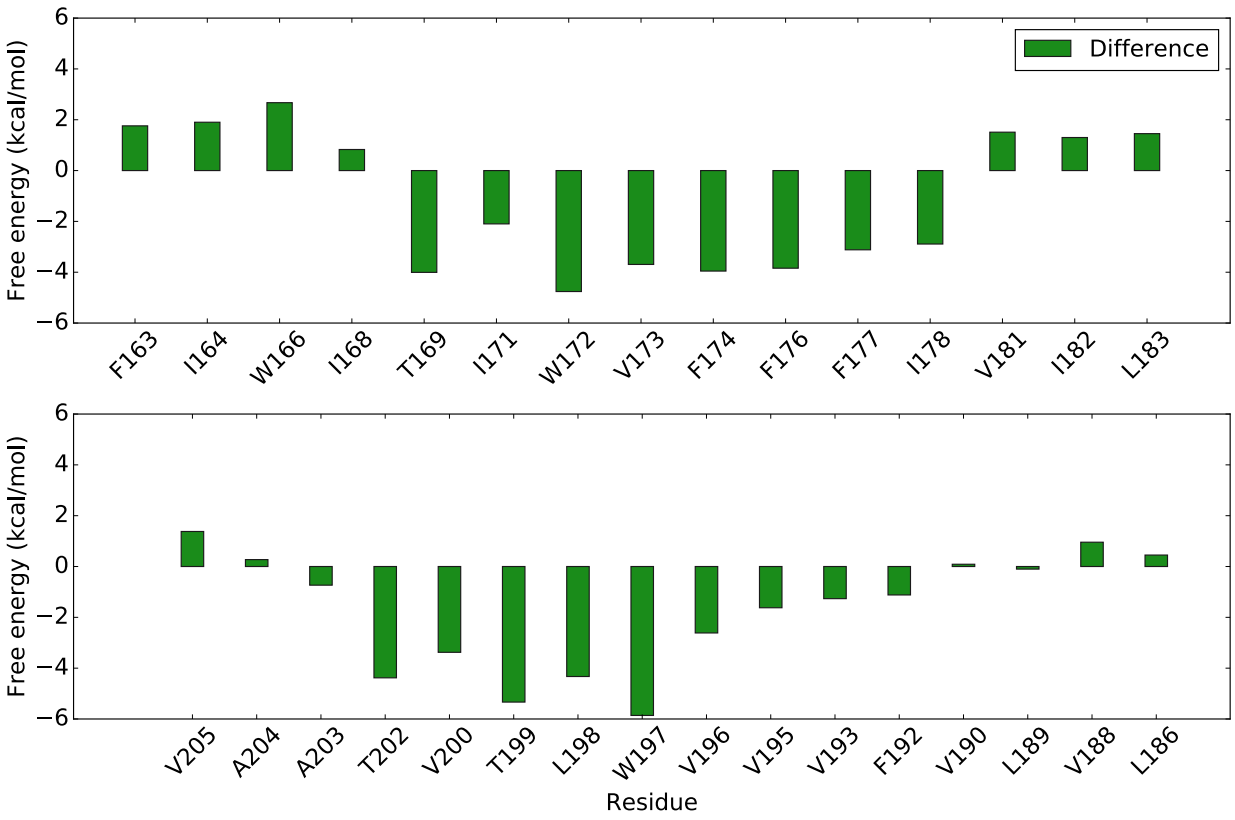

Figure 4-13 **Cont.**

(A) Free energy for each residue in GPAT4 hairpin in both the bilayer (blue) and monolayer (orange). The areas with the large hydrophobic residues show that there is a significant decrease in free energy upon re-localization from the bilayer to monolayer from these residues.
(B) Free energy difference between bilayer and monolayer for each of the above residues. A majority of the residues show a significant decrease in free energy upon re-localization.

Based on these TTMetaD simulations, it would seem that in the bilayer, R179 should also be interacting with the cytosolic leaflet instead of the lumen leaflet, as the stabilization accrued by the hydrophobic regions shifting upwards is quite large. But, R179 and R187 are only 8 residues apart, and the maximum distance separation between the charged nitrogen atoms is 2.5 nm in the monolayer simulations. This would require that the two ARG residues interact with hydrophobic portions of the bilayer, an extremely unfavorable interaction. To verify this effect, we ran

Umbrella Sampling on the W166-A203 distance for the GPAT4 hairpin with R179 mutated to ALA in the bilayer (Figure 4-14). In this calculation, the minimum free energy structure is observed to have a W166-A203 distance of 1.1 nm, which is considerably closer to WT GPAT4 in the monolayer. In this minimum free energy structure, the entire N-terminal helix is shifted upwards, with the structure more closely resembling the WT structure in the monolayer. This explains the decreased targeting of the R179A and R187A mutants (Figure 4-4). Without either of these ARG residues, the corresponding helix is shifted upwards in the bilayer, allowing the hairpin to achieve some of the stabilization in the bilayer that is only possible for the WT hairpin in the monolayer.

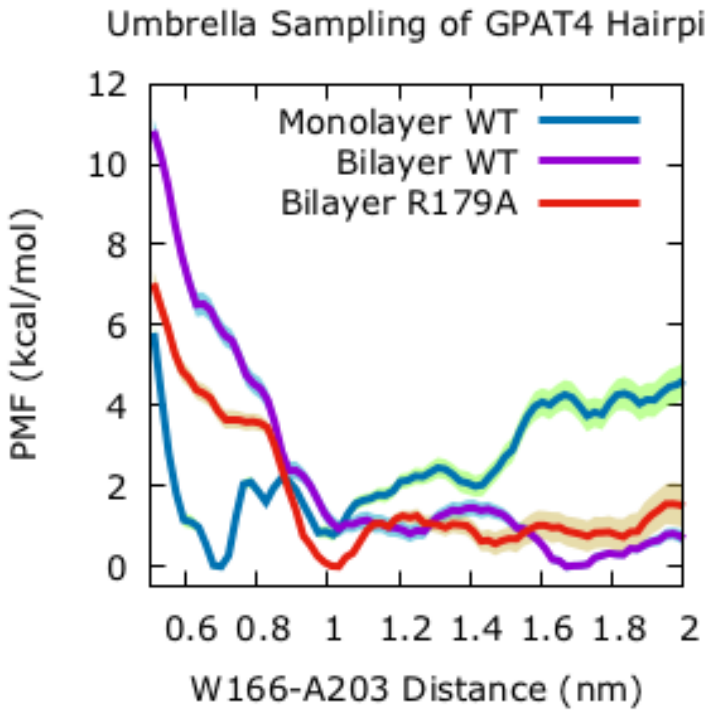

Figure 4-14 Helices of R179A Mutant in Bilayer are More Associated than WT
The PMF for the intra-protein helix association of GPAT4 was calculated along the W166-A203 distance. GPAT4 helices in the R179A are observed to be close together in the monolayer membrane, with a minimum in the PMF at 0.7 nm. The helices of GPAT4 are further separated in the bilayer, and cannot achieve the close distances observed in the monolayer.

4.3 Conclusion

Here we show that the GPAT4 hairpin domain contains a number of residues in specific locations within the sequence that drive conformational change upon relocalization from the ER to LDs. Through a combination of experimental approaches and MD simulations, we have identified key residues that drive GPAT4 targeting to LDs. Mutations of the three charged residues as well as of the Trp residues led to a significant decrease in LD targeting. In the bilayer, the GPAT4 hairpin was observed to prefer unassociated intra-protein helices, while in the monolayer, associated helices are strongly preferred. Furthermore, in the monolayer, the GPAT4 hairpin is significantly shifted towards the membrane-cytosol interface.

From the MD and experimental results shown above, we determine the mechanism of the GPAT4 hairpin targeting to LDs from the ER as follows. First, charged residues on the ends of each of the helices, as well as the hydrophobic regions of the protein, require large hydrophobic residues to reside at the bilayer midplane. The LD monolayer membrane, which does not contain a second polar region for the R179 and R187 to interact with, forces a conformational change upon relocalization to LDs. R179 switches to interact with the cytosolic PL headgroups, while R187 is solvated somewhat successfully by the glycerols of the NLs. This shift of R179 to the cytosolic-LD interface is accompanied by the whole membrane-embedded domain shifting upwards towards the cytosolic leaflet. This is driven by large hydrophobic residues shifting from the PL tail region in the ER to the PL carbonyl region, which is highly preferred. Additionally, the association of the two helices in the hairpin may provide additional stability within the LD membranes.

This suggests a mechanism by which all Class I proteins can target to LDs from the ER. In the ER, hairpin domains will likely contain charged residues that interact at both the cytosolic

and lumen bilayer-water interfaces. These domains should contain long hydrophobic stretches between the charged residues, with large hydrophobic residues localized around the bilayer midplane. Conformational change upon relocalization to LDs allows these large hydrophobic residues to shift towards the glycerol level, providing a large free energy gain. The Alg4 hairpin, which contains many of the same sequence specific features, also has a strong preference for LDs as opposed to the ER. As such, Class I proteins are expected to target to LDs in the same manner as the GPAT4 hairpin.

Understanding why other ER proteins do not target to LDs is important as well. Since the results in (Chapter 3.) suggest that all amino acids prefer to reside in monolayer membranes as opposed to bilayer membranes as long as the membrane insertion depth is equivalent, other aspects of the proteins must be preventing LD targeting. Proteins such as seipin(Wang et al., 2016), which is involved in LD expansion, contain both a cytosolic and luminal domain. These proteins could not target to lipid droplets without pushing the luminal domain through the membrane, an event that is extremely unlikely. Other proteins may also contain a large number of charged residues at the ER-lumen interface. Since there is no polar region for these residues to reside in lipid droplet membranes, these proteins are likely prevented from relocalizing to LDs.

4.4 Methods

General MD Simulation Parameters

All atom simulations were performed using the GROMACS(Abraham et al., 2015) (version 2016) simulation engine with the CHARMM36 lipid(Klauda et al., 2010) and protein(Best et al., 2012; MacKerell et al., 1998) force fields. Biased simulations were also conducted in

GROMACS, with the addition of the PLUMED2(Tribello et al., 2014) plugin. Simulations were integrated with a 2 fs timestep. Non-bonded VDW interactions were cut-off at 1.2 nm and were switched to zero between 1.0 and 1.2 nm. Particle Mesh Ewald(Essmann et al., 1995) algorithm was used to evaluate all electrostatic interactions. Bonds to hydrogen were constrained using the LINCS(Hess, 2008) algorithm. Temperature was maintained at 310 K using the stochastic velocity rescaling thermostat(Bussi et al., 2007) with a coupling time constant of 0.1 ps for simulations that were run in the isothermal-isobaric (NPT) ensemble as well as the canonical ensemble (NVT). In constant pressure simulations, the pressure was maintained semiisotropically using the Parrinello-Rahman(Parrinello and Rahman, 1981) barostat at a pressure of 1.0 bar, a compressibility of 4.5×10^{-5}, and a coupling time constant of 5.0 ps. Coordinates were saved every 10 ps.

GPAT4 Structure generation

The GPAT4 structure was generated using the Rosetta *ab initio* Structure Generation tool(Bradley et al., 2005; Raman et al., 2009; Rohl et al., 2004). Fragment files were created using the Robetta server(Kim et al., 2004; Song et al., 2013). 50,000 structures were generated and the ten structures with the best scores were chosen for analysis. These ten structures contained the same main structural elements (kink at PRO185 and two transmembrane helices on each side of PRO185). The top scoring structure was used for all simulations. We also predicted the structure with MEMSAT-SVM(Jones, 2007; Jones et al., 1994; Nugent and Jones, 2009) and TOPCONS(Tsirigos et al., 2015), which gave similar structures with the same features as Rosetta. The Rosetta generated structure was then solvated in a cubic water box and relaxed with 1 ns of NVT equilibration and 20 ns of NPT equilibration.

GPAT4-Membrane System Setup

GPAT4 was inserted into the bilayer and monolayer membranes using the procedure described in Javanainen(Javanainen and Martinez-Seara, 2016). Briefly, the protein was placed next to the membrane patch, with residue PRO185 at distances of 2, 2.5, and 3.0 nm below the cytosolic leaflet phosphate plane, with the water and ions removed from the system. Restraints were placed on the protein backbone as well as the phosphorous atoms of the lipids. A lateral pressure of 1000 bar was applied to the system, pushing the protein into the membrane. Three lipids were removed from the cytosolic membrane leaflet to maintain equal area of both leaflets. The systems were then relaxed for 2 ns of NPT equilibration. TIP3P water and 0.15 M NaCl was added to the membrane systems. Finally, the membrane-protein systems were equilibrated according to the CHARMM-GUI(Jo et al., 2008) membrane equilibration(Jo et al., 2007; Jo et al., 2009; Lee et al., 2016; Wu et al., 2014) procedure. All 6 systems were then run for 1 μs with coordinates saved every 10 ps.

Umbrella Sampling

Umbrella sampling(Torrie and Valleau, 1977) was conducted on the distance between residues W166 and A203. Harmonic restraints with a force constant of 10^4 kJ/mol/nm were placed on each of 80 windows, spaced every 0.05 nm over a distance range of 0.5 to 4.5 nm. Each window with a distance less than 1.5 nm was run for 90 ns, while every other window was run for 50 ns. The first 10 ns was considered equilibration and was not used for calculating the PMF. Starting structures for each window were generated as follows. Metadynamics(Laio and Parrinello, 2002a) was conducted on the same collective variable as the umbrella sampling, for both the bilayer and monolayer. Hills were deposited with a height of .003 kJ/mol/nm every 1 ps. The simulation length of each of the four metadynamics runs was at least 1 μs. Each of the starting

structures for the umbrella sampling was then chosen from the metadynamics runs, where the $D_{W166\text{-}A203}$ was within 0.02 nm of the equilibrium window distance. The potential of mean force was then calculated using the Grossfield(Grossfield) weighted histogram analysis method(Kumar et al., 1995; Roux, 1995) (WHAM) package with a bin spacing of .02 nm, a tolerance of 10^{-5} kJ/mol/nm. The error in the simulations was estimated by dividing the trajectories into 5 subsamples, calculating the PMF for each subsample, and then determining the standard deviation of the 5 subsamples.

#	Protein (Domain)	Sequence	LD Enrichment (Mean)
1	GPAT4 (Hairpin)	FISWKITSIWVFGFFIRYVILMPLR… …VLVCFVGVVWLTVCTAAVG	6.12
2	GPAT4 (W-V)	FIS<u>V</u>KITSI<u>V</u>VFGFFIRYVILMPLR… …VLVCFVGVV<u>V</u>LTVCTAAVG	2.5
3	GPAT4 (F-V)	FISWKITSIWV<u>V</u>G<u>VV</u>IRYVILMPLR… …VLVC<u>V</u>VGVVWLTVCTAAVG	6.19
4	GPAT4 (Y-V)	FISWKITSIWVFGFFIR<u>V</u>VILMPLR… …VLVCFVGVVWLTVCTAAVG	7.41
5	GPAT4 (LHR-V)	FIS<u>V</u>KITSI<u>V</u>V<u>V</u>G<u>VV</u>IR<u>V</u>VILMPLR… …VLVC<u>V</u>VGVV<u>V</u>LTVCTAAVG	1.39
6	GPAT4 (KRR-AAA)	FISW<u>A</u>ITSIWVFGFFI<u>A</u>YVILMPL<u>A</u>… …VLVCFVGVVWLTVCTAAVG	2.83

Table 4-1 Table of Hairpin Sequences used in this Manuscript
Table of hairpin sequences used in this manuscript, with their respective LD enrichment. LD enrichment is a measure of the amount of protein on LDs, as compared to the ER and cytosol. Mutated residues are underlined in the sequences of mutants.

7	GPAT4 (K167A)	FISWAITSIWVFGFFIRYVILMPLR… …VLVCFVGVVWLTVCTAAVG	5.08
8	GPAT4 (R179A)	FISWKITSIWVFGFFIAYVILMPLR… …VLVCFVGVVWLTVCTAAVG	3.37
9	GPAT4 (R187A)	FISWKITSIWVFGFFIRYVILMPLA… …VLVCFVGVVWLTVCTAAVG	5.37
10	GPAT4 (Scrambled)	FISLGFVTWLVRTCWSVIFVLMPLR… …VGVFIKYTIWCVAIVFAVG	1.76
11	GPAT4 (Artificial)	WSGYLTGIVAFFLAIFAVLSLGPMIW… …ICAFIVFLCVAMITVWAG	1.26
12	AGPAT3	LVNFVCWAVFSLSCIFYYVITSLLAANWTAFIT ALSVLGLFYWLM	1.31
13	DGAT2	ILVTAFFTSMLLILLSVSFLLVAGSL… …IYGGLLVRSLMVTYLAYVFVH	1.37
14	Alg4	QSWLSSIFTSLWALLWSCYLVWRDRPQ… …LILCNGPGTCVPFCYAAYLWRLLGRLPS	8.35
15	LysoPA	EIDSHIEVAKIYVLTVLLLPIRVV… …GCVLSLISAWMFACIGLYGMT	1.87
16	Lunapark	STEAVLEGLQTQIQALEKYMINT… …EERKRRFVTNFVGFTIGAYIV… …GFGLWWYFYFPPTMQECFM… …YLVPLLLFPIVIIFLRRLFTWY… …FQRKLNKNGDKLTRLKEDKRK… …ILEQVMDKETYKVAVNLLERFGD	2.92
17	SelT-like	DPPGLNYYLSKMIFALKIIIIVSVVS… …AVSPFTFLGNTPSWWSHMQANK… …IYACMMIFFLGNMLEAQLISSGA	1.25

Table 4-1 Cont.

4.5 Acknowledgements

We thank Jesper Madsen and Zack Jarin for help with the simulations, and members of the Voth group for comments on the manuscript. The simulations in this work used the Extreme Science and Engineering Discovery Environment (XSEDE), which is supported by the National Science Foundation grant number ACI-1548562. Specifically, it used the Bridges system at the Pittsburgh Supercomputing Center (PSC) through allocation number TG-MCA94P017. This work was also completed in part with resources provided by the University of Chicago Research Computing Center (RCC).

Chapter 5. Endophilin H0 Folding on Bilayer Membranes

5.1 Introduction

Curvature generation in membranes can take place through several mechanisms, including protein scaffolding, amphipathic insertion and protein crowding (Simunovic et al., 2015). In the case of BAR (Bin/amphiphysin/Rvs) domain-containing proteins, it has been shown that different curvature stabilizing domains within the protein each stabilize curvature in a different fashion (Snead et al., 2018). The BAR domain itself stabilizes curvature through its banana shape, typically containing many positive charged residues on the membrane-interacting face to bind to the negatively charged phospholipids (Frost et al., 2009; McMahon and Gallop, 2005; Mim and Unger, 2012). BAR proteins that contain intrinsically disordered domains can also generate positive curvature on the membrane due to protein crowding on the surface of the membrane (Snead et al., 2018).

Amphipathic helices (AH), a common motif on BAR domains, are known to generate curvature through wedging, where the AH insert at the membrane-water interface, increasing the surface area at the interface, generating and stabilizing curvature (Boucrot et al., 2012; Cui et al., 2011; Cui et al., 2013). Large, hydrophobic residues within the AH have been shown to read out the packing defects in the membrane (Vamparys et al., 2013; Vanni et al., 2013), which are created when hydrophobic core is exposed in the membrane, and fold inside the membrane. However, the exact process of helix formation (and the immersion process) in vesicles and tubules are not well known (Ambroso et al., 2014; Voth, 2013). Time-evolution data from double

electron-electron resonance (DEER) experiments indicate that AH immersion in tubules has a timescales on the order of microseconds (Ambroso et al., 2014).

Here we simulate the buried N-terminal helix from rat endophilin A1 protein in a lipid bilayer, in order to determine bilayer protein interactions that lead to the AH insertion in the membrane (Gallop et al., 2006; Jao et al., 2010). Though large defects favor helix folding and insertion, recent studies (Cui et al., 2011; Vamparys et al., 2013; Vanni et al., 2013) have revealed that large defects are not natural in self-aggregating lipid systems and the defect size distribution depend largely on the curvature, following an exponential law. Since average defect size is only a tiny fraction of the size of the folded helix, it is hypothesized that the defects must nucleate dynamically along with the folding of the AH and the restructuring of the defects is coupled with the hydrophobic sensing and helix folding/insertion process (Cui et al., 2011).

With the long microseconds simulations, we show the difficulties in simulating the folding process of AH on membranes. With multiple simulations together comprising over 50 μs of simulation, two partial folding events were observed. Folding was observed around the residue that was inserted first into the membrane, though the residues closest to the inserted residue displayed difficulty in folding. The data suggests that successful H0 folding will occur directionally from one end of the helix to the other to prevent kinks from occurring at the center.

5.2 Results and Discussion

To mimic the lipid packing defect distributions observed in curved membranes, where H0 is known to insert and fold (Cui et al., 2011), lipids were removed from one membrane leaflet. Upon the removal of 12 lipids from one leaflet, the membrane was observed to maintain the same lipid packing defect distribution as a highly curved membrane. We set out to determine

whether specific insertions of hydrophobic residues are more likely to result in a folded helix. Therefore, a single hydrophobic residue on the endophilin H0 was then inserted into a large packing defect on the membrane surface. Hydrophobic residues on amphipathic helices are known to first insert into the membrane before folding occurs (Vanni et al., 2013) and beginning the simulations after this mechanistic step simply decreases the simulation time necessary for folding. Two replicas were run with each V3, L6, and V21 inserted into the membrane. Three replicas were run with F10 inserted, as F residues have been shown to more frequently insert first into the membrane. For the folding simulations, we characterize the folding using two collective variables: 1) alpha-beta similarity, a measure of whether the phi- and psi-dihedral angles are in a helix conformation, and 2) backbone hydrogen-bonding, which is a sum of the number of backbone hydrogen bonds occurring in the protein.

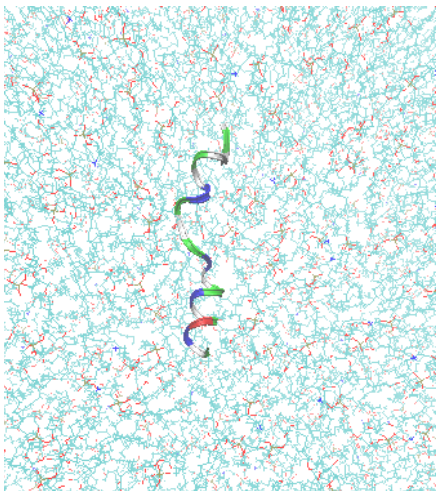

Figure 5-1 Folding of Endophilin H0 on a Membrane

Within the first 2 μs of simulation, no folding was observed in 6 out of the 9 replicas (Figure 5-2). In one simulation where F10 was inserted, folding began on the C-terminus and proceeded until F10 and then did not proceed any more. In a second simulation where F10 was inserted,

folding proceeded from both the N- and C-terminus, halting as it approached the residues near F10. In another simulation where V21 was inserted, the peptide popped out of the membrane, L6 inserted into the membrane, which afterward began to fold from the N-terminus. In this simulation, 16 out of 22 residues folded.

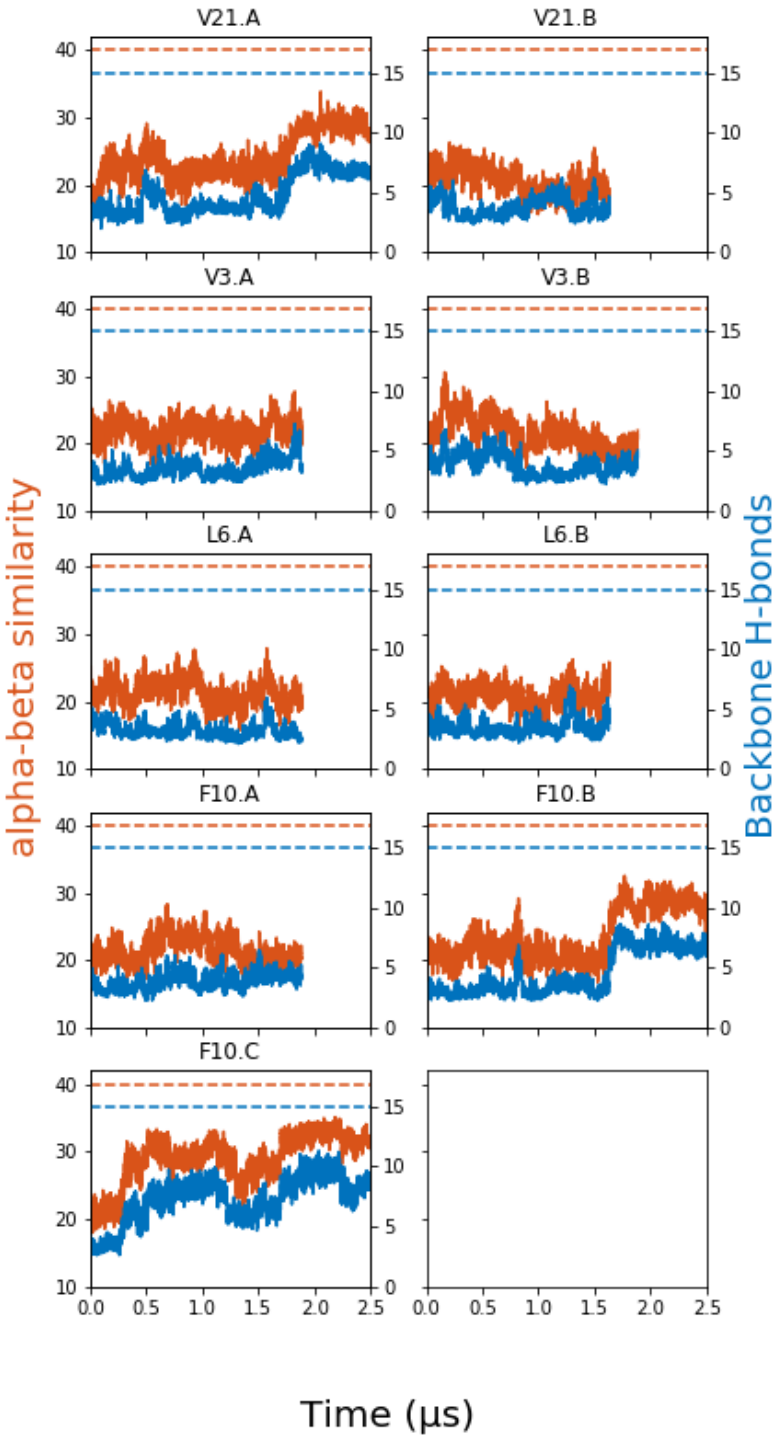

Figure 5-2 Endophilin H0 exhibits limited folding with 2 μs of simulation
The CVs alpha-beta similarity (orange) and backbone hydrogen bonding (blue) plotted over time for the folding simulations. Simulations are denoted by the residue that was first inserted (e.g. V21) into the membrane, along with the replica (A,B,C). The folded values for the CVs are denoted with a dashed line.

Two of these partially successful simulations were further extended to observe whether additional folding would occur Figure 5-3. With the initial insertion of V21, a stable partially folded state is observed within 5 μs of simulation. For the initial insertion of F10, a partially folded conformation is observed within the first μs of simulation. But, over 20 μs of simulation is required for H0 to leave this state. Protein folding in water is known to contain a number of frustrated states along the folding pathway (Lindorff-Larsen et al.). Folding on the membrane is likely frustrated even further, due to the slower diffusion of phospholipids, compared to water.

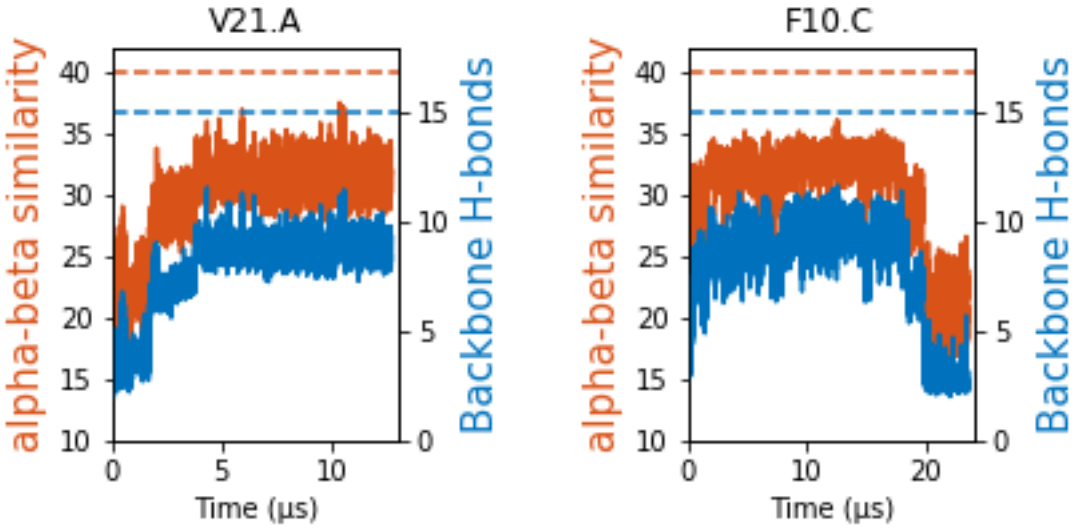

Figure 5-3 Extended Simulations of H0 do not Achieve Full Folding
The simulations with V21 and F10 initially inserted that demonstrated partial folding were extended past 2 μs of simulation time. The V21 simulation continues folding and achieves a stable partially folded state. The H0 with F10 inserted stayed partially folded for 17 μs, after which unfolding occurred.

From these simulations, we were able to learn a number of details about the folding process on the membrane. First, insertions of larger hydrophobic residues into the membrane, including PHE and LEU, promote folding. But insertions of these residues is not enough to drive folding,

as folding did not occur in a number of simulations where these were inserted. Second, once folding begins, it will proceed fairly quickly, within 2 μs, to a mostly folded state. This mostly folded structure is stabilized compared to the unfolded structure. But, there appears to be an additional barrier to folding which cannot be overcome within μs of simulation.

5.3 Methods

System Setup

Bilayer membranes were built using the CHARMM-GUI (Jo et al., 2007; Jo et al., 2008; Jo et al., 2009; Lee et al., 2016; Wu et al., 2014) web server. The CHARMM36 protein (Best et al., 2012; MacKerell et al., 1998) and lipid (Klauda et al., 2010) force fields were used for all simulations. Bilayer membranes were built with 100 DOPG and 50 DOPE lipid molecules per leaflet. 12 lipids were removed from one leaflet to mimic the defect distribution in curved membranes. The endophilin H0 (sequence: MSVAGLKKQFHKATQKVSEKVG) was simulated for 10 ns at 400K to unfold the helix and then simulated at 310K for 10 ns to generate an ensemble of configurations to begin the folding simulations. 9 configurations were chosen, where one of the hydrophobic residues (V21, V3, L6, F10) was orientated in opposite directions of the rest of the helix. Each configuration was inserted into a large packing defect on the membrane, such that it was the only residue in the hydrophobic region, with the rest of the protein in solution, using VMD (Humphrey et al., 1996). Each system was then re-solvated and ionized (150 mM NaCl) using VMD.

Simulations Using Anton

Simulations were run on the ANTON (Shaw et al., 2009) supercomputer. Simulations were integrated using the multigrator (Lippert et al., 2013) with a 2-fs timestep using RESPA

(Tuckerman et al., 1992), where long range electrostatic interactions were evaluated every three timesteps. VDW interactions were switched to zero between 1.0 and 1.2 nm, and Particle Mesh Ewald (Essmann et al., 1995) was used to evaluate electrostatic interactions. All bonds to hydrogen were constrained using the SHAKE algorithm (Ryckaert et al., 1977). The Nose-Hoover thermostat (Hoover, 1985) was used to maintain temperature at 310 K with a coupling time constant of 1.0 ps. The MTK barostat (Martyna et al., 1994) maintained a pressure of 1.0 atm semiisotropically.

5.4 Acknowledgements

Anton computer time was provided by the Pittsburgh Supercomputing Center (PSC) through grant *R01GM116961* from the National Institutes of Health. The Anton machine at PSC was generously made available by D.E. Shaw Research. The MD simulations were also completed in part with resources provided by the University of Chicago Research Computing Center.

Chapter 6. A Bottom Up Approach for Multi-Configuration Coarse Grained Molecular Dynamics

6.1 Abstract

Standard coarse-grained modeling techniques have difficulty capturing multiple configurations of protein systems. Here we present a method for creating accurate CG models with multiple configurations using empirical valence bond theory. Individual CG models are created to capture the individual states, and the coupling between the two states is determined from the all-atom potential of mean force. We show that the multi-configuration coarse-graining (MCCG) method accurately captures the transition state as well as the free energy between the two states. We test the method on the folding of dodecaalanine as well as the amphipathic helix of endophilin.

6.2 Introduction

Cellular systems are inherently multiscale, involving the interplay of many length scales and time scales working in concert. As a result, the theoretical methods used to understand these systems must be able to take into account this multiscale nature. Although molecular dynamics (MD) simulations can be used to successfully probe bio-molecular processes and interactions in ways that can complement experimental results (Schlick et al., 2011), standard MD methods are limited to length and time scales that may be unable to accurately characterize biological phenomena. These systems require the use of multiscale MD methods (Marrink and Tieleman, 2013; Riniker et al., 2012), where low resolution, or coarse grained (CG), models of biological molecules are developed to reduce the computational cost of such simulations; all while maintaining the fundamental physics and chemistry underlying the biological processes (Noid,

2013). The use of low-resolution CG models can be used to probe important biological processes such as protein-protein interactions (Grime and Voth, 2012; Langowski et al., 2013; Pak et al., 2017), membrane remodeling by proteins (Arkhipov et al., 2008; Braun et al., 2012; Fuhrmans and Marrink, 2012; Simunovic et al., 2016; Simunovic et al., 2013; Simunovic and Voth, 2015; Simunovic et al., 2015; Su et al., 2018), and large-scale protein conformational changes (Elofsson et al., 2012; Kalli et al., 2016; Lelimousin et al., 2016; Yefimov et al., 2008).

Current CG models are often unable to accurately reproduce conformational change of proteins (Marrink and Tieleman, 2013; Riniker et al., 2012), and are typically best suited to reproduce a single conformation of a protein. However, even CG models that are able to capture multiple protein conformations are still unable to reproduce neither the free energy difference between the two states nor the transition barrier (Calero-Rubio et al., 2016; Rudzinski and Bereau, 2016). This has been demonstrated for CG models that were parameterized with a top down approach, incorporating information from experiment, or a bottom-up approach, where high frequency motions in higher resolution all-atom (AA) simulations are integrated out to generate smoother, but less detailed interaction potentials. The popular MARTINI protein force field (de Jong et al., 2013; Monticelli et al., 2008), a top-down CG model, requires an elastic network on the peptide backbone to maintain secondary structure and is therefore restrained to the native state (Marrink and Tieleman, 2013; Periole et al., 2009). Bottom up CG approaches, including relative entropy minimization (REM) (Shell, 2008) and multiscale coarse-graining (MS-CG) (Izvekov and Voth, 2005; Noid et al., 2008a; Noid et al., 2008b) can at best capture portions of multiple conformations, but less accurately capture the free energy difference between the states and the transition barrier (Carmichael and Shell, 2012; Rudzinski and Noid, 2015; Thorpe et al., 2008). This deficiency of current CG modeling techniques prevents the

study of complex, multiscale biophysical phenomena, including for example, actin polymerization, where the ATP hydrolysis within actin as well as actin conformational change drive polymerization and depolymerization (Pollard et al., 2000) .

Much of the previous work on multi-configuration CG modeling has been focused on developing fine-grained, Cα elastic network models of proteins that can switch between two or more equilibrium states (Best et al., 2005; Chu and Voth, 2007; de Marco and Várnai, 2009; Maragakis and Karplus, 2005; Okazaki et al., 2006; Zheng et al., 2007). These methods treat the individual equilibrium configurations as discrete states and use an empirical valance bond method (EVB) like approach to couple the discrete states while also providing the smooth saddle point between the states. The benefit of this approach is that the CG model can sample configurations, or states, corresponding to very different structures. But, switching between structures in these simulations is not parameterized in a multiscale manner that accurately reproduces key features in the potential of mean force (PMF), such as the transition barrier and the free energy difference between the states.

In this work, we introduce a new multi-configuration coarse graining (MCCG) method that can both switch between CG models during the course of a MD simulation and directly takes into account the AA PMF to couple the individual CG models. The multiscale approach results in CG simulations that can reproduce the AA PMF, but with much fewer degrees of freedom than the AA case. In the MCCG method presented here, an EVB-like approach is used, where the diagonal elements of the Hamiltonian represent the potential energy surface for each of the independently developed CG models. MCCG takes advantage of the strength of CG models to accurately reproduce individual protein conformations. Each of these models can represent the system in a different state, e.g. folded or unfolded, open or closed, in membrane or in solution.

The off-diagonals elements represent the thermodynamic coupling between the CG states. The coupling is treated as function of CG CVs that describe the transition between states and is directly calculated from the AA PMF in a way that compensates for the differences between the CG potential energy surfaces and the AA PMF. This results in a CG simulation that can reproduce all of the features of the AA PMF, including the saddle point barrier, in terms of CG CVs that describe the transition between the CG structural states.

6.3 Theory and Methods

6.3.1 Theory

To develop CG models that can adopt multiple configurations, we first treat the individual structures as discrete states with completely separate force fields and potential energy surfaces, labeled $V_{11}(\boldsymbol{R}^N)$ and $V_{22}(\boldsymbol{R}^N)$. Here, we are limiting ourselves to the case where only two CG structural models are considered. Although our system is not a quantum mechanical system, treating the individual CG structures as discrete thermodynamic states allows us to conveniently describe the system using an eigenvalue problem, as in the case of electron transfer.(Marcus, 1964) By using the following characteristic equation, the potential energy surface, E, can be created that includes a smooth saddle point between the potential energy surfaces of the individual CG models, $V_{11}(\boldsymbol{R}^N)$ and $V_{22}(\boldsymbol{R}^N)$:

$$\begin{pmatrix} V_{11}(\boldsymbol{R}^N) & V_{12}(\boldsymbol{R}^N) \\ V_{12}(\boldsymbol{R}^N) & V_{22}(\boldsymbol{R}^N) \end{pmatrix} \begin{pmatrix} c_1 \\ c_2 \end{pmatrix} = E \begin{pmatrix} c_1 \\ c_1 \end{pmatrix} \tag{6.1}$$

where $\boldsymbol{R}^N$ is the CG coordinates, $V_{11}(\boldsymbol{R}^N)$ and $V_{22}(\boldsymbol{R}^N)$ are the potential energy surfaces of the discrete thermodynamic states, $V_{12}(\boldsymbol{R}^N)$ is the thermodynamic coupling between the two states, E is the potential energy surface of the total system, and c_1 and c_2 are the components of the eigenvector. In the MCCG model, the $V_{11}(\boldsymbol{R}^N)$ and $V_{22}(\boldsymbol{R}^N)$ terms are determined by the force fields describing the individual states.

If there is a nontrivial solution to the characteristic equation above, then the secular equation can be solved for the lowest energy eigenvalue:

$$\begin{vmatrix} V_{11}(\boldsymbol{R}^N) - E & V_{12}(\boldsymbol{R}^N) \\ V_{12}(\boldsymbol{R}^N) & V_{22}(\boldsymbol{R}^N) - E \end{vmatrix} = 0 \tag{6.2}$$

resulting in the following expression for the potential energy surface:

$$E = \frac{1}{2}\left[V_{11}(\boldsymbol{R}^N) + V_{22}(\boldsymbol{R}^N)\right] - \left[\left(\frac{V_{11}(\boldsymbol{R}^N) - V_{22}(\boldsymbol{R}^N)}{2}\right)^2 + V_{12}(\boldsymbol{R}^N)^2\right]^{1/2} \tag{6.3}$$

Previously developed multistate MD methods have either treated the off-diagonal coupling term, $V_{12}(\boldsymbol{R}^N)$, as either a constant (Best et al., 2005; de Marco and Várnai, 2009; Maragakis and Karplus, 2005; Okazaki et al., 2006) or have used a second order expansion around the saddle point to approximate the coupling (Chang and Miller, 1990; Chu and Voth, 2007).

Our goal in this work is to develop a method for determining $V_{12}(\boldsymbol{R}^N)$ using parameters calculable from AA simulations. This will allow the CG system to reproduce the PMF calculated for the AA system. To this end, we can solve the potential energy solution in eq. (6.3) for the off-

diagonal coupling term, $V_{12}(\boldsymbol{R}^N)$, in terms of both the individual states and the total potential energy surface:

$$V_{12}(\boldsymbol{R}^N)^2 = \left[V_{11}(\boldsymbol{R}^N) - E\right]\left[V_{22}(\boldsymbol{R}^N) - E\right] \tag{6.4}$$

To derive an expression for $V_{12}(\boldsymbol{R}^N)$ in which we can easily calculate the relevant terms, we make two assumptions. First, similar to the CG method of Boltzmann Inversion (BI), we make the assumption that the potential energy surface of the CG system can be approximated by the true many-body PMF, $F(\boldsymbol{R}^N)$. Here we will use the AA PMF in place of the true system PMF, but this may also be determined using force-pulling experiments or constructed *ad hoc*. Second, we assume that we can describe the process of transitioning from state $V_{11}(\boldsymbol{R}^N)$ to state $V_{22}(\boldsymbol{R}^N)$ with a single, or collection of, collective variables $\boldsymbol{Q}$. The off-diagonal coupling can now be rewritten in terms of the PMFs of the CG diabatic states, $F_{11}(\boldsymbol{Q})$ and $F_{22}(\boldsymbol{Q})$, as well as the AA PMF, $F_{AA}(\boldsymbol{Q})$

$$V_{12}(\boldsymbol{Q})^2 = \left[F_{11}(\boldsymbol{Q}) - F_{AA}(\boldsymbol{Q})\right]\left[F_{22}(\boldsymbol{Q}) - F_{AA}(\boldsymbol{Q})\right]. \tag{6.5}$$

For $F_{AA}(\boldsymbol{Q})$, we assume that there is a function that maps the AA coordinates onto the CG CV, $\boldsymbol{Q}$. By including the off-diagonal coupling between states in a way that is determined directly from the AA PMF, the potential energy surface of this MCCG model can exactly reproduce the AA PMF in terms of CG CVs.

If the coupling term is correct, the MCCG PMF will match the AA PMF. But, as in the case of BI, entropic contributions from the AA system have not been accounted for in the CG

potential energy terms. To account for this, $V_{12}(\boldsymbol{Q})$ must be iteratively updated (as in Iterative Boltzmann Inversion) to create agreement between the AA and CG PMF. The coupling term $V_{12}(\boldsymbol{Q})$ is iteratively updated to improve the resulting MCCG PMF by adding the difference between the AA PMF $F_{AA}(\boldsymbol{Q})$ and the MCCG PMF $F^{i}_{MCCG}(\boldsymbol{Q})$ to the coupling term:

$$V_{12}^{i+1}(\boldsymbol{Q}) = V_{12}^{i}(\boldsymbol{Q}) + \alpha(F_{AA}(\boldsymbol{Q}) - F^{i}_{MCCG}(\boldsymbol{Q})) \tag{6.6}$$

where α is a tuning parameter to ensure convergence. Successive updates to the off-diagonal coupling term will drive the MCCG PMF to approach the AA PMF.

6.3.2 Simulation Details

AA Simulations

All Atom (AA) simulations were performed with the GROMACS (version 5) simulation suite (Abraham et al., 2015) using the CHARMM36 force field (Best et al., 2012). Simulations were integrated with a 2 fs timestep. Non-bonded VDW interactions were switched to zero between 1.0 and 1.2 nm. Electrostatic interactions were evaluated using Particle Mesh Ewald (Essmann et al., 1995). Bonds to hydrogen were constrained using the LINCS algorithm (Hess, 2008). Temperature was maintained at 310 K using the stochastic velocity rescaling thermostat (Bussi et al., 2007) with a coupling time constant of 0.1 ps. The pressure was maintained isotropically in constant pressure simulations using the Parrinello-Rahman barostat (Parrinello and Rahman, 1981) at a pressure of 1.0 bar, a compressibility of 4.5×10^{-5}, and a coupling time constant of 2.0 ps. Coordinates were saved every 1 ps.

AA System Initialization and Equilibration: The endophilin H0 amphipathic helix (Sequence: MSVAGLKKQFHKATQKVSEKVG) and the capped alanine 12-mer were each initialized in a

linear configuration using the Molefacture plugin in VMD (Humphrey et al., 1996). H0 and dodecaalanine were solvated using VMD in a TIP3P water box with a side length of 6.0 and 4.8 nm, respectively, and ionized with 150 mM NaCl. The two peptides were then energy-minimized using the steepest descent algorithm to a maximum force of 1000 kJ mol-1 nm-1; the systems converged within 500 steps. The peptides were then equilibrated for 1 ns in the isothermal-isobaric ensemble (NPT).

AA production simulations: Dodecaalanine (ALA-AA) was simulated for 1 μs in the canonical ensemble (NVT) to adequately sample the folding/unfolding process. Free energy surfaces and CG models were obtained from the single, 1 μs simulation. H0 was simulated (H0-AA) using temperature replica-exchange molecular dynamics(Sugita and Okamoto, 1999) (T-REMD) with 72 temperature windows exponentially distributed from 310 K to 565 K. Each temperature replica was first equilibrated at the respective temperature for 100 ps. Each temperature replica was then simulated for 100 ns, with exchanges occurring every 100 steps. The average exchange probability across all replicas was 25%. Free energy surfaces and CG models were obtained from the lowest temperature replica.

CG Simulations: Coarse-grain (CG) simulations were carried out using the LAMMPS simulation package (Plimpton, 1995). Simulations were integrated with a 5.0 fs timestep. Temperature was maintained using the Langevin thermostat (Schneider and Stoll, 1978) with a damping coefficient of 500 fs. Coordinates were saved every 200 timesteps. MCCG simulations were performed using a newly designed plugin for LAMMPS simulation package (https://github.com/mocohen/USER-MCCG), which interfaces with the PLUMED2 plugin.(Tribello et al., 2014) MCCG simulation parameters were the same as the CG simulations.

CG Models

Dodecaalanine*:* Four solvent free CG models of Dodecaalanine were constructed from the 1 μs AA simulation. Each alanine residue was represented by a single bead corresponding to the α carbon, for a total of 12 CG beads for the whole peptide. Two methods for creating CG models were used: heterogeneous elastic networks (Lyman et al., 2008) (HENM) and Boltzmann Inversion (BI). HENM models of polyalanine were created using the full trajectory (ALA-HENM) as well as for only the folded configurations (ALA-HENM-F). HENM models were constructed using a cutoff of 1.5 nm. BI models of polyalanine were created using the full trajectory (ALA-BI) as well as for only the unfolded configurations (ALA-BI-U), configurations with a helicity (Q_{hel}) less than 0.2. Each bead in the BI model was treated equivalently - models were constructed with a single bond, angle, dihedral, and non-bonded interaction. Each CG model of dodecaalanine was simulated for 4 billion timesteps to obtain the free energy surfaces.

H0: Two solvent free CG models of h0 were constructed from the lowest temperature replica of the AA T-REMD simulation. Each residue was represented by a single bead corresponding to the Cα carbon, for a total of 22 CG beads for the whole peptide. An HENM model of h0 was constructed using only the folded configurations (H0-HENM-F). The HENM model was constructed using a cutoff of 1.5 nm. A BI model of h0 was created using only the unfolded configurations (H0-BI-U). Each bead in the BI model was treated equivalently – models were constructed with a single bonded, angular, dihedral, and non-bonded interaction. Each CG model of h0 was simulated for 4 billion timesteps to obtain the free energy surfaces.

MCCG Models: MCCG models were constructed for dodecaalanine (ALA-MCCG) and h0 (H0-MCCG) using the folded HENM and unfolded BI CG models for the two states. For the iterative procedure, α was set to be 1.

6.4 Results and Discussion

In this study, we demonstrate the ability of a coupled two-state CG system to capture the folding and unfolding of two different peptides: an alanine 12-mer and endophilin h0.

6.4.1 Dodecaalanine

Dodecaalanine was chosen as the first system to study because it has been used in previous studies, which have attempted to capture the folding and unfolding process of peptides (Carmichael and Shell, 2012; Rudzinski and Noid, 2015). We first simulated dodecaalanine for 1 μs using AA MD. This fine-grained simulation sampled folded, partially folded, globular, and extended configurations. The free energy surface (Figure 6-1) along the collective variables (CVs) helicity (Q_{hel}) and radius of gyration (R_g) shows a large free energy minimum in the unfolded configuration (Q_{hel}< 0.2) as well as a few small free energy minima in the helical configurations (Q_{hel}> 0.8). These two CVs have been previously (Rudzinski and Noid, 2015) used to characterize the different conformations explored by dodecaalanine.

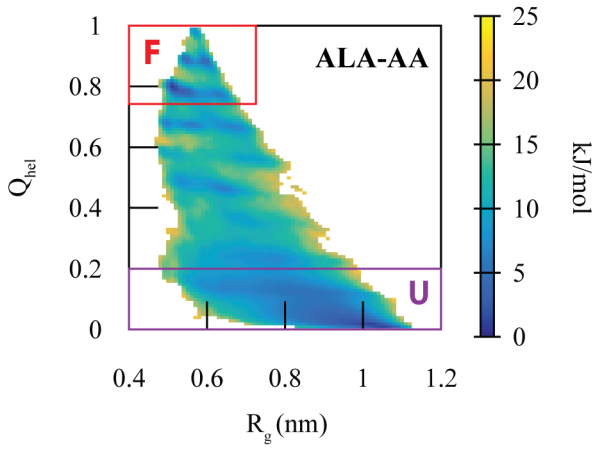

Figure 6-1 2D potential of mean force for the AA dodecaalanine (ALA-AA) system.
The PMF is plotted with mapped coordinates as a function of helicity (Q_{hel}) and radius of gyration (R_g). The folded state is denoted in the red square (F), and the unfolded state (U) in purple.

We chose a Cα mapping – one CG site per residue at the Cα position – for each CG. A Cα CG mapping is able to characterize the difference between an unfolded or folded helix (Tozzini et al., 2006). Using the Cα CG mapping, we developed two simple CG models to try to capture the folding and unfolding of the peptide using the AA trajectories. Both the Boltzmann Inversion (ALA-BI) and Heterogeneous Elastic Network (ALA-HENM) models developed from the AA trajectory of dodecaalanine failed to capture this transition, as seen in the 2D PMF (Figure 6-2). ALA-BI reproduces only portions of the folded configuration and is quite sticky – it stabilizes structures with small radius of gyration ($R_g < 0.4$), configurations that are not sampled in the AA simulation. ALA-HENM samples the unfolded configuration as well as a large number of high-energy states that are not sampled in the AA simulation. Previous studies by Carmichael and

Shell(Carmichael and Shell, 2012), as well as Rudzinski and Noid, (Rudzinski and Noid, 2015) have demonstrated the inability of more complicated CG methods to accurately capture both the folded and unfolded configurations of alanine polymers using the REM, iterative generalized Yvon-Born-Green, (Cho and Chu, 2009; Lu et al., 2013) and MS-CG techniques.

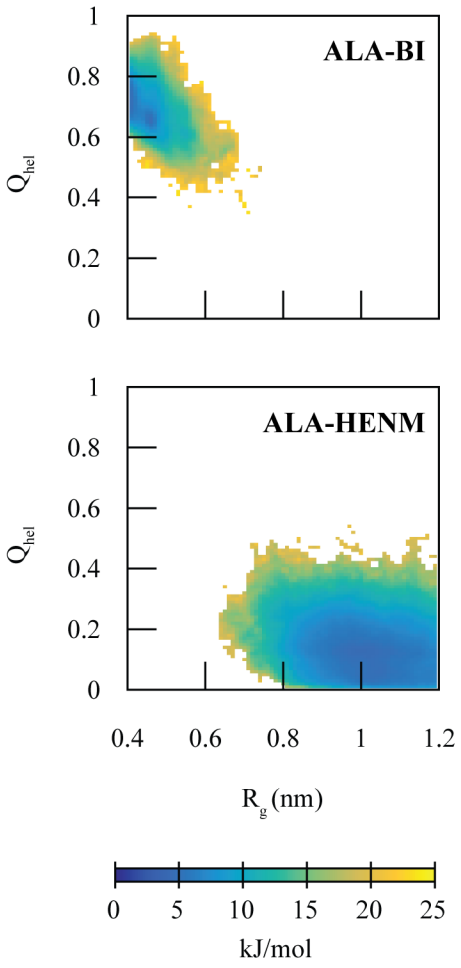

Figure 6-2 2D potentials of mean force of dodecalalanine for the BI (ALA-BI) and hENM (ALA-HENM) CG models.

The PMF is plotted with mapped coordinates as a function of helicity (Q_{hel}) and radius of gyration (R_g). ALA-BI and ALA-HENM both cannot reproduce the AA mapped PMF, and do not even sample portions of the AA mapped PMF well.

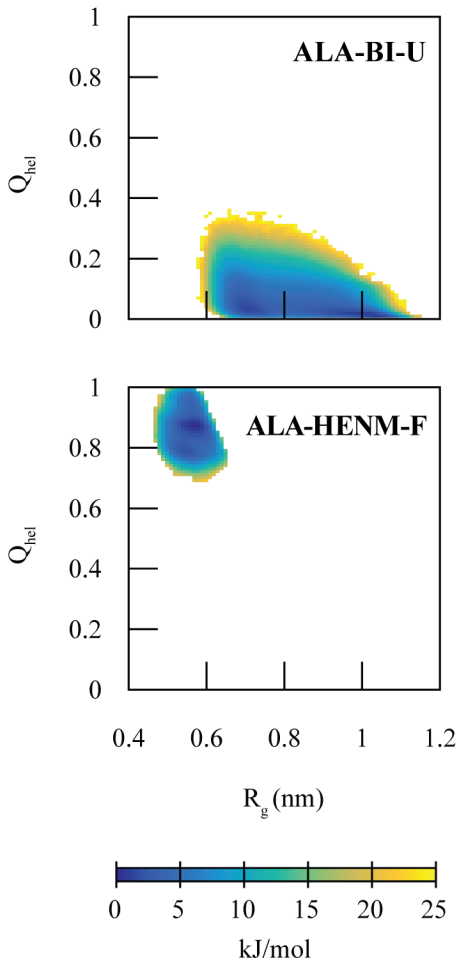

Figure 6-3 2D potentials of mean force of dodecalalanine for the unfolded BI (ALA-BI-U) and folded hENM (ALA-HENM-F) CG models.

The PMF is plotted with mapped coordinates as a function of helicity (Q_{hel}) and radius of gyration (R_g). ALA-BI-U reproduces the unfolded portion of the AA PMF, and ALA-HENM reproduces the folded portion of the AA PMF.

We next parameterized separate CG models to model the folded and unfolded configurations. A BI CG model parameterized solely from AA coordinates of the unfolded configuration (ALA-BI-U) reproduced the unfolded portion of the 2D PMF, and a heterogeneous Elastic Network CG model parameterized solely from AA coordinates of the folded configuration (ALA-HENM-F) reproduced the folded portion of the 2D PMF (Figure 6-3). While these simple CG models reproduce the general shape of the unfolded and unfolded areas of the PMF, they do not contain some of the local minima observed in the AA PMF. This is to be expected, as CG models generally smooth out the PMF. Additionally, more features could be obtained in the individual CG models if more sophisticated CG modeling techniques, such as MS-CG and REM, are used to build the diabatic states.

Using these CG models as the diabatic states, and the AA and CG 2D PMFs to calculate the coupling, we constructed an MCCG model of dodecalanine (ALA-MCCG). The coupling term $V_{12}(\boldsymbol{Q})$ was mostly localized to the transition region between the two states (Figure 6-4). Due to the large transition region, the coupling is required to operate over a large portion of conformational space. The resulting 2D PMF from simulations of ALA-MCCG show sampling in both the folded and unfolded configurations, with transitions between the two states (Figure 6-4).

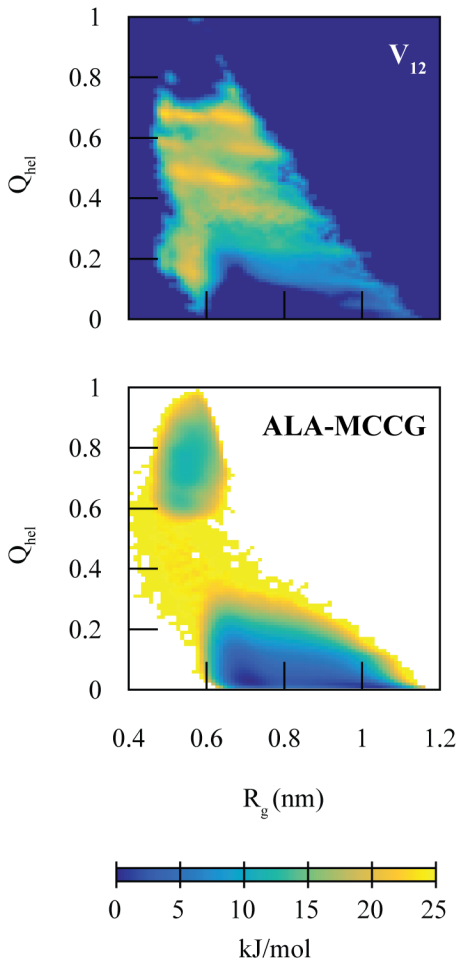

Figure 6-4 MCCG Model of dodecaalanine

Top. Tabulated coupling term, ($V_{12}(\boldsymbol{Q})$), used for the dodecaalanine MCCG model, as a function of helicity (Q_{hel}) and radius of gyration (R_g).

Bottom. Resulting MCCG PMF for dodecaalanine (ALA-MCCG). ALA-MCCG reproduces 2-state behavior, but does not reproduce the barrier height or well depths.

While the MCCG model was able to describe the two-state behavior of dodecaalanine, it was not able to accurately reproduce neither the barrier height nor the free energy difference between the two configurations. The high PMF barrier, 25 kJ/mol in the MCCG model versus 15 kJ/mol in the AA model, suggests that the coupling in the transition region is too low. We therefore

refined the MCCG model by using the iterative procedure described in Equation (6.6). Since the MCCG PMF is most different compared to the AA PMF in the transition, this slowly increases the coupling in the transition region, and the MCCG PMF barrier will approach the AA PMF barrier. As seen in Figure 6-5, the iterative MCCG procedure reduces the free energy barrier to 20 kJ/mol by the third iteration and 17 kJ/mol (within an order of k_bT) by the seventh iteration. Additionally, the PMF well depths, at 0 kJ/mol for both states in the AA PMF is matched by the seventh iteration. It should be noted that the AA PMF contains at least 10 local minima, which are smoothed out in the CG PMF. While MCCG substantially improves the transition region, it should not be expected to improve other aspects of the CG model, especially features in the diabatic wells. The primary motions of the system are driven by the diabatic potentials – it is only in the transition region that the coupling term has an effect. But, with MCCG, diabatic states derived from simple CG models can more accurately reproduce the AA PMF compared to more sophisticated CG modeling techniques.

We further analyzed the MCCG trajectories to determine whether ALA-MCCG can accurately capture additional CVs that were not included in the coupling term (SI FIGURE 1). For each additional CV, MCCG produces a PMF that is a mix between the ALA-HENM-F and ALA-BI-U models. The two collective variables most correlated with the coupled CVs, R_g^{22} (the second component of the gyration tensor which describes the width of the polymer) and RMSD improve the most compared towards the 1D AA PMFs. But, end-to-end distance, which is least correlated with the coupled CVs, is significantly worse at reproducing the reference AA PMF. This demonstrates the importance of choosing good CVs for the coupling term. CVs not correlated with the coupled CVs may be adversely affected by the MCCG procedure. By

reducing the many-body PMF to the PMF dependent only upon a few CVs, some information is lost. Choosing CVs that can best represent the many body PMF will produce the best MCCG models. When building MCCG models, it is important to check whether properties not correlated with the coupled CVs are worsened.

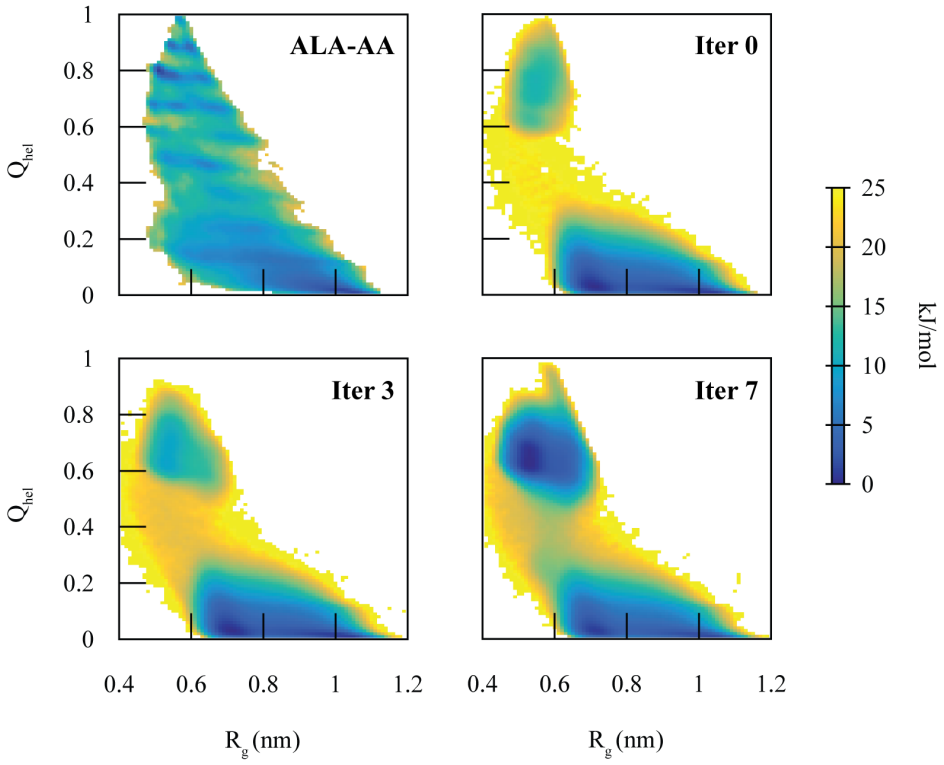

Figure 6-5 PMFs of dodecaalanine iterative MCCG model.
2D PMFs as a function of helicity (Q_{hel}) and radius of gyration (R_g) comparing the mapped AA system (ALA-AA) with various iterations (Iter X) of MCCG. The iterative procedure improves the difference in free energy difference between the two states, as well as the free energy barrier to match the AA system.

6.4.2 Endophilin H0

The folding process of endophilin H0, a 22 residue amphipathic helix that targets curved membranes, has been previously studied by (Cui et al., 2013). The folding process was characterized using the CVs αβ similarity and the number of backbone hydrogen bonds. These CVs can only be described using atomistic detail. Here, we chose to characterize the folding process using the $RMSD$ from the idealized folded configuration and the second component of the gyration tensor(Vymetal and Vondrasek, 2011) (R_g^{22}) of the Cα coordinates (Figure 6-6A). These CVs adequately separate the two states and contain a minimal transition region. The folded configuration of H0 is characterized by R_g^{22} and $RMSD$ values less than 0.4 nm, while the unfolded configuration is characterized by $RMSD > 0.5$ nm.

A BI CG model of the unfolded configuration (H0-BI-U) and a hENM model of folded configuration (H0-HENM-F) accurately reproduced respectively, the unfolded and folded portions of the PMF, along the CVs R_g^{22} and $RMSD$, but with smoothed PMF minima compared to the AA PMF. CG techniques typically smooth out portions of the potential energy surface because the high frequency motions are integrated out of the model. We then constructed an MCCG model of H0 (H0-MCCG). As in the case of dodecaalanine, the coupling is highest in the transition region (Figure 6-6), as well as regions not sampled by the diabatic states ($RMSD > 1.0$ nm and $RMSD < 0.2$ nm).

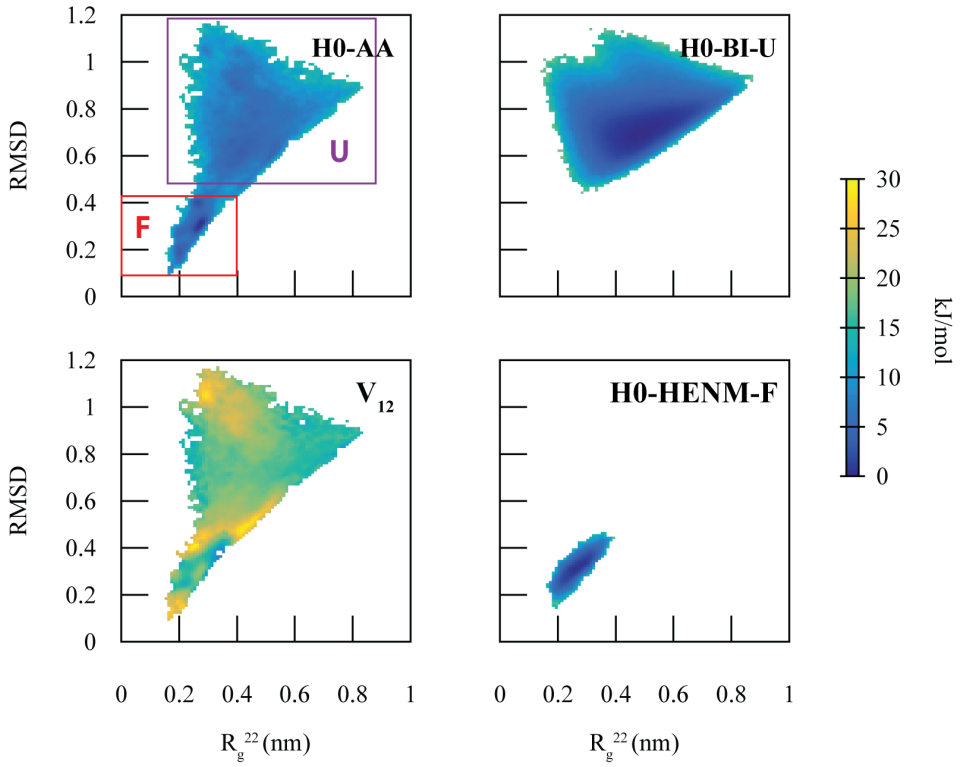

Figure 6-6 PMFs of AA and CG models of endophilin H0
2D PMFs as a function of root mean squared deviation ($RMSD$) and the second component of the gyration tensor (R_g^{22}) for H0. For the mapped AA system (H0-AA), the folded state is denoted in the red square (F), and the unfolded state (U) in purple. The Boltzmann inversion CG model of the unfolded state (H0-BI-U) captures the unfolded portion of the AA PMF, and the hENM CG model of the folded state (H0-BI-F) captures the folded portion of the AA PMF. The coupling term ($V_{12}(\boldsymbol{Q})$) is at a maximum in the transition region (RMSD=0.45) as well as the portions of the PMF unsampled by H0-BI-U and H0-HENM-F.

H0-MCCG exhibits two-state behavior, sampling both the unfolded and folded configurations, with transitions between the two states (Figure 6-7). H0-MCCG has a barrier height of 10 kJ/mol, within an order of k_bT of the barrier height of 7.5 kJ/mol in the AA PMF. As in the case of dodecalanine, the initial barrier height is incorrect. Applying the iterative

MCCG method for only 2 iterations for H0-MCCG reproduces the 7.5 kJ/mol barrier height at $RMSD = 0.5$ nm.

The H0-MCCG PMF is in much better agreement with the AA PMF compared to ALA-MCCG. This is likely caused by the more accurate diabatic states in the case of H0-MCCG. The coupling term is required to do less work to reproduce the AA PMF, as it is already more accurately represented by the individual CG models. Additionally, the number of iterations required to converge the barrier height and PMF minima is significantly reduced due to the much improved CG diabatic states.

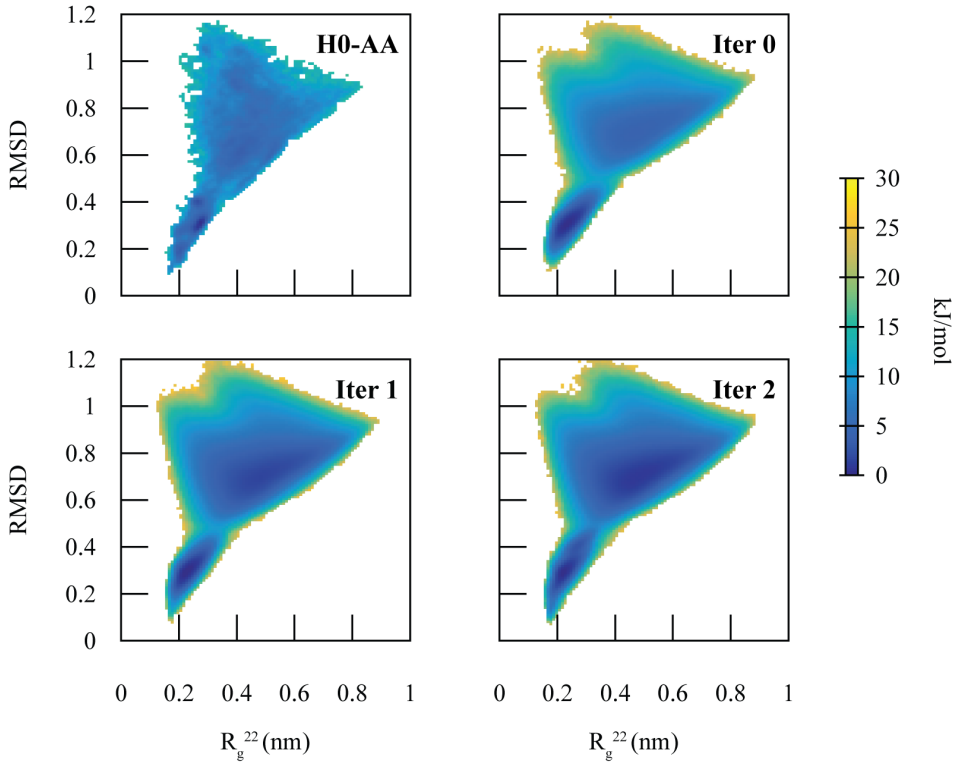

Figure 6-7 PMFs of iterative MCCG model for endophilin H0.
2D PMFs as a function of root mean squared deviation ($RMSD$) and the second component of the gyration tensor (R_g^{22}) comparing the mapped AA system (H0-AA) with various iterations (Iter X) of MCCG. The iterative procedure improves the difference in free energy difference between the two states, and converges to H0-AA within 2 iterations.

6.5 Conclusion

The method introduced in this work is able to capture the transitions between multiple CG models in a way that can reproduce the AA PMF for the process. Proteins can undergo major conformational changes that cannot always be captured by a single CG model. This can especially be the case when conformational changes are due to degrees of freedom that have been absorbed into the CG site. Although previous methods have been developed that can simulate a CG model that transitions between multiple conformational states, these methods are not guaranteed to reproduce key features of the PMF. Our new method is able to use AA-based off-diagonal coupling, the $V_{12}(\boldsymbol{Q})$ term in eq. (6.5), to reproduce the correct distribution of states as well as the transition barrier.

An important strength in our new method is the fact that the off-diagonal coupling term is a function of the CVs that describe the transition process. When a constant off-diagonal coupling term is used, the system is unable to capture the correct location of the transition barrier. Using a coupling term that is a function of the transition CVs not only allows the system to reproduce the transition barrier, but also leads to more realistic descriptions of the transition process. Additionally, as the method is applied to other systems, more complicated CVs can be used to take into account other influences on structural transformations, such as environmental interactions. As long as a PMF can be calculated to describe the transition between states, whether from AA simulations or from experiment, an accurate MCCG model can be parameterized for the system of study.

Another advantage of the MCCG is the ability to use simple CG models to capture complex, multistate behavior instead of more complex CG methods. An accurate MCCG model instead

requires the calculation of the AA PMF, for which many methods have been developed (Barducci et al., 2008; Darve et al., 2008; Laio and Parrinello, 2002b; Sun et al., 2016; Torrie and Valleau, 1977). If CG models are made for each of individual protein conformations and the AA PMF is known for the structural transition, then an MCCG model can be created for the system. The major reduction in computational effort can be taken advantage of to investigate new emergent behavior. When many proteins are allowed to interact with each other, as occurs in cellular environments, the MCCG model will not only be influenced by the AA PMF for a single protein, but also by the interactions between proteins on the CG level. This will lead to simulations that will be more representative of actual cellular environments, where protein conformations are influenced by both smaller scale atomistic level interactions and by the larger scale protein motions and protein-protein interactions.

Bibliography

Abraham, M.J., Murtola, T., Schulz, R., Páll, S., Smith, J.C., Hess, B., and Lindahl, E. (2015). GROMACS: High performance molecular simulations through multi-level parallelism from laptops to supercomputers. SoftwareX *1–2*, 19-25.

Adrover, M., Martorell, G., Martin, S.R., Urosev, D., Konarev, P.V., Svergun, D.I., Daura, X., Temussi, P., and Pastore, A. (2012). The role of hydration in protein stability: comparison of the cold and heat unfolded states of Yfh1. J Mol Biol *417*, 413-424.

Almeida, P.F., Ladokhin, A.S., and White, S.H. (2012). Hydrogen-bond energetics drive helix formation in membrane interfaces. Biochim Biophys Acta *1818*, 178-182.

Ambroso, M.R., Hegde, B.G., and Langen, R. (2014). Endophilin A1 induces different membrane shapes using a conformational switch that is regulated by phosphorylation. Proc Natl Acad Sci U S A *111*, 6982-6987.

Angelova, M.I., Soléau, S., Méléard, P., Faucon, J.F., and Bothorel, P. (1992). Preparation of giant vesicles by external AC electric fields . Kinetics and applications. Progress in Colloid & Polymer Science *89*, 127-131.

Arkhipov, A., Yin, Y., and Schulten, K. (2008). Four-scale description of membrane sculpting by BAR domains. Biophysical Journal *95*, 2806-2821.

Armbruster, U., Labs, M., Pribil, M., Viola, S., Xu, W., Scharfenberg, M., Hertle, A.P., Rojahn, U., Jensen, P.E., Rappaport, F.*, et al.* (2013). Arabidopsis CURVATURE THYLAKOID1 proteins modify thylakoid architecture by inducing membrane curvature. The Plant cell *25*, 2661-2678.

Arrese, E.L., Rivera, L., Hamada, M., Mirza, S., Hartson, S.D., Weintraub, S., and Soulages, J.L. (2008). Function and structure of lipid storage droplet protein 1 studied in lipoprotein complexes. Archives of biochemistry and biophysics *473*, 42-47.

Bacle, A., Gautier, R., Jackson, C.L., Fuchs, P.F., and Vanni, S. (2017). Interdigitation between Triglycerides and Lipids Modulates Surface Properties of Lipid Droplets. Biophys J *112*, 1417-1430.

Barducci, A., Bussi, G., and Parrinello, M. (2008). Well-tempered Metadynamics: A smoothly converging and tunable free-energy method. Physical review letters *100*.

Bartz, R., Li, W.H., Venables, B., Zehmer, J.K., Roth, M.R., Welti, R., Anderson, R.G., Liu, P., and Chapman, K.D. (2007). Lipidomics reveals that adiposomes store ether lipids and mediate phospholipid traffic. J Lipid Res *48*, 837-847.

Ben M'barek, K., Ajjaji, D., Chorlay, A., Vanni, S., Foret, L., and Thiam, A.R. (2017). ER Membrane Phospholipids and Surface Tension Control Cellular Lipid Droplet Formation. Dev Cell.

Bennett, C.H. (1976). Efficient estimation of free energy differences from Monte Carlo data. Journal of Computational Physics *22*, 245-268.

Bernardi, R.C., Melo, M.C.R., and Schulten, K. (2015). Enhanced sampling techniques in molecular dynamics simulations of biological systems. Biochim Biophys Acta *1850*, 872-877.

Best, R.B., Chen, Y.-G., and Hummer, G. (2005). Slow protein conformational dynamics from multiple experimental structures: The helix/sheet transition of Arc repressor. Structure *13*, 1755-1763.

Best, R.B., Zhu, X., Shim, J., Lopes, P.E., Mittal, J., Feig, M., and Mackerell, A.D., Jr. (2012). Optimization of the additive CHARMM all-atom protein force field targeting improved sampling of the backbone phi, psi and side-chain chi(1) and chi(2) dihedral angles. J Chem Theory Comput *8*, 3257-3273.

Bianco, V., and Franzese, G. (2015). Contribution of Water to Pressure and Cold Denaturation of Proteins. Physical review letters *115*, 108101.

Bickel, P.E., Tansey, J.T., and Welte, M.A. (2009). PAT proteins, an ancient family of lipid droplet proteins that regulate cellular lipid stores. Biochim Biophys Acta *1791*, 419-440.

Bigay, J., and Antonny, B. (2012). Curvature, lipid packing, and electrostatics of membrane organelles: defining cellular territories in determining specificity. Dev Cell *23*, 886-895.

Bigay, J., Casella, J.F., Drin, G., Mesmin, B., and Antonny, B. (2005). ArfGAP1 responds to membrane curvature through the folding of a lipid packing sensor motif. The EMBO journal *24*, 2244-2253.

Boeszoermenyi, A., Nagy, H.M., Arthanari, H., Pillip, C.J., Lindermuth, H., Luna, R.E., Wagner, G., Zechner, R., Zangger, K., and Oberer, M. (2015). Structure of a CGI-58 motif provides the molecular basis of lipid droplet anchoring. J Biol Chem *290*, 26361-26372.

Boucrot, E., Pick, A., Camdere, G., Liska, N., Evergren, E., McMahon, H.T., and Kozlov, M.M. (2012). Membrane fission is promoted by insertion of amphipathic helices and is restricted by crescent BAR domains. Cell *149*, 124-136.

Boulant, S., Montserret, R., Hope, R.G., Ratinier, M., Targett-Adams, P., Lavergne, J.P., Penin, F., and McLauchlan, J. (2006). Structural determinants that target the hepatitis C virus core protein to lipid droplets. J Biol Chem *281*, 22236-22247.

Bouvet, S., Golinelli-Cohen, M.P., Contremoulins, V., and Jackson, C.L. (2013). Targeting of the Arf-GEF GBF1 to lipid droplets and Golgi membranes. J Cell Sci *126*, 4794-4805.

Bradley, P., Misura, K.M., and Baker, D. (2005). Toward high-resolution de novo structure prediction for small proteins. Science (New York, NY) *309*, 1868-1871.

Brady, J.P., Claridge, J.K., Smith, P.G., and Schnell, J.R. (2015). A conserved amphipathic helix is required for membrane tubule formation by Yop1p. Proc Natl Acad Sci U S A *112*, E639-648.

Brasaemle, D.L., Dolios, G., Shapiro, L., and Wang, R. (2004). Proteomic analysis of proteins associated with lipid droplets of basal and lipolytically stimulated 3T3-L1 adipocytes. J Biol Chem *279*, 46835-46842.

Braun, A.R., Sevcsik, E., Chin, P., Rhoades, E., Tristram-Nagle, S., and Sachs, J.N. (2012). α-Synuclein induces both positive mean curvature and negative Gaussian curvature in membranes. Journal of the American Chemical Society *134*, 2613-2620.

Bulankina, A.V., Deggerich, A., Wenzel, D., Mutenda, K., Wittmann, J.G., Rudolph, M.G., Burger, K.N., and Honing, S. (2009). TIP47 functions in the biogenesis of lipid droplets. J Cell Biol *185*, 641-655.

Bussi, G., Donadio, D., and Parrinello, M. (2007). Canonical sampling through velocity rescaling. The Journal of Chemical Physics *126*, 014101.

Calero-Rubio, C., Paik, B., Jia, X., Kiick, K.L., and Roberts, C.J. (2016). Predicting unfolding thermodynamics and stable intermediates for alanine-rich helical peptides with the aid of coarse-grained molecular simulation. Biophysical Chemistry *217*, 8-19.

Camilloni, C., Bonetti, D., Morrone, A., Giri, R., Dobson, C.M., Brunori, M., Gianni, S., and Vendruscolo, M. (2016). Towards a structural biology of the hydrophobic effect in protein folding. Sci Rep *6*, 28285.

Carmichael, S.P., and Shell, M.S. (2012). A new multiscale algorithm and its application to coarse-grained peptide models for self-assembly. J Phys Chem B *116*, 8383-8393.

Carpenter, A.E., Jones, T.R., Lamprecht, M.R., Clarke, C., Kang, I.H., Friman, O., Guertin, D.A., Chang, J.H., Lindquist, R.A., Moffat, J.*, et al.* (2006). CellProfiler: image analysis software for identifying and quantifying cell phenotypes. Genome biology *7*, R100.

Chang, Y.T., and Miller, W.H. (1990). An empirical valence bond model for constructing global potential energy surfaces for chemical reactions of polyatomic molecular systems. The Journal of Physical Chemistry *94*, 5884-5888.

Cho, H.M., and Chu, J.W. (2009). Inversion of radial distribution functions to pair forces by solving the Yvon-Born-Green equation iteratively. J Chem Phys *131*, 134107.

Choudhary, V., Ojha, N., Golden, A., and Prinz, W.A. (2015). A conserved family of proteins facilitates nascent lipid droplet budding from the ER. J Cell Biol *211*, 261-271.

Chu, J.-W., and Voth, G.A. (2007). Coarse-grained free energy functions for studying protein conformational changes: A double-well network model. Biophysical Journal *93*, 3860-3871.

Čopič, A., Antoine-Bally, S., Giménez-Andrés, M., La Torre Garay, C., Antonny, B., Manni, M.M., Pagnotta, S., Guihot, J., and Jackson, C.L. (2018). A giant amphipathic helix from a perilipin that is adapted for coating lipid droplets. Nature Communications *9*.

Cui, H., Lyman, E., and Voth, G.A. (2011). Mechanism of membrane curvature sensing by amphipathic helix containing proteins. Biophys J *100*, 1271-1279.

Cui, H., Mim, C., Vázquez, Francisco X., Lyman, E., Unger, Vinzenz M., and Voth, Gregory A. (2013). Understanding the role of amphipathic helices in N-BAR domain driven membrane remodeling. Biophysical Journal *104*, 404-411.

Dama, J.F., Hocky, G.M., Sun, R., and Voth, G.A. (2015). Exploring Valleys without Climbing Every Peak: More Efficient and Forgiving Metabasin Metadynamics via Robust On-the-Fly Bias Domain Restriction. J Chem Theory Comput *11*, 5638-5650.

Dama, J.F., Parrinello, M., and Voth, G.A. (2014a). Well-Tempered Metadynamics Converges Asymptotically. Physical review letters *112*.

Dama, J.F., Rotskoff, G., Parrinello, M., and Voth, G.A. (2014b). Transition-Tempered Metadynamics: Robust, Convergent Metadynamics via On-the-Fly Transition Barrier Estimation. J Chem Theory Comput *10*, 3626-3633.

Darve, E., and Pohorille, A. (2001). Calculating free energies using average force. The Journal of Chemical Physics *115*, 9169-9183.

Darve, E., Rodriguez-Gomez, D., and Pohorille, A. (2008). Adaptive biasing force method for scalar and vector free energy calculations. J Chem Phys *128*, 144120.

de Jong, D.H., Singh, G., Bennett, W.F., Arnarez, C., Wassenaar, T.A., Schafer, L.V., Periole, X., Tieleman, D.P., and Marrink, S.J. (2013). Improved parameters for the Martini coarse-grained protein force field. J Chem Theory Comput *9*, 687-697.

de Marco, G., and Várnai, P. (2009). Molecular simulation of conformational transitions in biomolecules using a combination of structure-based potential and empirical valence bond theory. Physical Chemistry Chemical Physics *11*, 10694.

Doucet, C.M., Esmery, N., de Saint-Jean, M., and Antonny, B. (2015). Membrane Curvature Sensing by Amphipathic Helices Is Modulated by the Surrounding Protein Backbone. PloS one *10*, e0137965.

Drin, G., and Antonny, B. (2010). Amphipathic helices and membrane curvature. FEBS Lett *584*, 1840-1847.

Drin, G., Casella, J.F., Gautier, R., Boehmer, T., Schwartz, T.U., and Antonny, B. (2007). A general amphipathic alpha-helical motif for sensing membrane curvature. Nature structural & molecular biology *14*, 138-146.

Drin, G., Morello, V., Casella, J.F., Gounon, P., and Antonny, B. (2008). Asymmetric tethering of flat and curved lipid membranes by a golgin. Science (New York, NY) *320*, 670-673.

Dunne, S.J., Cornell, R.B., Johnson, J.E., Glover, N.R., and Tracey, A.S. (1996). Structure of the membrane binding domain of CTP:phosphocholine cytidylyltransferase. Biochemistry *35*, 11975-11984.

Eisenberg, D., Weiss, R.M., and Terwilliger, T.C. (1982). The helical hydrophobic moment: a measure of the amphiphilicity of a helix. Nature *299*, 371-374.

Elofsson, A., Deplazes, E., Louhivuori, M., Jayatilaka, D., Marrink, S.J., and Corry, B. (2012). Structural investigation of MscL gating using experimental data and coarse grained MD Simulations. PLoS Computational Biology *8*, e1002683.

Essmann, U., Perera, L., Berkowitz, M.L., Darden, T., Lee, H., and Pedersen, L.G. (1995). A smooth particle mesh Ewald method. The Journal of Chemical Physics *103*, 8577-8593.

Evans, E., and Rawicz, W. (1990). Entropy-driven tension and bending elasticity in condensed-fluid membranes. Physical review letters *64*, 2094-2097.

Farsad, K., Ringstad, N., Takei, K., Floyd, S.R., Rose, K., and De Camilli, P. (2001). Generation of high curvature membranes mediated by direct endophilin bilayer interactions. J Cell Biol *155*, 193-200.

Fernandez-Vidal, M., Jayasinghe, S., Ladokhin, A.S., and White, S.H. (2007). Folding amphipathic helices into membranes: amphiphilicity trumps hydrophobicity. J Mol Biol *370*, 459-470.

Ford, M.G., Mills, I.G., Peter, B.J., Vallis, Y., Praefcke, G.J., Evans, P.R., and McMahon, H.T. (2002). Curvature of clathrin-coated pits driven by epsin. Nature *419*, 361-366.

Frost, A., Unger, V.M., and De Camilli, P. (2009). The BAR domain superfamily: membrane-molding macromolecules. Cell *137*, 191-196.

Fuhrmans, M., and Marrink, S.J. (2012). Molecular view of the role of fusion peptides in promoting positive membrane curvature. Journal of the American Chemical Society *134*, 1543-1552.

Fujimoto, T., and Parton, R.G. (2011). Not just fat: the structure and function of the lipid droplet. Cold Spring Harb Perspect Biol *3*.

Fujimoto, Y., Itabe, H., Sakai, J., Makita, M., Noda, J., Mori, M., Higashi, Y., Kojima, S., and Takano, T. (2004). Identification of major proteins in the lipid droplet-enriched fraction isolated from the human hepatocyte cell line HuH7. Biochim Biophys Acta *1644*, 47-59.

Gallop, J.L., Jao, C.C., Kent, H.M., Butler, P.J.G., Evans, P.R., Langen, R., and T McMahon, H. (2006). Mechanism of endophilin N-BAR domain-mediated membrane curvature. Embo Journal *25*, 2898-2910.

Gannon, J., Fernandez-Rodriguez, J., Alamri, H., Feng, S.B., Kalantari, F., Negi, S., Wong, A.H., Mazur, A., Asp, L., Fazel, A.*, et al.* (2014). ARFGAP1 is dynamically associated with lipid droplets in hepatocytes. PloS one *9*, e111309.

Gauthier, N.C., Masters, T.A., and Sheetz, M.P. (2012). Mechanical feedback between membrane tension and dynamics. Trends Cell Biol *22*, 527-535.

Gautier, R., Douguet, D., Antonny, B., and Drin, G. (2008). HELIQUEST: a web server to screen sequences with specific alpha-helical properties. Bioinformatics *24*, 2101-2102.

Gill, R.L., Jr., Castaing, J.P., Hsin, J., Tan, I.S., Wang, X., Huang, K.C., Tian, F., and Ramamurthi, K.S. (2015). Structural basis for the geometry-driven localization of a small protein. Proc Natl Acad Sci U S A *112*, E1908-1915.

Gluchowski, N.L., Becuwe, M., Walther, T.C., and Farese, R.V., Jr. (2017). Lipid droplets and liver disease: from basic biology to clinical implications. Nat Rev Gastroenterol Hepatol.

Grime, John M.A., and Voth, Gregory A. (2012). Early Stages of the HIV-1 Capsid Protein Lattice Formation. Biophysical Journal *103*, 1774-1783.

Grippa, A., Buxo, L., Mora, G., Funaya, C., Idrissi, F.Z., Mancuso, F., Gomez, R., Muntanya, J., Sabido, E., and Carvalho, P. (2015). The seipin complex Fld1/Ldb16 stabilizes ER-lipid droplet contact sites. J Cell Biol *211*, 829-844.

Grossfield, A. WHAM: an implementation of the weighted histogram analysis method.

Guo, Y., Walther, T.C., Rao, M., Stuurman, N., Goshima, G., Terayama, K., Wong, J.S., Vale, R.D., Walter, P., and Farese, R.V. (2008). Functional genomic screen reveals genes involved in lipid-droplet formation and utilization. Nature *453*, 657-661.

Hamilton, J.A., and Small, D.M. (1981). Solubilization and localization of triolein in phosphatidylcholine bilayers: a 13C NMR study. Proc Natl Acad Sci U S A *78*, 6878-6882.

Hennere, G., Havard, L., Bonan, B., and Prognon, P. (2005). Stability of cidofovir in extemporaneously prepared syringes. Am J Health Syst Pharm *62*, 506-509.

Hennere, G., Prognon, P., Brion, F., and Nicolis, I. (2009). Molecular dynamics study of a phospholipid monolayer at a water/triglyceride interface: towards lipid emulsion modelling. Chem Phys Lipids *157*, 86-93.

Hess, B. (2008). P-LINCS: A Parallel Linear Constraint Solver for Molecular Simulation. J Chem Theory Comput *4*, 116-122.

Hoover, W.G. (1985). Canonical dynamics: Equilibrium phase-space distributions. Phys Rev A Gen Phys *31*, 1695-1697.

Hristova, K., Wimley, W.C., Mishra, V.K., Anantharamiah, G.M., Segrest, J.P., and White, S.H. (1999). An amphipathic alpha-helix at a membrane interface: a structural study using a novel X-ray diffraction method. J Mol Biol *290*, 99-117.

Humphrey, W., Dalke, A., and Schulten, K. (1996). VMD: visual molecular dynamics. J Mol Graph *14*, 33-38, 27-38.

Izvekov, S., and Voth, G.A. (2005). Multiscale coarse graining of liquid-state systems. The Journal of Chemical Physics *123*, 134105.

Jacquier, N., Choudhary, V., Mari, M., Toulmay, A., Reggiori, F., and Schneiter, R. (2011). Lipid droplets are functionally connected to the endoplasmic reticulum in Saccharomyces cerevisiae. J Cell Sci *124*, 2424-2437.

Jao, C.C., Hegde, B.G., Gallop, J.L., Hegde, P.B., McMahon, H.T., Haworth, I.S., and Langen, R. (2010). Roles of amphipathic helices and the bin/amphiphysin/rvs (BAR) domain of endophilin in membrane curvature generation. The Journal of biological chemistry *285*, 20164-20170.

Javanainen, M., and Martinez-Seara, H. (2016). Efficient preparation and analysis of membrane and membrane protein systems. Biochim Biophys Acta *1858*, 2468-2482.

Jo, S., Kim, T., and Im, W. (2007). Automated builder and database of protein/membrane complexes for molecular dynamics simulations. PloS one *2*, e880.

Jo, S., Kim, T., Iyer, V.G., and Im, W. (2008). CHARMM-GUI: a web-based graphical user interface for CHARMM. J Comput Chem *29*, 1859-1865.

Jo, S., Lim, J.B., Klauda, J.B., and Im, W. (2009). CHARMM-GUI Membrane Builder for mixed bilayers and its application to yeast membranes. Biophys J *97*, 50-58.

Jones, D.T. (2007). Improving the accuracy of transmembrane protein topology prediction using evolutionary information. Bioinformatics *23*, 538-544.

Jones, D.T., Taylor, W.R., and Thornton, J.M. (1994). A model recognition approach to the prediction of all-helical membrane protein structure and topology. Biochemistry *33*, 3038-3049.

Kahn, R.A., Randazzo, P., Serafini, T., Weiss, O., Rulka, C., Clark, J., Amherdt, M., Roller, P., Orci, L., and Rothman, J.E. (1992). The amino terminus of ADP-ribosylation factor (ARF) is a critical determinant of ARF activities and is a potent and specific inhibitor of protein transport. J Biol Chem *267*, 13039-13046.

Kalli, A.C., Rog, T., Vattulainen, I., Campbell, I.D., and Sansom, M.S.P. (2016). The integrin receptor in biologically relevant bilayers: Insights from Molecular Dynamics simulations. The Journal of Membrane Biology *250*, 337-351.

Kim, D.E., Chivian, D., and Baker, D. (2004). Protein structure prediction and analysis using the Robetta server. Nucleic Acids Res *32*, W526-531.

Kimmel, A.R., and Sztalryd, C. (2016). The Perilipins: Major Cytosolic Lipid Droplet-Associated Proteins and Their Roles in Cellular Lipid Storage, Mobilization, and Systemic Homeostasis. Annual review of nutrition *36*, 471-509.

Klauda, J.B., Venable, R.M., Freites, J.A., O'Connor, J.W., Tobias, D.J., Mondragon-Ramirez, C., Vorobyov, I., MacKerell, A.D., Jr., and Pastor, R.W. (2010). Update of the CHARMM all-atom additive force field for lipids: validation on six lipid types. J Phys Chem B *114*, 7830-7843.

Koivuniemi, A., Heikela, M., Kovanen, P.T., Vattulainen, I., and Hyvonen, M.T. (2009). Atomistic simulations of phosphatidylcholines and cholesteryl esters in high-density lipoprotein-sized lipid droplet and trilayer: clues to cholesteryl ester transport and storage. Biophys J *96*, 4099-4108.

Kory, N., Farese, R.V., Jr., and Walther, T.C. (2016). Targeting Fat: Mechanisms of Protein Localization to Lipid Droplets. Trends Cell Biol *26*, 535-546.

Kory, N., Thiam, A.R., Farese, R.V., Jr., and Walther, T.C. (2015). Protein Crowding Is a Determinant of Lipid Droplet Protein Composition. Dev Cell *34*, 351-363.

Krahmer, N., Farese, R.V., Jr., and Walther, T.C. (2013a). Balancing the fat: lipid droplets and human disease. EMBO Mol Med *5*, 973-983.

Krahmer, N., Guo, Y., Wilfling, F., Hilger, M., Lingrell, S., Heger, K., Newman, H.W., Schmidt-Supprian, M., Vance, D.E., Mann, M*., et al.* (2011). Phosphatidylcholine synthesis for lipid droplet expansion is mediated by localized activation of CTP:phosphocholine cytidylyltransferase. Cell Metab *14*, 504-515.

Krahmer, N., Hilger, M., Kory, N., Wilfling, F., Stoehr, G., Mann, M., Farese, R.V., Jr., and Walther, T.C. (2013b). Protein correlation profiles identify lipid droplet proteins with high confidence. Mol Cell Proteomics *12*, 1115-1126.

Kumar, S., Rosenberg, J.M., Bouzida, D., Swendsen, R.H., and Kollman, P.A. (1995). Multidimensional free-energy calculations using the weighted histogram analysis method. Journal of Computational Chemistry *16*, 1339-1350.

Kwok, R., and Evans, E. (1981). Thermoelasticity of large lecithin bilayer vesicles. Biophys J *35*, 637-652.

Ladokhin, A.S., and White, S.H. (1999). Folding of amphipathic alpha-helices on membranes: energetics of helix formation by melittin. J Mol Biol *285*, 1363-1369.

Lagace, T.A., and Ridgway, N.D. (2005). The rate-limiting enzyme in phosphatidylcholine synthesis regulates proliferation of the nucleoplasmic reticulum. Molecular biology of the cell *16*, 1120-1130.

Lai, C.-L., Srivastava, A., Pilling, C., Chase, A.R., Falke, J.J., and Voth, G.A. (2013). Molecular Mechanism of Membrane Binding of the GRP1 PH Domain. Journal of Molecular Biology *425*, 3073-3090.

Laio, A., and Parrinello, M. (2002a). Escaping free-energy minima. Proc Natl Acad Sci U S A *99*, 12562-12566.

Laio, A., and Parrinello, M. (2002b). Escaping free-energy minima. Proceedings of the National Academy of Sciences *99*, 12562-12566.

Langowski, J., Globisch, C., Krishnamani, V., Deserno, M., and Peter, C. (2013). Optimization of an Elastic Network Augmented Coarse Grained Model to Study CCMV Capsid Deformation. PloS one *8*, e60582.

Lee, J., Cheng, X., Swails, J.M., Yeom, M.S., Eastman, P.K., Lemkul, J.A., Wei, S., Buckner, J., Jeong, J.C., Qi, Y.*, et al.* (2016). CHARMM-GUI Input Generator for NAMD, GROMACS, AMBER, OpenMM, and CHARMM/OpenMM Simulations Using the CHARMM36 Additive Force Field. J Chem Theory Comput *12*, 405-413.

Lee, M.C., Orci, L., Hamamoto, S., Futai, E., Ravazzola, M., and Schekman, R. (2005). Sar1p N-terminal helix initiates membrane curvature and completes the fission of a COPII vesicle. Cell *122*, 605-617.

Lelimousin, M., Limongelli, V., and Sansom, M.S.P. (2016). Conformational changes in the epidermal growth factor receptor: Role of the transmembrane domain investigated by coarse-grained MetaDynamics free energy calculations. Journal of the American Chemical Society *138*, 10611-10622.

Li, J., Ziemba, B.P., Falke, J.J., and Voth, G.A. (2014). Interactions of Protein Kinase C-α C1A and C1B Domains with Membranes: A Combined Computational and Experimental Study. Journal of the American Chemical Society *136*, 11757-11766.

Lin, P., Chen, X., Moktan, H., Arrese, E.L., Duan, L., Wang, L., Soulages, J.L., and Zhou, D.H. (2014). Membrane attachment and structure models of lipid storage droplet protein 1. Biochim Biophys Acta *1838*, 874-881.

Lindorff-Larsen, K., Piana S Fau - Dror, R.O., Dror Ro Fau - Shaw, D.E., and Shaw, D.E. How fast-folding proteins fold.

Lippert, R.A., Predescu, C., Ierardi, D.J., Mackenzie, K.M., Eastwood, M.P., Dror, R.O., and Shaw, D.E. (2013). Accurate and efficient integration for molecular dynamics simulations at constant temperature and pressure. The Journal of Chemical Physics *139*.

Liu, P., Kim, B., Friesner, R.A., and Berne, B.J. (2005). Replica exchange with solute tempering: A method for sampling biological systems in explicit water. Proceedings of the National Academy of Sciences *102*, 13749-13754.

Liu, T.Y., Bian, X., Sun, S., Hu, X., Klemm, R.W., Prinz, W.A., Rapoport, T.A., and Hu, J. (2012). Lipid interaction of the C terminus and association of the transmembrane segments facilitate atlastin-mediated homotypic endoplasmic reticulum fusion. Proc Natl Acad Sci U S A *109*, E2146-2154.

Lu, L., Dama, J.F., and Voth, G.A. (2013). Fitting coarse-grained distribution functions through an iterative force-matching method. The Journal of Chemical Physics *139*, 121906.

Lyman, E., Pfaendtner, J., and Voth, G.A. (2008). Systematic multiscale parameterization of heterogeneous elastic network models of proteins. Biophysical Journal *95*, 4183-4192.

MacCallum, J.L., Bennett, W.F., and Tieleman, D.P. (2008). Distribution of amino acids in a lipid bilayer from computer simulations. Biophys J *94*, 3393-3404.

MacKerell, A.D., Bashford, D., Bellott, M., Dunbrack, R.L., Evanseck, J.D., Field, M.J., Fischer, S., Gao, J., Guo, H., Ha, S.*, et al.* (1998). All-atom empirical potential for molecular modeling and dynamics studies of proteins. J Phys Chem B *102*, 3586-3616.

Maragakis, P., and Karplus, M. (2005). Large amplitude conformational change in proteins explored with a plastic network model: Adenylate kinase. Journal of Molecular Biology *352*, 807-822.

Marcus, R.A. (1964). Chemical and electrochemical electron-transfer theory. Annual Review of Physical Chemistry *15*, 155-196.

Marrink, S.J., and Tieleman, D.P. (2013). Perspective on the Martini model. Chemical Society Reviews *42*, 6801.

Martinez, L., Andrade, R., Birgin, E.G., and Martinez, J.M. (2009). PACKMOL: a package for building initial configurations for molecular dynamics simulations. J Comput Chem *30*, 2157-2164.

Martyna, G.J., Tobias, D.J., and Klein, M.L. (1994). Constant pressure molecular dynamics algorithms. The Journal of Chemical Physics *101*, 4177-4189.

McMahon, H.T., and Gallop, J.L. (2005). Membrane curvature and mechanisms of dynamic cell membrane remodelling. Nature *438*, 590-596.

Meyers, N.L., Wang, L., and Small, D.M. (2012). Apolipoprotein C-I binds more strongly to phospholipid/triolein/water than triolein/water interfaces: a possible model for inhibiting cholesterol ester transfer protein activity and triacylglycerol-rich lipoprotein uptake. Biochemistry *51*, 1238-1248.

Mim, C., and Unger, V.M. (2012). Membrane curvature and its generation by BAR proteins. Trends Biochem Sci *37*, 526-533.

Mitsche, M.A., and Small, D.M. (2013). Surface pressure-dependent conformation change of apolipoprotein-derived amphipathic alpha-helices. J Lipid Res *54*, 1578-1588.

Miyanari, Y., Atsuzawa, K., Usuda, N., Watashi, K., Hishiki, T., Zayas, M., Bartenschlager, R., Wakita, T., Hijikata, M., and Shimotohno, K. (2007). The lipid droplet is an important organelle for hepatitis C virus production. Nature cell biology *9*, 1089-1097.

Monticelli, L., Kandasamy, S.K., Periole, X., Larson, R.G., Tieleman, D.P., and Marrink, S.-J. (2008). The MARTINI coarse-grained force field: Extension to proteins. Journal of Chemical Theory and Computation *4*, 819-834.

Noid, W.G. (2013). Perspective: Coarse-grained models for biomolecular systems. The Journal of Chemical Physics *139*, 090901.

Noid, W.G., Chu, J.-W., Ayton, G.S., Krishna, V., Izvekov, S., Voth, G.A., Das, A., and Andersen, H.C. (2008a). The multiscale coarse-graining method. I. A rigorous bridge between atomistic and coarse-grained models. The Journal of Chemical Physics *128*, 244114.

Noid, W.G., Liu, P., Wang, Y., Chu, J.-W., Ayton, G.S., Izvekov, S., Andersen, H.C., and Voth, G.A. (2008b). The multiscale coarse-graining method. II. Numerical implementation for coarse-grained molecular models. The Journal of Chemical Physics *128*, 244115.

Nugent, T., and Jones, D.T. (2009). Transmembrane protein topology prediction using support vector machines. BMC Bioinformatics *10*, 159.

Ohsaki, Y., Kawai, T., Yoshikawa, Y., Cheng, J., Jokitalo, E., and Fujimoto, T. (2016). PML isoform II plays a critical role in nuclear lipid droplet formation. J Cell Biol *212*, 29-38.

Okazaki, K.i., Koga, N., Takada, S., Onuchic, J.N., and Wolynes, P.G. (2006). Multiple-basin energy landscapes for large-amplitude conformational motions of proteins: Structure-based molecular dynamics simulations. Proceedings of the National Academy of Sciences *103*, 11844-11849.

Ostermeir, K., and Zacharias, M. (2013). Advanced replica-exchange sampling to study the flexibility and plasticity of peptides and proteins. Biochimica et Biophysica Acta (BBA) - Proteins and Proteomics *1834*, 847-853.

Pak, A.J., Grime, J.M.A., Sengupta, P., Chen, A.K., Durumeric, A.E.P., Srivastava, A., Yeager, M., Briggs, J.A.G., Lippincott-Schwartz, J., and Voth, G.A. (2017). Immature HIV-1 lattice assembly dynamics are regulated by scaffolding from nucleic acid and the plasma membrane. Proceedings of the National Academy of Sciences *114*, E10056-E10065.

Parrinello, M., and Rahman, A. (1981). Polymorphic transitions in single crystals: A new molecular dynamics method. Journal of Applied Physics *52*, 7182-7190.

Periole, X., Cavalli, M., Marrink, S.-J., and Ceruso, M.A. (2009). Combining an elastic network with a coarse-grained molecular force field: Structure, dynamics, and intermolecular recognition. Journal of Chemical Theory and Computation *5*, 2531-2543.

Piana, S., and Laio, A. (2007). A bias-exchange approach to protein folding. J Phys Chem B *111*, 4553-4559.

Pichoff, S., and Lutkenhaus, J. (2005). Tethering the Z ring to the membrane through a conserved membrane targeting sequence in FtsA. Molecular microbiology *55*, 1722-1734.

Plimpton, S. (1995). Fast parallel algorithms for short-range molecular dynamics. Journal of Computational Physics *117*, 1-19.

Pogorelov, T.V., Vermaas, J.V., Arcario, M.J., and Tajkhorshid, E. (2014). Partitioning of Amino Acids into a Model Membrane: Capturing the Interface. The Journal of Physical Chemistry B *118*, 1481-1492.

Pol, A., Gross, S.P., and Parton, R.G. (2014). Review: biogenesis of the multifunctional lipid droplet: lipids, proteins, and sites. J Cell Biol *204*, 635-646.

Pollard, T.D., Blanchoin, L., and Mullins, R.D. (2000). Molecular mechanisms controlling actin filament dynamics in nonmuscle cells. Annual Review of Biophysics and Biomolecular Structure *29*, 545-576.

Prevost, C., Sharp, M.E., Kory, N., Lin, Q., Voth, G.A., Farese, R.V., Jr., and Walther, T.C. (2018). Mechanism and Determinants of Amphipathic Helix-Containing Protein Targeting to Lipid Droplets. Dev Cell *44*, 73-86 e74.

Prévost, C., Tsai, F.C., Bassereau, P., and Simunovic, M. (2017). Pulling Membrane Nanotubes from Giant Unilamellar Vesicles. J Vis Exp, e56086.

Raman, S., Vernon, R., Thompson, J., Tyka, M., Sadreyev, R., Pei, J., Kim, D., Kellogg, E., DiMaio, F., Lange, O.*, et al.* (2009). Structure prediction for CASP8 with all-atom refinement using Rosetta. Proteins *77 Suppl 9*, 89-99.

Riniker, S., Allison, J.R., and van Gunsteren, W.F. (2012). On developing coarse-grained models for biomolecular simulation: a review. Physical Chemistry Chemical Physics *14*, 12423.

Roe, D.R., Bergonzo, C., and Cheatham, T.E. (2014). Evaluation of Enhanced Sampling Provided by Accelerated Molecular Dynamics with Hamiltonian Replica Exchange Methods. The Journal of Physical Chemistry B *118*, 3543-3552.

Rohl, C.A., Strauss, C.E., Misura, K.M., and Baker, D. (2004). Protein structure prediction using Rosetta. Methods Enzymol *383*, 66-93.

Roux, B. (1995). The calculation of the potential of mean force using computer simulations. Computer Physics Communications *91*, 275-282.

Rowe, E.R., Mimmack, M.L., Barbosa, A.D., Haider, A., Isaac, I., Ouberai, M.M., Thiam, A.R., Patel, S., Saudek, V., Siniossoglou, S.*, et al.* (2016). Conserved Amphipathic Helices Mediate Lipid Droplet Targeting of Perilipins 1-3. J Biol Chem *291*, 6664-6678.

Rudzinski, J.F., and Bereau, T. (2016). Concurrent parametrization against static and kinetic information leads to more robust coarse-grained force fields. The European Physical Journal Special Topics *225*, 1373-1389.

Rudzinski, J.F., and Noid, W.G. (2015). Bottom-up coarse-graining of peptide ensembles and helix–coil transitions. Journal of Chemical Theory and Computation *11*, 1278-1291.

Ryckaert, J.-P., Ciccotti, G., and Berendsen, H.J.C. (1977). Numerical integration of the cartesian equations of motion of a system with constraints: molecular dynamics of n-alkanes. Journal of Computational Physics *23*, 327-341.

Schindelin, J., Arganda-Carreras, I., Frise, E., Kaynig, V., Longair, M., Pietzsch, T., Preibisch, S., Rueden, C., Saalfeld, S., Schmid, B.*, et al.* (2012). Fiji: an open-source platform for biological-image analysis. Nature methods *9*, 676-682.

Schlick, T., Collepardo-Guevara, R., Halvorsen, L.A., Jung, S., and Xiao, X. (2011). Biomolecular Modeling and simulation: a field coming of age. Q Rev Biophys *44*, 191-228.

Schneider, T., and Stoll, E. (1978). Molecular-dynamics study of a three-dimensional one-component model for distortive phase transitions. Physical Review B *17*, 1302-1322.

Seelig, J. (2004). Thermodynamics of lipid-peptide interactions. Biochim Biophys Acta *1666*, 40-50.

Segrest, J.P., Jones, M.K., De Loof, H., Brouillette, C.G., Venkatachalapathi, Y.V., and Anantharamaiah, G.M. (1992). The amphipathic helix in the exchangeable apolipoproteins: a review of secondary structure and function. J Lipid Res *33*, 141-166.

Shaw, D.E., Dror, R.O., Salmon, J.K., Grossman, J.P., Mackenzie, K.M., Bank, J.A., Young, C., Deneroff, M.M., Batson, B., Bowers, K.J.*, et al.* (2009). Millisecond-scale molecular dynamics simulations on Anton. In Proceedings of the Conference on High Performance Computing Networking, Storage and Analysis (Portland, Oregon: ACM), pp. 1-11.

Shell, M.S. (2008). The relative entropy is fundamental to multiscale and inverse thermodynamic problems. The Journal of Chemical Physics *129*, 144108.

Shirts, M.R., and Chodera, J.D. (2008). Statistically optimal analysis of samples from multiple equilibrium states. J Chem Phys *129*, 124105.

Simunovic, M., Evergren, E., Golushko, I., Prévost, C., Renard, H.-F., Johannes, L., McMahon, H.T., Lorman, V., Voth, G.A., and Bassereau, P. (2016). How curvature-generating proteins build scaffolds on membrane nanotubes. Proceedings of the National Academy of Sciences *113*, 11226-11231.

Simunovic, M., Srivastava, A., and Voth, G.A. (2013). Linear aggregation of proteins on the membrane as a prelude to membrane remodeling. Proceedings of the National Academy of Sciences *110*, 20396-20401.

Simunovic, M., and Voth, G.A. (2015). Membrane tension controls the assembly of curvature-generating proteins. Nature Communications *6*.

Simunovic, M., Voth, G.A., Callan-Jones, A., and Bassereau, P. (2015). When Physics Takes Over: BAR Proteins and Membrane Curvature. Trends in Cell Biology *25*, 780-792.

Sinka, R., Gillingham, A.K., Kondylis, V., and Munro, S. (2008). Golgi coiled-coil proteins contain multiple binding sites for Rab family G proteins. J Cell Biol *183*, 607-615.

Snead, W.T., Zeno, W.F., Kago, G., Perkins, R.W., Richter, J.B., Zhao, C., Lafer, E.M., and Stachowiak, J.C. (2018). BAR scaffolds drive membrane fission by crowding disordered domains. BioRXiv.

Song, Y., DiMaio, F., Wang, R.Y., Kim, D., Miles, C., Brunette, T., Thompson, J., and Baker, D. (2013). High-resolution comparative modeling with RosettaCM. Structure *21*, 1735-1742.

Su, J., Thomas, A.S., Grabietz, T., Landgraf, C., Volkmer, R., Marrink, S.J., Williams, C., and Melo, M.N. (2018). The N-terminal amphipathic helix of Pex11p self-interacts to induce membrane remodelling during peroxisome fission. Biochimica et Biophysica Acta (BBA) - Biomembranes *1860*, 1292-1300.

Sugita, Y., Kitao, A., and Okamoto, Y. (2000). Multidimensional replica-exchange method for free-energy calculations. The Journal of Chemical Physics *113*, 6042-6051.

Sugita, Y., and Okamoto, Y. (1999). Replica-exchange molecular dynamics method for protein folding. Chemical Physics Letters *314*, 141-151.

Sun, R., Dama, J.F., Tan, J.S., Rose, J.P., and Voth, G.A. (2016). Transition-tempered Metadynamics is a promising tool for studying the permeation of drug-like molecules through membranes. Journal of Chemical Theory and Computation *12*, 5157-5169.

Szeto, T.H., Rowland, S.L., Habrukowich, C.L., and King, G.F. (2003). The MinD membrane targeting sequence is a transplantable lipid-binding helix. J Biol Chem *278*, 40050-40056.

Tang, J., Signarvic, R.S., DeGrado, W.F., and Gai, F. (2007). Role of helix nucleation in the kinetics of binding of mastoparan X to phospholipid bilayers. Biochemistry *46*, 13856-13863.

Thiam, A.R., Antonny, B., Wang, J., Delacotte, J., Wilfling, F., Walther, T.C., Beck, R., Rothman, J.E., and Pincet, F. (2013a). COPI buds 60-nm lipid droplets from reconstituted water-phospholipid-triacylglyceride interfaces, suggesting a tension clamp function. Proc Natl Acad Sci U S A *110*, 13244-13249.

Thiam, A.R., Farese, R.V., Jr., and Walther, T.C. (2013b). The biophysics and cell biology of lipid droplets. Nat Rev Mol Cell Biol *14*, 775-786.

Thorpe, I.F., Zhou, J., and Voth, G.A. (2008). Peptide folding using multiscale coarse-grained models. The Journal of Physical Chemistry B *112*, 13079-13090.

Torrie, G.M., and Valleau, J.P. (1977). Nonphysical sampling distributions in Monte Carlo free-energy estimation: Umbrella sampling. Journal of Computational Physics *23*, 187-199.

Tozzini, V., Rocchia, W., and McCammon, J.A. (2006). Mapping all-atom models onto one-bead coarse-grained models: General properties and applications to a minimal polypeptide model. Journal of Chemical Theory and Computation *2*, 667-673.

Tribello, G.A., Bonomi, M., Branduardi, D., Camilloni, C., and Bussi, G. (2014). PLUMED 2: New feathers for an old bird. Computer Physics Communications *185*, 604-613.

Tsirigos, K.D., Peters, C., Shu, N., Kall, L., and Elofsson, A. (2015). The TOPCONS web server for consensus prediction of membrane protein topology and signal peptides. Nucleic Acids Res *43*, W401-407.

Tuckerman, M., Berne, B.J., and Martyna, G.J. (1992). Reversible multiple time scale molecular dynamics. The Journal of Chemical Physics *97*, 1990-2001.

Ulmschneider, M.B., Doux, J.P.F., Killian, J.A., Smith, J.C., and Ulmschneider, J.P. (2010). Mechanism and Kinetics of Peptide Partitioning into Membranes from All-Atom Simulations of Thermostable Peptides. Journal of the American Chemical Society *132*, 3452-3460.

Vamparys, L., Gautier, R., Vanni, S., Bennett, W.F.D., Tieleman, D.P., Antonny, B., Etchebest, C., and Fuchs, Patrick F.J. (2013). Conical Lipids in Flat Bilayers Induce Packing Defects Similar to that Induced by Positive Curvature. Biophysical Journal *104*, 585-593.

Vanni, S., Vamparys, L., Gautier, R., Drin, G., Etchebest, C., Fuchs, P.F., and Antonny, B. (2013). Amphipathic lipid packing sensor motifs: probing bilayer defects with hydrophobic residues. Biophys J *104*, 575-584.

Voet, D., Voet, J.G., and Pratt, C.W. (2013). Fundamentals of Biochemistry: Life at the Molecular Level, Fourth Edition edn (Hoboken, NJ: Wiley).

Voth, G.A. (2013). New and notable: key new insights into membrane targeting by proteins. Biophys J *104*, 517-519.

Vymetal, J., and Vondrasek, J. (2011). Gyration- and inertia-tensor-based collective coordinates for metadynamics. Application on the conformational behavior of polyalanine peptides and Trp-cage folding. J Phys Chem A *115*, 11455-11465.

Walther, T.C., and Farese, R.V., Jr. (2012). Lipid droplets and cellular lipid metabolism. Annu Rev Biochem *81*, 687-714.

Wang, H., Becuwe, M., Housden, B.E., Chitraju, C., Porras, A.J., Graham, M.M., Liu, X.N., Thiam, A.R., Savage, D.B., Agarwal, A.K., *et al.* (2016). Seipin is required for converting nascent to mature lipid droplets. Elife *5*.

Welte, M.A. (2015). Expanding roles for lipid droplets. Curr Biol *25*, R470-481.

White, S.H., and Wimley, W.C. (1998). Hydrophobic interactions of peptides with membrane interfaces. Biochimica et Biophysica Acta (BBA) - Reviews on Biomembranes *1376*, 339-352.

Wilfling, F., Haas, J.T., Walther, T.C., and Jr, R.V.F. (2014). Lipid droplet biogenesis. Current Opinion in Cell Biology *29*, 39-45.

Wilfling, F., Wang, H., Haas, J.T., Krahmer, N., Gould, T.J., Uchida, A., Cheng, J.X., Graham, M., Christiano, R., Frohlich, F., *et al.* (2013). Triacylglycerol synthesis enzymes mediate lipid droplet growth by relocalizing from the ER to lipid droplets. Dev Cell *24*, 384-399.

Wu, E.L., Cheng, X., Jo, S., Rui, H., Song, K.C., Davila-Contreras, E.M., Qi, Y., Lee, J., Monje-Galvan, V., Venable, R.M., *et al.* (2014). CHARMM-GUI Membrane Builder toward realistic biological membrane simulations. J Comput Chem *35*, 1997-2004.

Yefimov, S., van der Giessen, E., Onck, P.R., and Marrink, S.J. (2008). Mechanosensitive membrane channels in action. Biophysical Journal *94*, 2994-3002.

Zehmer, J.K., Bartz, R., Liu, P., and Anderson, R.G. (2008). Identification of a novel N-terminal hydrophobic sequence that targets proteins to lipid droplets. J Cell Sci *121*, 1852-1860.

Zheng, W., Brooks, B.R., and Hummer, G. (2007). Protein conformational transitions explored by mixed elastic network models. Proteins: Structure, Function, and Bioinformatics *69*, 43-57.

Ziemba, B.P., Li, J., Landgraf, K.E., Knight, J.D., Voth, G.A., and Falke, J.J. (2014). Single-Molecule Studies Reveal a Hidden Key Step in the Activation Mechanism of Membrane-Bound Protein Kinase C-α. Biochemistry *53*, 1697-1713.